Measurement of equilibrium supercurrent noise in superconductor-normal ring and current-phase relation of helical hinge states of tungsten ditelluride

Xavier Ballu

université
PARIS-SACLAY

Measurement of equilibrium supercurrent noise in superconductor-normal ring and current-phase relation of helical hinge states of tungsten ditelluride

Mesure du bruit du supercourant à l'équilibre dans un anneau supraconducteur-normal et relation courant-phase des états de bord hélicaux du ditellure de tungstène

Thèse de doctorat de l'université Paris-Saclay

École doctorale n° 564, physique en Ile de France (PIF)
Spécialité de doctorat: Physique
Graduate School : Physique. Référent : Faculté des Sciences d'Orsay

Thèse préparée dans l'unité de recherche **Laboratoire de Physique des Solides** (Université Paris-Saclay, CNRS), sous la direction de **Meydi FERRIER**, Maître de conférences, la co-direction de **Hélène BOUCHIAT**, Directrice de recherche

Thèse soutenue à Paris-Saclay, le 19 décembre 2023, par

Xavier BALLU

Composition du jury

Membres du jury avec voix délibérative

Anne ANTHORE Professeure des universités, Université Paris-Cité	Présidente
Thilo BAUCH Professeur associé (HDR), Chalmers University of Technology	Rapporteur & Examinateur
Olivier BUISSON Directeur de recherche, Institut Néel, CNRS	Rapporteur & Examinateur
Francesco GIAZOTTO Directeur de recherche, Istituto Nanoscienze CNR, Scuola Normale Superiore di Pisa	Examinateur

THESE DE DOCTORAT

NNT : 2023UPASP189

université PARIS-SACLAY

ÉCOLE DOCTORALE
Physique en Île-de-France (PIF)

Titre: Mesure du bruit du supercourant à l'équilibre dans un anneau supraconducteur-normal et relation courant-phase des états de bord hélicaux du ditellure de tungstène

Mots clés: Transport quantique, isolant topologique, fluctuations de courant

Résumé: Une jonction SNS formée par un matériau non-supraconducteur (N) entre deux contacts supraconducteurs (S) peut être traversée par un supercourant porté par des états liés d'Andreev (ABS) qui est déterminé par la différence de phase supraconductrice aux bornes des contacts supraconducteurs. La valeur de ce courant et sa dynamique sont des sondes très sensibles des propriétés de transport cohérent et topologique dans le matériau non-supraconducteur. Une première expérience dans laquelle un fil mésoscopique (Au) est inséré dans un anneau supraconducteur a permis d'explorer la dynamique des ABS. A température finie, les fluctuations thermiques des ABS doivent donner lieu à des fluctuations du supercourant et donc à une dissipation à fréquence finie dont l'amplitude dépend de leur temps de relaxation comme prédit par le théorème fluctuation-dissipation. En couplant cet anneau à un résonateur supraconducteur nous avons réussi à mesurer indépendamment les fluctuations du supercourant à l'équilibre et la dissipation qui apparait quand on soumet l'anneau à un flux magnétique oscillant. Cette expérience constitue la première confirmation de ce théorème dans une jonction SNS. Dans une seconde partie, nous avons mis en évidence le caractère topologique du ditellure de tungstène (WTe2) à travers la mesure de la relation supercourant/phase en utilisant un dispositif d'interférence quantique supraconducteur (SQUID) asymétrique, constitué de deux jonctions SNS en parallèle. La forme en dent de scie de la relation courant-phase pour une facette latérale du cristal et la survie du supercourant à fort champ magnétique révèlent le caractère balistique et unidimensionnel du transport le long de certaines arêtes sur plus de 500 nm. Ceci est une signature de la présence d'états unidimensionnels protégés du désordre dans ce matériaux confirmant les prédictions d'une phase proche d'un isolant topologique d'ordre supérieur pour ce matériau.

Title: Measurement of equilibrium supercurrent noise in superconductor-normal ring and current-phase relation of helical hinge states of tungsten ditelluride
Keywords: Quantum transport, topological insulator, current fluctuations

Abstract: An SNS junction formed by a non-superconducting material (N) between two superconducting contacts (S) can sustain a supercurrent carried by Andreev bound states (ABS) which is determined by the superconducting phase difference across the superconducting contacts. The value of this current and its dynamics are very sensitive probes of the coherent and topological transport properties in the non-superconducting material. An initial experiment in which a mesoscopic wire (Au) is inserted into a superconducting ring has made it possible to explore the dynamics of the ABS. At finite temperature, thermal fluctuations in ABS should give rise to fluctuations in the supercurrent and therefore to a finite-frequency dissipation, the amplitude of which depends on their relaxation time, as predicted by the fluctuation-dissipation theorem. By coupling this ring to a superconducting resonator, we were able to measure independently the fluctuations in the supercurrent at equilibrium and the dissipation that occurs when the ring is subjected to an oscillating magnetic flux. This experiment constitutes the first confirmation of this theorem in an SNS junction. In the second part, we demonstrated the topological character of tungsten ditelluride (WTe2) by measuring the supercurrent/phase relation using an asymmetric superconducting quantum interference device (SQUID), consisting of two SNS junctions in parallel. The sawtooth shape of the current-phase relation for a lateral facet of the crystal and the robustness of the supercurrent at high magnetic field reveals the ballistic and one-dimensional character of the transport along certain edges over more than 500 nm. This is a signature of the presence of one-dimensional states protected from disorder in this material, confirming the predictions of a phase close to a higher-order topological insulator for this material.

Contents

Remerciements **7**

Synthèse en français **9**

Introduction, summary, and organization of the manuscript **15**

1 Quantum transport and linear response theory **21**
1.1 Electronic transport at the mesoscopic scale 21
1.1.1 A matter of length scale 21
1.1.2 Conductance of a mesoscopic system 21
1.2 Theoretical approach of quantum transport 22
1.2.1 Landauer formalism : the scattering approach 22
1.2.2 Linear response theory and quantum transport 22
1.2.3 The fluctuation-dissipation theorem 26
1.3 Superconducting proximity effect 29
1.3.1 DC and AC Josephson effect 29
1.3.2 Bogoliubov-de Gennes equations and Andreev reflection : the NS interface . . . 30
1.3.3 Andreev bound states : the SNS junction 31
1.3.4 Current-phase relations 35
1.4 Noise and conductance of a superconducting junction : a two-level toy model 37
1.4.1 Supercurrent noise in a superconducting and perfectly transmitting quantum point contact 37
1.4.2 Conductance of the quantum point contact 38
1.4.3 Susceptibility of a long diffusive SNS junction 40

2 Supercurrent noise in a phase-biased superconductor-normal ring in thermal equilibrium **43**
2.1 Conductance of a phase-biased Josephson junction in a ring geometry. 43
2.1.1 Defining the conductance of a superconducting junction 43
2.1.2 Ring's response and junction's response : screening effect 44
2.1.3 Susceptibility measurement : coupling a Josephson junction to a resonator . . . 45
2.1.4 Noise measurement in the same configuration 46
2.2 Experimental setup 46
2.2.1 The CryoHEMT amplifier 47
2.2.2 Sample fabrication 48
2.2.3 Modeling the transmission and noise measurements 50
2.3 Calibration procedure 57
2.3.1 Electronic temperature 57
2.3.2 Calibration of circuit elements 58

2.3.3 Calibration of transmission measurement . . . 59
2.4 Fluctuation and dissipation measurement : the SNS ring . . . 62
2.4.1 Inductance and conductance of the NS ring . . . 62
2.4.2 Noise and validation of the FDT . . . 71
2.5 Understanding phase and temperature dependence of the conductance . . . 75
2.5.1 Tight-binding model for the long diffusive SNS ring . . . 75
2.5.2 Phase dependence of G_D and G_{ND} . . . 76
2.6 General conclusion . . . 80

3 Ballistic hinge states in multilayer tungsten ditelluride 81
3.1 Introduction to topological insulators . . . 81
3.1.1 Topological band structure . . . 81
3.1.2 Topological protection and spin-momentum locking . . . 83
3.1.3 Superconducting proximity effect and topological insulators . . . 83
3.2 Topological phases of Tungsten Ditelluride . . . 85
3.3 Current-Phase Relations measurements . . . 87
3.3.1 Superconducting Quantum Interference Device . . . 87
3.3.2 Diffraction phenomena in a single Josephson junction . . . 89
3.4 Device fabrication . . . 94
3.4.1 Exfoliation and transfer . . . 94
3.4.2 Sample design . . . 96
3.4.3 Lithography and metal deposition . . . 97
3.5 Measurement techniques. . . . 97
3.5.1 Differential resistance . . . 97
3.5.2 Counter technique . . . 99
3.5.3 Advantages and drawbacks of the two techniques. . . . 99
3.6 Current-phase relation of topological hinge states in multilayer tungsten ditelluride . . . 100
3.6.1 Characterization of the reference junction. . . . 100
3.6.2 Current-phase relation of the edge junction . . . 104
3.6.3 High field behaviour. . . . 111
3.7 Conclusion and perspectives. . . . 114

Conclusion 117

Bibliography 119

Remerciements

Si je peux aujourd'hui rédiger ces derniers mots dans ce manuscrit, c'est avant tout en grande partie grâce à ces

Tout d'abord, ce manuscrit a été relu et révisé par Anne Anthore, présidente du jury, Francesco Giazotto, examinateur, et avec une attention toute particulière par Olivier Buisson et Thilo Bauch qui en ont été les rapporteurs. Merci à eux d'avoir accepté cette tâche, pour les commentaires et les discussions qui ont suivies.

Bien sûr, ce manuscrit a été réalisé à la fin d'un travail réalisé dans une équipe incroyable que je tiens à remercier encore et encore. Merci à Sophie et Richard pour leur bienveillance et les réponses à toutes les questions que je pouvais leur poser, Alexei pour ses suggestions sur l'histoire à raconter à l'approche du grand jour, et Miguel pour son oreille toujours attentive. À mes camarades thésards et postdocs dans le groupe : Yan pour être toujours positive, les bébés Jules, Lucas (que j'ai peut-être fait un peu souffrir à son arrivée, oups !) et Matthieu à qui j'ai confié la lourde de tâche de représentant des non-permanents. Merci à Arthur le dernier arrivé qui à dû supporter mes états d'âmes de fin de thèse. Enfin, les compagnons qui étaient déjà là quand je suis arrivé : Alexandre et Victor, mais aussi Jorge pour les rigolades dans le bureau, un soutien moral inconditionnel, et les grands débats sur le genre des mots en français et en espagnol. Un grand merci également à Raphaëlle qui pose toujours les questions que je ne veux pas entendre et m'a ainsi appris à faire de la biblio correctement, mais sait récompenser d'une photo de petit chat.

Ce travail a été supervisé également par Ziwei et Hélène que je tiens à remercier pour tout ce qu'ils m'ont appris autant scientifiquement que personnellement. Enfin, un grand merci à Meydi, que je suis depuis mon entrée en magistère et qui a été jusqu'à m'emmener avec lui au Québec pour me remettre les idées en place quand je divaguais un peu trop. Merci pour cette grande aventure qui se termine aujourd'hui, et bravo pour avoir réussi à me supporter !

De ce séjour aux LPS je ne retiendrai pas que de la physique passionnante, mais également des souvenirs partagés avec de nombreuses personnes. J'adresse donc ces quelques mots à ces personnes qui ont rendu l'aventure si spéciale : À Marco et Charis pour des bières et des discussions toujours passionnantes. À Alexandra, Stanislas, Joao, André, Banan les magnétiseurs du babyfoot et les repas partagés ensemble. À Raphael, l'auto-proclamé abbé Pierre de lÀ litho élec' (mais qui n'a pas le même talent pour le baby...). À Antoine "Boubou", qui lui a un talent pour le babyfoot qu'il n'a pas pour la litho élec, mais qui a accepté de m'accompagner en salle blanche et m'a donné un sacré coup de main pour toute la fabrication. À Léo et tous moments passés ensemble au sein du labo comme à l'extérieur (et pour m'avoir hébergé quand je me suis fait voler mon velux !). À Sujit pour les innombrables *mental breakdance* traversés ensemble. À Helen pour sa bonne humeur communicative et les coups qu'on a encore à boire ensemble. À Ansgar l'allemand le plus corse que je connaisse. À Vincent et Antoine (encore un) pour les sessions grimpes toujours délicieuses. À Mateo et les grands moments passés sur la neige ou au bord de mer. Et à tous ceux

avec qui j'ai partagé un bout de ce chemin : Baptiste, Mark, Pascal, Florian, Sara, Freek, Anniina.

Merci à la team Sherbrooke : Bertrand Reulet pour m'avoir accueilli dans son groupe. Edouard, Laurine et Madeleine des cobureaux grimpeurs, randonneurs, qui ne disent jamais non pour une petite poutine au souper. Bien sûr merci au reste du groupe : Maxime, Louis, Alexandre, Clovis, Nico, Gabriel, Christian. Merci à tous les copains rencontrés là-bas, et en particulier à mes partenaires de rédaction, Lucas et Claude.

Enfin, merci à mes parents, Anaïs et Didier, et mes soeurs Emmanuelle et Christelle pour m'avoir toujours soutenu pendant ces huit années d'études, parfois compliquées, même si vous ne compreniez pas toujours où je voulais aller.

Aux copains qui se sont retrouvés à un moment ou l'autre mêlés à des choix pas toujours réfléchis : merci à Emilie, Lolo et toute la team prépa. Merci à l'équipe des physiciens, en particulier ceux avec qui j'ai passé de nombreuses soirées et week-end : Marion, Victor, La Huche, La Franche, Charlotte.

À mes amis les plus proches. Jade et Hayat le duo légendaire. Alexis Bébouski là depuis le tout tout début. Manon, la Lady Mélody. Seb le grand aventurier. Timo mon *bradaframanadamada* et Zonzon que je viendrai embêter jusqu'en Italie. Lulu avec qui j'ai fêté chaque étape de mes études, bientôt pour une dernière fois.

Mes derniers remerciements vont à Greis. Merci pour ton soutien indéfectible et toute la joie que tu as apporté avec toi.

Synthèse en français

Cette thèse porte sur les propriétés fondamentales du supercourant qui passe à travers un matériau non-supraconducteurs, autrement dit les propriétés des jonctions SNS (S pour supraconducteur et N pour normal). Les notions utiles à la compréhension générale de ce travail de thèse dans son ensemble sont introduites dans le premier chapitre de ce manuscrit, intitulé **Transport quantique et réponse linéaire**. En particulier sont introduites dans ce chapitre les bases théoriques de la supraconductivité par effet de proximité et les différentes charactéristiques du supercourant dans une jonction supraconductrice hybride, ainsi que les bases du formalisme de la réponse linéaire. Ce chapitre se termine par le modèle des fluctuations du supercourant d'un système à deux niveaux (le point de contact quantique) et de sa conductance, permettant d'introduire une des premières motivations de ce travail de thèse : la mesure du *bruit* du supercourant dans une jonction SNS dans le régime long diffusif.

Mesure du bruit du supercourant dans un anneau supraconducteur-normal

Le deuxième chapitre de ce manuscrit (et premier chapitre expérimental) de ce manuscrit est consacrée à la mesure à la fois des fluctuations de supercourant à l'équilibre thermique et à la *conductance* d'une jonction longue diffusive. A cause de la grande non-linéarité de ces objets, une attention particulière est portée sur la définition d'un régime linéaire d'une jonction SNS nous permettant à la fois de définir une conductance et de rester dans le domaine de validité du théorème fluctuation-dissipation et de mesurer indépendemment les deux quantités qui nous intéressent. Tout d'abord, la jonction est placée dans un anneau supraconducteur. Via l'application d'un champ magnétique, un flux magnétique permet de contrôler la différence de phase supraconductrice entre les deux interfaces NS de la jonction. L'anneau est inductivement couplé à un résonateur supraconducteur, ce qui permet à la fois de convertir le bruit en courant de l'anneau en bruit en tension pour les mesures de bruit et de polariser l'anneau avec une phase alternative pour les mesures de conductance. Le montage expérimental est complété par l'utilisation d'un amplificateur cryogénique fabriqué par Y. Jin et Q. Dong (Centre de Nanosciences et de Nanotechnologies) connecté directement au résonateur.

Une importante partie de ce travail est la calibration de la mesure. A phase nulle, où flux nul, la température électronique ainsi que la valeur des éléments du circuit sont déterminés via la mesure du spectre de bruit en tension ainsi que du coefficient de transmission. La mesure du coefficient de transmission en fonction de la différence de phase supraconductrice - ou plutôt sa différence par rapport au cas où la différence phase est nulle - nous donne accès séparément aux composantes réactive (inductance) et dissipative (conductance) de la réponse de la jonction à une excitation. La relation courant-phase de la jonction est extraite via l'inductance

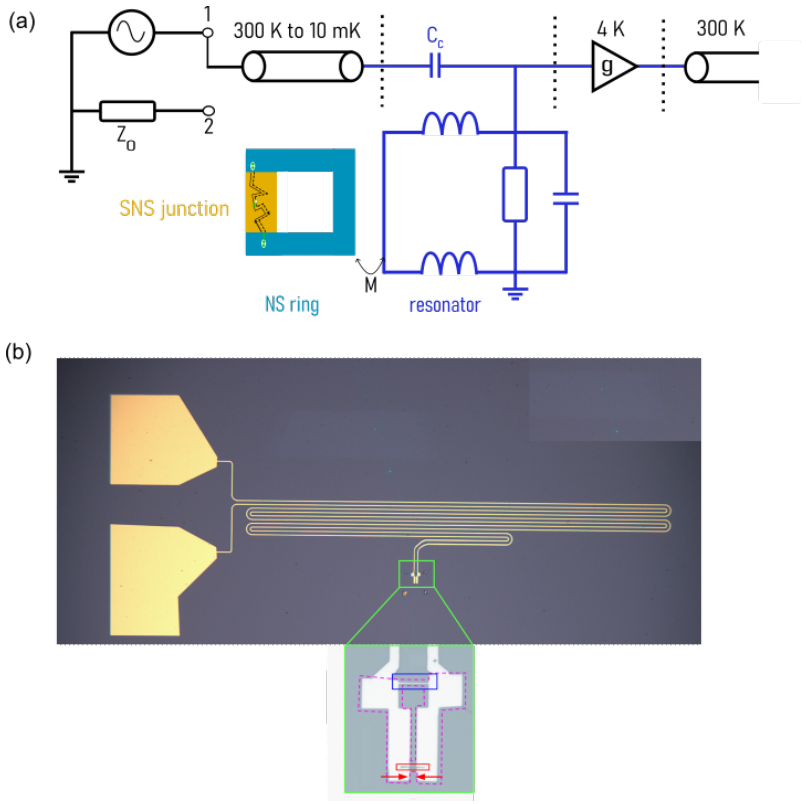

FIGURE 1 – Dispositif expérimental et de l'échantillon étudié dans le chapitre 2 de ce manuscrit. (a) Schéma de principe de la mesure. La jonction SNS est placée dans un anneau supraconducteur, formant un anneau NS, inductivement couplé à un résonateur supraconducteur directement connecté à l'amplificateur cryogénique. Grâce à ce dispositif expérimental, en utilisant le même échantillon, il est possible de mesurer la réponse de l'anneau à une excitation en phase (représenté par une excitation sur le résonateur, position "1"), et sans excitation (représenté par la position "2". (b) Image au microscope optique du résonateur supraconducteur, les méandres en molybdène-rhénium représentant la partie inductive du résonateur (la partie capacitive est soudée sur le porte-échantillon et n'est pas représentée ici). Le cadre vert est un zoom sur l'anneau, encadré par les pointillés rose. Le cadre bleu montre l'inductance de couplage, tandis que la jonction (dont la partie normale est un fil d'or) est encadré en rouge.

mesurée, et sa forme et l'évolution en température confirment le régime long diffusif. La conductance est également obtenue et est à comparer au bruit en courant mesuré sur le même échantillon, et est présenté en Fig. 2.

Premièrement, la bonne thermalisation entre le résonateur et l'anneau est confirmée via l'utilisation de la même valeur de température électronique. De plus, l'accord entre les lignes de base (indépendante en phase), est une vérification du théorème pour le résonateur seul tandis que la partie dépendante en phase est la vérification de ce même théorème pour l'anneau NS.

Enfin, il nous est possible de dissocier la réponse de la jonction de la réponse

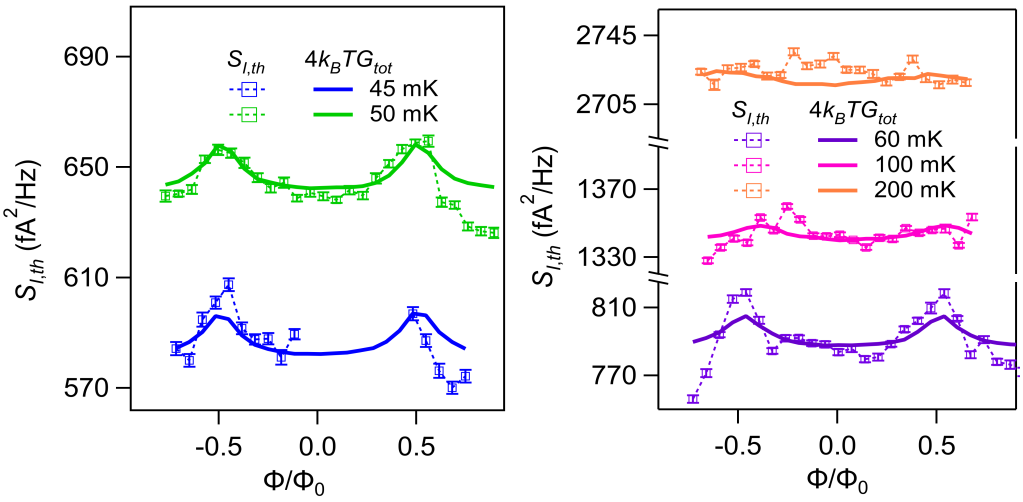

FIGURE 2 – Théorème fluctuation-dissipation dépendant de la différence de phase supraconductrice. Comparaison entre les fluctuations du courant (carrés) et la conductance (lignes pleines).

de l'anneau en prenant en compte les effets d'écrantage du champ magnétique. Il vient que la conductance de la jonction est quasiment indépendante de la différence de phase supraconductrice mais fortement dépendante de la température en $1/T$, contrastant avec la conductance d'un métal dans l'état normal. Dans une dernière partie de ce chapitre, des calculs numériques via un modèle de liaisons fortes et une première approche théorique nous permette d'expliquer ces phénomènes, due en particulier à la symétrie électron-trou imposée par la supraconductivité.

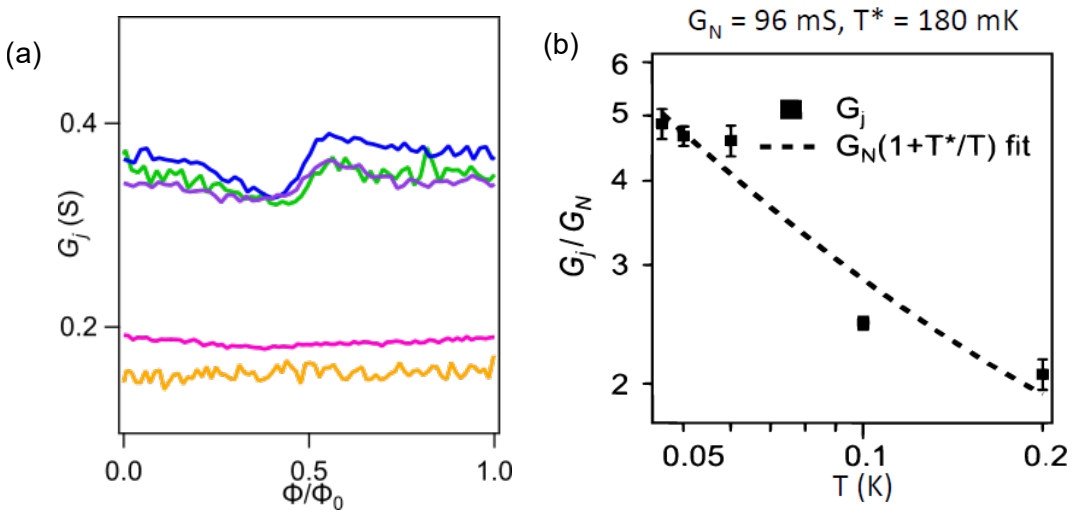

FIGURE 3 – (a) La conductance de la jonction est indépendente de la phase. (b) Cependent, elle dépend fortement de la température, et à basse température peut atteindre jusqu'à cinq fois la conductance du même matériau dans l'état normal.

Des états unidimensionnels et balistiques aux arêtes du ditellure de tungstène

Le troisième chapitre de ce manuscrit est consacrée à la révélation expérimentale d'états balistiques charnières d'un matériau topologique, matériaux introduits dans une première partie de ce chapitre. En particulier, nous nous concentrons sur le ditellure de tungstène (WTe_2). Ce dernier est un matériau riche de par ses nombreuses propriétés topologiques : ces dix dernières années, il a été théorisé et montré expérimentalement qu'en monocouche le WTe_2 est un isolant quantique de spin, c'est-à-dire que sa surface est isolante mais que ses bords présentent des états conducteurs. De plus, la direction de propagation des électrons au bord est associé au spin (verrouillage spin-impulsion), ce qui entraîne une protection topologique face à, par exemple, une rétrodiffusion sur une impureté non-magnétique. En multicouche, le WTe_2 est un matériau plus complexe : il a été montré qu'il s'agit d'un matériau de Weyl de type II, induisant des états de surface topologiques. De récentes études expérimentales ont cependant montré l'existence d'états unidimensionnels sur les arêtes du ditellure de tungstène, sans pour autant discriminer leur caractère topologique ou non. Une description plus approfondie du matériau est l'objet de la seconde partie de ce chapitre. L'objectif de cette expérience est de déterminer la nature de ces états de bords. Pour ce faire, nous souhaitons mesurer la relation courant-phase d'une jonction SNS où le matériau non-supraconducteur est le bord d'un multicouche de WTe_2. Expérimentalement cela passe par la fabrication d'un dispositif d'interférence quantique supraconducteur (SQUID) asymétrique, consistant dans notre cas en deux jonctions SNS en parallèle, une de référence et l'autre à sonder. Dans notre expérience, la jonction de référence est placée dans le volume du WTe_2. Enfin, le courant critique du SQUID en fonction du champ magnétique est la somme des courants critiques des deux jonctions, ce qui en première approximation fait que l'on mesure le courant critique de la jonction de référence modulée par la relation courant-phase de la jonction que l'on souhaite sonder. Les détails de cette technique, de la fabrication et les techniques de mesure sont l'objet respectivement des parties 3, 4 et 5 de ce manuscrit.

Finalement, la dernière partie de ce chapitre est une description et une analyse des résultats obtenus, résumé dans la figure 4. Grâce à la branche du SQUID qui sert de jonction de référence, nous avons pu déterminer le caractère diffusif (c'est-à-dire topologiquement triviaux) des états conducteurs du WTe_2 en volume et surface. La partie d'intérêt nous donne une relation courant-phase qui ressemble à une *dent de scie* (Fig. 4(d), forme caractéristique d'une jonction SNS dans le régime long et balistique. De plus, la valeur de ce supercourant nous permet de déterminer qu'il existe cinq canaux de conduction balistiques dans notre échantillon, coïncidant avec le nombre d'arêtes visibles en microscopie électronique (Fig. 4(c)). De plus, la survie d'un supercourant à fort champ (jusqu'à 2 T), donne des indices sur le caractère unidimensionnels de ces états. Ces expériences confirment donc la présence d'états balistiques unidimensionnels aux bords du WTe_2, indiquant un possible caractère topologique.

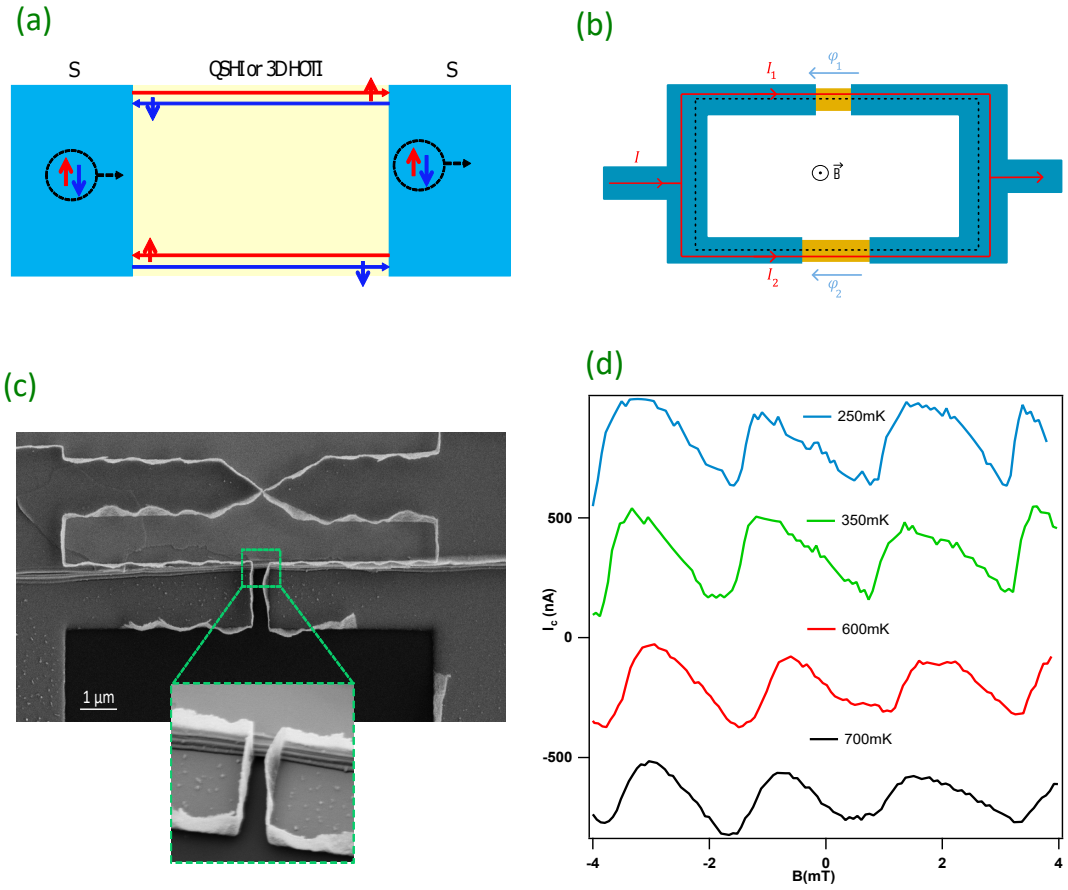

FIGURE 4 – (a) Un isolant topologique 2D ou un isolant topologique d'ordre deux en 2D présente des états de conductions hélicaux à ses bords. Ces états ont différentes propriétés topologiques, par exemple le verrouillage spin-impulsion qui associe le signe d'un spin à une direction de propagation, amenant à une protection contre la rétrodiffusion par une impureté non-magnétique. A l'aide de la supraconductivité par effet de proximité, il est possible de sonder la nature de ces états hélicaux, comme par exemple en mesurant la relation courant-phase d'une jonction SNS à base de ces matériaux topologiques. (b) Expérimentalement, cela est possible en utilisant un SQUID asymétrique, fait à partir de deux jonctions SNS en parallèle (bleu : supraconducteur, jaune : métal non-supraconducteur). (c) La jonction de référence de ce SQUID asymétrique est fabriquée dans le volume du WTe_2, et une jonction au bord de ce même échantillon est la jonction que nous souhaitons étudier (rectangle vert). En mesurant le courant critique du SQUID (qui est la somme des courants passant dans les deux jonctions), nous avons accès à la relation courant-phase de la jonction au bord. (d) La relation courant-phase mesurée est une dent de scie, évoluant très peu avec la température. Cette forme est représentative d'une jonction SNS dans le régime long et balistique, indiquant que le courant au bord du WTe_2 est transporté par des états balistiques sur une distance de plus de 500 nm. Cette mesure est une preuve supplémentaire du caractère topologique du WTe_2.

Introduction, summary, and organization of the manuscript

This thesis deals with the fundamental properties of the supercurrent through a non-superconducting link inserted in a superconducting ring. A magnetic flux controls the phase difference across the link and modulates the properties of the supercurrent.

A first question we adressed (both theoretically and experimentally) is how to characterize the dissipation in such a system. Experimentally the ring configuration is ideal in an oscillating magnetic field which modulates the phase difference, realizing a phase biasing of this non-connected ring. The non-dissipative current is in phase with the *ac* excitation ; the dissipative current is out-of-phase. By measuring both the noise and the *ac* magnetic susceptibility of such an SNS (superconductor-normal-superconducor) ring we not only verified the fluctuation-dissipation theorem for hybrid superconducting junction but we also have demonstrated a peculiar increase of the conductance (dissipation) at low temeprature specific to a normal metal proximitized by a superconductor. Tight-binding simulations suggest that this dissipation is mostly due to transitions between Andreev levels that are symmetric around the Fermi energy, a hallmark of the electron-hole symmetry induced by the superconductor. Consequently, in contrast with the Drude conductance of a normal metal, the conductance of the hybrid junction is temperature dependent (it decreases with temperature as 1/T) and experimentally can reach up to five times the Drude conductance of a non-superconducting metal. The main results are summarized in Fig. 5.

A second part of this thesis is devoted to reveal the presence of helical states at the hinges of a topological material, tungsten ditelluride. For this, we measure the flux-dependence of the critical current of an asymmetric *dc* SQUID in which we used a topological material, WTe_2, as the weak link. The goal is to reveal the helical states that are supposed to carry the supercurrent ballistically. The reference junction used for this SQUID is on the surface of the thick WTe_2 crystal whereas the smaller critical current jjunction is due to the helical states at the hinges of the crystal. By measuring the critical current of the SQUID, we access the current-phase relation of the hinge states and reveal the ballistic transport of those states over a distance (500 nm) which is ten time the elastic mean free path of the electrons. A summary is found in Fig. 6.

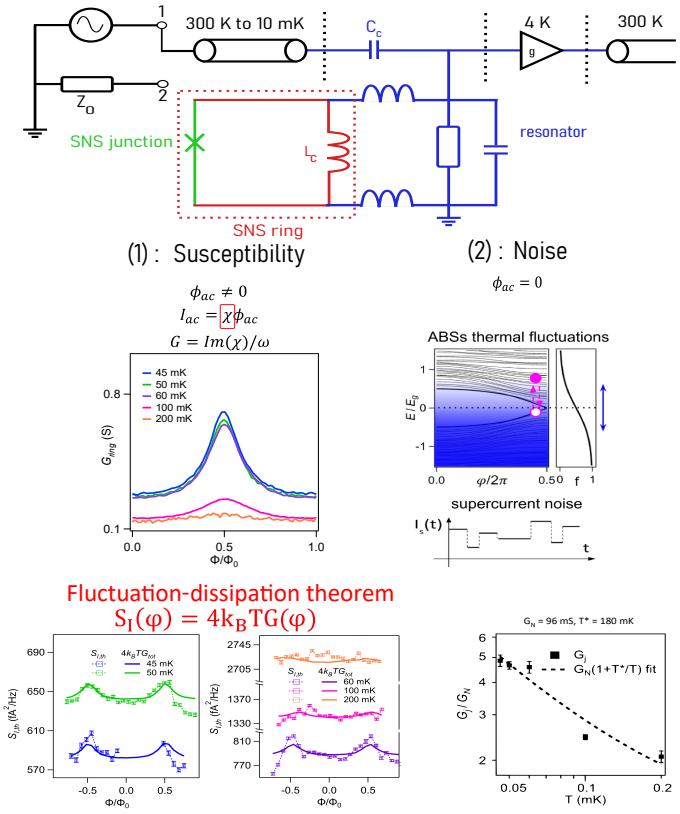

FIGURE 5 – **(a)** The SNS ring (green : junction, red : ring, blue : superconducting resonator) has a supercurrent modulated by the phase difference between the two superconducting boundaries. This phase difference is controlled using a magnetic flux ϕ_{dc}. On top of this *dc* flux, an oscillating *ac* flux ϕ_{ac} is added by coupling an rf resonator to the ring. The ring's response in turn modifies the resonator's resonance frequency and quality factor. Those shifts are directly related to the magnetic susceptibility of the ring. **(b)** the imaginary part of the magnetic susceptibility. This quantity is related to the conductance of the SNS ring and is phase dependent. The plot shows the phase dependent conductance of the ring. **(c)** The noise of the ring is measured with no *ac* excitation. The noise is due to thermally activated transitions between Andreev levels that carry current with an alternating sign : the current thus fluctuates around a mean value. The schematics here shows a fluctuating supercurrent with time. The quantity of interest is not the current itself but the current noise, which is defined here as the Fourier transform of the correlator current-current. **(d)** The measurement of the conductance and the supercurrent noise of the same sample allows us to compare the two quantities using the fluctuation-dissipation theorem. **(e)** The temperature dependence of the conductance of the SNS junction, that we explain by the electron-hole symmetry imposed by the superconducting boundaries.

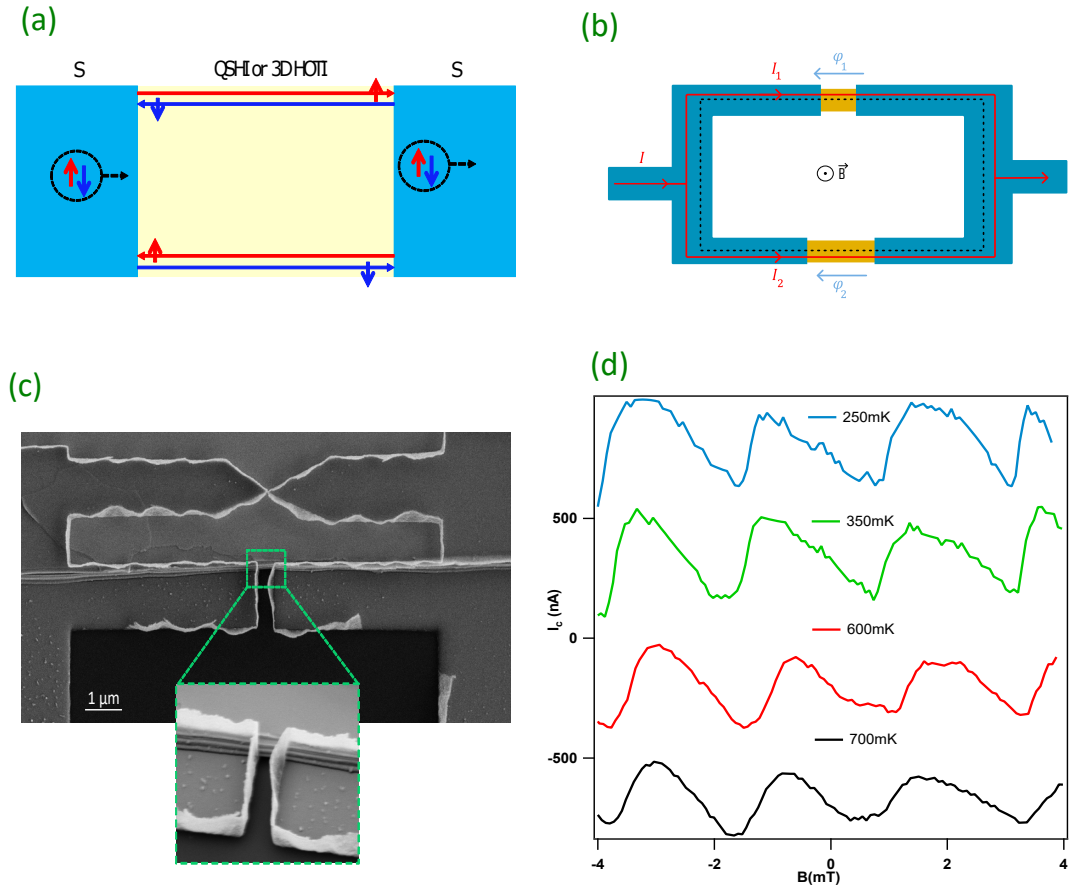

FIGURE 6 – **(a)** A 2D topological insulator or 3D second-order topological insulator has helical conducting states at its edges. These state present different topological properties, such as the spin-momentum locking or the protection from backscattering. Using the superconducting proximity effect, the idea is to probe the nature of these channels, by measuring their current-phase relation. **(b)** To do so, the tool we use is the *dc* asymmetric SQUID, consisting of two SNS junctions in parallel (blue : superconductor, yellow : normal metal). **(c)** The reference junction of this SQUID is fabricated using the bulk of WTe_2 and by measuring the critical current (which is the sum of the current going through the two junctions), we get acces to the current-phase relation of the hinge junction highlighted in the green rectangle. **(d)** The current-phase relation measured is a sawtooth. This shape is a tell-tale sign that the current through the hinge flows ballistically over 500 nm. This is due to the topological character of WTe_2

.

Organization of the thesis

The organisation of this manuscript is the following :

— In the introductive chapter, we introduce all the general notions needed to understand the idea of this work. We start by a short introduction on the mesoscopic scale. We introduce also the scattering formalism and Kubo formalism to define the conductance in mesoscopic physics. A part is dedicated to the superconductivity proximity effect and we finally give a short derivation to the fluctuation-dissipation theorem in a superconducting quantum point contact to introduce the second chapter.

— In the chapter **Supercurrent noise in a phase-biased superconductor-normal ring in thermal equilibrium**, we detail the measurements of thermal noise and conductance. Section 2.1 details the principle of the experiments and give a theoretical insight on the quantities we want to measure. The experimental part starts with section 2.2 in which we detail the setup before the calibration and technical part of section 2.3. The experimental results are detailed in section 2.4, and a discussion on the results and the comparison with numerical simulations can be found in section 2.5.

— In the chapter **Ballistic hinge states in multilayer tungsten ditelluride**, we start by an introduction on the (higher order) topological insulators in section 3.1, with a focus on the specific S/topological insulator/S junction. In section 3.2, we present briefly WTe_2. The principle of the experiment is detailed in section 3.3. Sections 3.4 and 3.5 deal with the fabrication of the samples and the measurement techniques used during this PhD. Finally, the results are detailed and discussed in section 3.6.

1 - Quantum transport and linear response theory

1.1 . Electronic transport at the mesoscopic scale

1.1.1 . A matter of length scale

In the field of quantum transport, the phenomena we are interested in take place in system with a large number of atoms, electrons or other quantum objects but in a reasonable size so that these phenomena have to be describe by quantum mechanics : mesoscopic physics is then first a matter of length scale.
The first length scale we describe is maybe the most important one to consider: the phase coherence length L_φ. It is the distance range in which the phase of an electron, is well defined. This means that electronic interferences are possible within this range, and these interferences give rise to quantum effects. However phase coherence is limited by a lot of processes, for instance inelastic collisions such as electron-phonon ones or electron-electron interactions.
Thus, to consider a system to be coherent and for the rest of this section, we consider a system of characteristic size $L < L_\varphi$. Transport properties are controlled by electrons near the Fermi level. Considering this, we need to take into account the length scale associated with the electronic wavefunction : the Fermi wavelength λ_F. Last but not least, the elastic mean free path l_e of an electron is an important quantity to consider when studying transport as it determines the nature of transport of the considered system.

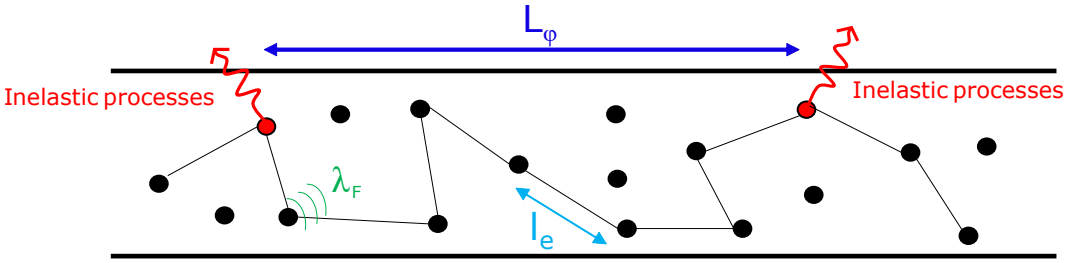

FIGURE 1.1 – Summary of the typical length scales of a mesoscopic system : L_φ is the phase coherence length, l_e the elastic mean free path (the mean distance between elastic collisions) and λ_F the Fermi wavelength.

— If the electron can travel from one end of the conductor to the other without scattering, i.e. if $l_e > L$, the system is said to be **ballistic**.
— Otherwise, the electron scatters and we are entering a diffusive regime : the system is then **diffusive**.

1.1.2 . Conductance of a mesoscopic system

Electronic transport is generally described by the conductivity σ, which is classicaly an intrinsic characteristic of a system, independent of the geometry of the

conductor or the environment. However experimentally the measured quantity is the conductance G, and more precisely the current I in response of an applied voltage via Ohm's law $I = GV$ and the conductivity is obtained via $G = \sigma S/L$. In this classical picture, the conductance is seen as coming from the scattering of the charge carriers. Two approaches, at first glance radically different, give a more precise definition of conductance. The first one we describe is the Landauer approach [1] that we describe briefly in section 1.2.1 and Kubo and Greenwood approach, subject of section 1.2.2.

1.2 . Theoretical approach of quantum transport

1.2.1 . Landauer formalism : the scattering approach

Landauer's approach consists on seeing the conductor we want to probe the conductance of as a barrier, and the wires used to send the current to the conductor as waveguides. The conductor is describe by its transmission coefficient τ.

The four wire conductance of one channel is given by :

$$G = \frac{2e^2}{h}\tau \tag{1.1}$$

where the factor 2 is for the spin degeneracy. Even for a ballistic wire, for which $\tau = 1$, there is still a finite resistance given by :

$$R_Q = \frac{h}{2e^2} = 12.9\ \mathrm{k}\Omega \tag{1.2}$$

which is the quantum of resistance. This finite resistance comes from the contacts which then play a major role in quantum transport experiments. To access the intrinsic properties of the materials we want to study, we develop a technique which does not require any contacts. To describe these systems, Kubo formalism is more suited as it describes the local conductance, and it is presented in the following.

1.2.2 . Linear response theory and quantum transport

This section aims at giving the readers the basic tools of linear response theory and a derivation of the fluctuation-dissipation theorem to understand the first part of the manuscript. It is heavily inspired by C. Texier lectures notes [2] and T. T. Heikkilä's book [3], and G. Montambeaux and E. Akkermans' book [4]

(a) Kubo formula : general formulation

The Kubo approach of quantum transport can be summed up as follows : we consider a conductor first at equilibrium. This conductor will be perturbed by an external potential, yielding the creation of an electric field $\vec{E}$ which yields in the linear response a current density $\vec{j} = \sigma\vec{E}$. To compute σ, we need to introduce in the Hamiltonian of the system a term related to the electric field. The correct way

to do it is by introducing the vector potential $A(t)$ such that :

$$\vec{E} = -\frac{\partial A}{\partial t} \quad \text{and} \quad \vec{\nabla} \times \vec{A} = 0 \tag{1.3}$$

and the Hamiltonian is written :

$$\mathcal{H} = \frac{[\vec{p} + e\vec{A}(t)]^2}{2m} + V(\vec{r}) \tag{1.4}$$

And considering that the current density $\vec{j}$ is given by :

$$\vec{j} = \mathrm{Tr}(\rho\widehat{j}) \tag{1.5}$$

where $\widehat{j}$ is the current density operator and $\rho(t)$ the density matrix, solution of the following equation :

$$i\hbar\frac{\partial \rho}{\partial t} = [\mathcal{H}, \rho] \tag{1.6}$$

ρ is generally written as $\rho = \rho_0 + \delta\rho$ with ρ_0 the density matrix at equilibrium, i.e. in the case $\vec{A} = \vec{0}$. To take into account the perturbation starting at $t = -\infty$ we can add a relaxation term to equation 1.6. This relaxation term is of the form $-i\gamma\delta\rho(t)$ in equation 1.6 and taking the limit $\gamma \to 0$. $\hbar/\gamma$ can be interpreted as the lifetime of the electrons in the conductor before it escapes in the reservoirs, mimicking the relaxation due to inelastic collisions. Introducing this term in equation 1.6 yields :

$$i\hbar\frac{\partial \rho}{\partial t} = [\mathcal{H}, \rho] - i\gamma(\rho(t) - \rho_{eq}(t)) \tag{1.7}$$

where ρ_{eq} describes the total system at thermodynamic equilibrium.

The linear response approximation consists on keeping in the expression of $\delta\rho(t)$ and $\delta\rho_{eq}(t)$ only the linear terms in $\vec{A(t)}$. Therefore, we rewrite the Hamiltonian of equation 1.4 :

$$\begin{aligned} \mathcal{H} &= \mathcal{H}_0 + \mathcal{H}_1(t) \\ \mathcal{H}_0 &= \frac{\vec{p}^2}{2m} + V(\vec{r}) \\ \mathcal{H}_1(t) &= \frac{e}{2m}(\vec{p}\cdot\vec{A} + \vec{A}\cdot\vec{p}) \end{aligned} \tag{1.8}$$

and equation 1.7 can be written :

$$i\hbar\frac{\partial \delta\rho}{\partial t} = [\mathcal{H}_0, \delta\rho(t)] + [\mathcal{H}_1, \delta\rho_0] - i\gamma(\delta\rho(t) - \delta\rho_{eq}(t)) \tag{1.9}$$

We write in a basis $(|n\rangle, \varepsilon_n)$ of eigenstates of $\mathcal{H}_0$ the Fourier transform of equation 1.9 :

$$\langle n|\delta\rho(\omega)|l\rangle = \frac{[f(\varepsilon_n) - f(\varepsilon_l)]\langle n|\mathcal{H}_1|l\rangle - i\gamma\langle n|\delta\rho_{eq}(\omega)|l\rangle}{(\varepsilon_n - \varepsilon_l) - \hbar\omega - i\gamma} \tag{1.10}$$

with $f(\varepsilon_n)$ the occupation of the state $|n\rangle$. If we assume $\delta\rho_{eq}$ to be stationary, we have :

$$\langle n|\delta\rho_{eq}(\omega)|l\rangle = \frac{f(\varepsilon_n) - f(\varepsilon_l)}{\varepsilon_n - \varepsilon_l}\langle n|\mathcal{H}_1(\omega)|l\rangle \tag{1.11}$$

and we can also write the current density operator as $\widehat{j} = \widehat{j_0} + \widehat{j_1}$:

$$\begin{aligned} \widehat{j_0} &= -\frac{e}{2m}(\widehat{n}\vec{p} + \vec{p}\widehat{n}) \\ \widehat{j_1} &= -\frac{e^2}{2m}(\widehat{n}\vec{A} + \vec{A}\widehat{n}) \end{aligned} \tag{1.12}$$

such that the current density $\vec{j}$ given by equation 1.5 can be written :

$$\begin{aligned} \vec{j} &= \mathrm{Tr}(\rho_0\widehat{j_1}) + \mathrm{Tr}(\delta\rho(t)\widehat{j_0}) \\ &= -A(\omega)[\frac{n_e e^2}{m} + \frac{e^2}{m^2\Omega}\sum_{n,n\neq l}\frac{f(\varepsilon_n) - f(\varepsilon_l)}{\varepsilon_n - \varepsilon_l}\frac{\varepsilon_n - \varepsilon_l - i\gamma}{\varepsilon_n - \varepsilon_l - \hbar\omega - i\gamma}|\langle n|\vec{p}|l\rangle|^2] \end{aligned} \tag{1.13}$$

From which we can deduce the conductivity using $\vec{j} = \sigma\vec{E} = i\omega\sigma\vec{A}$. It takes the form :

$$\sigma = \frac{i}{\omega}[\frac{n_e e^2}{m} + \frac{e^2}{m^2\Omega}\sum_{n,n\neq l}\frac{f(\varepsilon_n) - f(\varepsilon_l)}{\varepsilon_n - \varepsilon_l}\frac{\varepsilon_n - \varepsilon_l - i\gamma}{\varepsilon_n - \varepsilon_l - \hbar\omega - i\gamma}|\langle n|\vec{p}|l\rangle|^2] \tag{1.14}$$

To simplify this expression, we use the following sum rule called "f-sum rule" :

$$n_e + \frac{1}{m\Omega}\sum_{n,n\neq l}\frac{f(\varepsilon_n) - f(\varepsilon_l)}{\varepsilon_n - \varepsilon_l}|\langle n|\vec{p}|l\rangle|^2 = 0 \tag{1.15}$$

and by taking the matrix element of the current operator defined as $j_{nl} = -e/m\langle n|p|l\rangle$, we arrive at :

$$\sigma = i\frac{\hbar}{\Omega}\sum_{n,n\neq l}\frac{f(\varepsilon_n) - f(\varepsilon_l)}{\varepsilon_n - \varepsilon_l}\frac{|j_{nl}|^2}{\varepsilon_n - \varepsilon_l - \hbar\omega - i\gamma} \tag{1.16}$$

whose real part, the dissipative component, is then :

$$\mathrm{Re}\sigma(\omega) = -\frac{\pi\hbar}{\Omega}\sum_{n,n\neq l}\frac{f(\varepsilon_n) - f(\varepsilon_l)}{\hbar\omega}|j_{nl}|^2\delta_\gamma(\varepsilon_n - \varepsilon_l - \hbar\omega) \tag{1.17}$$

This last equation is the general formulation of the Kubo formula for a disorder conductor in a wire geometry. The fonction δ_γ appearing is a δ function "enlarged" by the relaxation term γ, such that :

$$\delta_\gamma(x) = \frac{\gamma/\pi}{x^2 + \gamma^2} \tag{1.18}$$

The expression of the Drude conductance can be obtained from equation 1.17 if the level spacing δ is the smallest energy scale. In this case, when ω, $\gamma \to 0$, equation 1.17 can be written :

$$\sigma_{Drude} = \frac{ne^2\tau}{m} \tag{1.19}$$

with τ the elastic scattering rate. It is worth noticing that in σ of equation 1.17 only the non-diagonal term of the current operator $\widehat{j}$ which is not the case in a ring geometry as we detail in the following.

(b) In a ring geometry

The formalism detailed above is valid only for a wire geometry, but in this PhD we considered the case of a ring. Due to its geometry, the conductance of a mesoscopic ring is different than the conductance of a simple wire. For instance, the sum rule we used in the last paragraphs doesn't hold anymore as the position operator x can take several values. However, with this ring geometry, a controllable experimental parameter exists : the flux $\Phi(t) = \Phi_{dc} + \delta\Phi(t)$ (with $\delta\Phi \ll \Phi_{DC}$). We derive here a few expressions, inspired by [5] and [6], and we start by introducing the necessary ingredients to derive the conductance of an isolated mesoscopic ring. First, we notice that due to the ring geometry, the potential and the wavefunctions are necessarily periodic in angle, meaning :

$$V(r, \theta + 2\pi, z) = V(r, \theta, z) \text{ and} |\Psi(r, \theta, z)\rangle = |\Psi(r, \theta + 2\pi, z)\rangle \tag{1.20}$$

We control the flux. The flux is related to the expression of the vector potential via :

$$A(t) = A_0 + \delta A(t) = \Phi(t)/L \tag{1.21}$$

And we still consider equation 1.7. To find the sum rule needed to solve this problem, we consider the changes in the Hamiltonian in second order of the experimentally controllable quantity $\delta\Phi$. The changes $\delta\mathcal{H}$ reads :

$$\delta\mathcal{H} = -\frac{e\delta\Phi}{L}\left(\frac{p - eA}{m}\right) + \frac{1}{2m}\left(\frac{e\delta\Phi}{L}\right)^2 \tag{1.22}$$

The change in energy of state n caused by this variation is evaluated using second order perturbation theory. The energy ε_n reads :

$$\begin{aligned} \varepsilon_n(\Phi + \delta\Phi) &= \varepsilon_n(\Phi) + \langle n|\delta\mathcal{H}|n\rangle + \sum_{l\neq n} \frac{|\langle n|\delta\mathcal{H}|l\rangle|^2}{\varepsilon_n - \varepsilon_l} \\ &= \varepsilon_n(\Phi) + \frac{\partial\varepsilon_n}{\partial\Phi}\delta\Phi + \frac{1}{2}\frac{\partial^2\varepsilon_n}{\partial\Phi^2}(\delta\Phi)^2 \end{aligned} \tag{1.23}$$

A comparison of the first order term gives :

$$\frac{\partial\varepsilon_n}{\partial\Phi} = -\langle n|j|n\rangle = -j_{nn} \tag{1.24}$$

and the second order term yields a new sume rule for the ring geometry :

$$\frac{1}{m} + 2\sum_{l} \frac{|\langle n|j|l\rangle|^2}{\varepsilon_n - \varepsilon_l} = \frac{L^2}{e^2}\frac{\partial^2 \varepsilon_n}{\partial \Phi^2} \tag{1.25}$$

This new sum rule yields a new expression for the conductivity of the ring, which can be decomposed in three parts [5] :

$$\sigma(\omega) = \sigma_{per} + \sigma_D + \sigma_{ND} \tag{1.26}$$

with

$$\sigma_{per} = \frac{i}{\Omega}\frac{L^2}{\omega}\frac{\partial}{\partial \Phi}\sum_n f_n j_{nn} \tag{1.27}$$

is linked to the presence of permanent current via the term $j_{nn} = -\partial E_n/\partial\Phi$. This term is purely reactive and stands for the response of the current when the flux is time-dependent. The two other terms are more interesting for the purpose of this manuscript. The term σ_D, "diagonal conductivity" (in a sense that it takes into account only the diagonal elements of the operator $\widehat{j}$), reads :

$$\sigma_D = \frac{i}{\Omega}\frac{L^2}{\gamma - i\hbar\omega}\sum_n \frac{\partial f_n}{\partial \Phi} j_{nn} \tag{1.28}$$

and is due to the finite relaxation time of the electrons. The term proporitonal to $-\frac{\partial E_n}{\partial \Phi}$ links this dissipation term to the current in the ring. Finally, the non-diagonal term (in a sense that it takes into account the off-diagonal term of $\widehat{j}$)

$$\sigma_{ND} = \frac{i}{\Omega}\frac{e^2}{m^2}\sum_{n,l\neq n} \frac{f_n - f_l}{\varepsilon_n - \varepsilon_l}\frac{|j_{nl}|^2}{\varepsilon_n - \varepsilon_l - \hbar\omega - i\gamma} \tag{1.29}$$

takes into account the transitions between levels in the ring. This contribution is exactly equal to the one of equation 1.17, hence it includes in the continous limit also the Drude conductance of the system.

1.2.3 . The fluctuation-dissipation theorem

(a) Noise and fluctuations

To characterize experimentally the noise, the spectrum analyzer measured the power it receives on a frequency bandwidth Δf and gives a quantity $S_v(f)$ the noise power density (V^2/Hz) which can be written :

$$S_v(f) = \frac{1}{\Delta f}\sum_{[f,f+\Delta f]} |V^2(f)| \tag{1.30}$$

This noise power density is related to the Fourier transform of the autocorrelation function (Wiener-Khintchine theorem) :

$$S_v(f) \equiv \int_{-\infty}^{+\infty} \langle V(t)V(t-\tau)\rangle e^{i2\pi f\tau} d\tau \tag{1.31}$$

(b) Historical overview

The link between the response of a system and the fluctuations started long before the proper theorem was derived by Kubo. In 1926 already Johnson observed that the voltage across an ordinary conductor is subject to fluctuations [7], and Nyquist derived a first expression linking dissipation and fluctuations :

$$S_v(f) = 4k_B T R \tag{1.32}$$

where R is the resistance. If we consider a conductor, the well-known Joule heating dissipates power as $P = RI^2$. However, even if $\langle I \rangle = 0$, fluctuations appear. Johnson and Nyquist attributed the non-zero voltage fluctuations to the thermal agitation of the electrons, creating a small but rapidly oscillating current in the conductor.

However for decades a more general form of this relation lacked until Callen and Welton proposed a more general link between those two quantities in 1957 [8]. They generalized Johnson, Nyquist and Einstein's results to one simple relation :

$$S_v(f) = 2hf \coth\left(\frac{hf}{2k_B T}\right)\mathcal{R}e(Z(f)) \tag{1.33}$$

known as the "quantum version" of the Johnson-Nyquist relation (or "generalized Nyquist relation" by Callen and Welton). $Z(\omega)$ in this expression is the "generalized" impedance of a system. This assumption was later expanded by Kubo [9] within the linear response theory, and we will describe a bit more this general result in the following.

(c) Derivation using linear response theory

For the sake of simplicity and because it is the main interest of this manuscript, we focus in the following on the current response to an external field. The field is described by the vector potential $A(t)$ and it couples to the current density as $j \times A(t)$. The response functions reads :

$$\chi_{jj}(t) = \frac{i}{\hbar}\theta(t)\langle [j(t), j(0)] \rangle \tag{1.34}$$

Let's define now the current fluctuations, defined by :

$$\begin{aligned} S_j(t) &= \langle j(t) j(0) \rangle \\ &= \mathrm{Tr}(\mathrm{e}^{-\beta \mathcal{H}_0} \mathrm{e}^{i\mathcal{H}_0 t} j(0) \mathrm{e}^{-i\mathcal{H}_0 t} j(0)) \end{aligned} \tag{1.35}$$

One can show that

$$S_j(t) = \langle j(-t - i\hbar\beta) j(0) \rangle = S_j(-t - i\hbar\beta) \tag{1.36}$$

or in Fourier space :

$$S_j(\omega) = \mathrm{e}^{\beta\hbar\omega} S_j(-\omega) \tag{1.37}$$

This function has two other properties that we will use :

$$S_j^*(t) = S_j(-t) \ , \mathcal{I}m(S_j(t)) = \frac{S_j(t) - S_j(-t)}{2i} \tag{1.38}$$

using this, we can write

$$\mathcal{I}m(S_j(t)) = \frac{1}{2i}[j(t), j(0)] \tag{1.39}$$

relating fluctuations to the susceptibility by :

$$\chi_{jj}(t) = -\frac{2}{\hbar}\theta(t)\mathcal{I}m(S_j(t)) \tag{1.40}$$

Again, in Fourier space it becomes :

$$\mathcal{I}m(S_j(\omega)) = -i\hbar\mathcal{I}m\chi_{jj}(\omega) \tag{1.41}$$

We combine equations (1.37) and (1.38) to obtain :

$$\mathcal{I}m(S_j(\omega)) = \frac{1 - \mathrm{e}^{\beta\hbar\omega}}{2i} S_j(\omega) \tag{1.42}$$

and we recover a general expression of the fluctuation-dissipation theorem :

$$S_j(\omega) = \hbar\mathcal{I}m(\chi_{jj}(\omega))[\coth(\beta\hbar\omega/2) + 1] \tag{1.43}$$

If we derive the response function as follows :

$$\begin{aligned} j(\omega) &= \sigma(\omega)E(\omega) \\ &= i\omega\sigma(\omega)A(\omega) \\ &= \chi_{jj}(\omega)A(\omega) \end{aligned} \tag{1.44}$$

we can relate the conductivity to the susceptibility via :

$$\sigma(\omega) = \frac{\chi_{jj}(\omega)}{i\omega} \tag{1.45}$$

we obtain directly the link between the fluctuations of the system, represented by $S_j(\omega)$ and the dissipation represented by the finite conductance $\sigma(\omega)$/ At temperature $T \ll \omega$, one recovers the expression of the Johnson-Nyquist noise of equation (1.32) but expressed in terms of current fluctuations.

The fluctuation-dissipation theorem, as long as it is verified, tells us that a measurement of current noise and conductance are equivalent. However, there exists several advantages in measuring noise : at high-frequency measuring the conductance of a system is not trivial. Some systems may be very sensitive to even very small perturbations, and dynamical effects can be a nuisance in these case (e.g. the Zener effect).

We try in the following to apply such concepts in the case of a normal metal in between two superconducting leads, and we start with a description of the superconducting proximity effect.

1.3 . Superconducting proximity effect

The superconducting proximity effect is a phenomenon occuring when a superconductor (S) is placed in contact with a non-superconducting material (described as "normal" N, "insulating" I, etc.) and the latter inherits the properties of a superconductor. This effect was first described theoretically by Josephson in 1962 [10] when the two superconducting materials are coupled by an insulating barrier called the weak link and observed a year later by Anderson and Rowell [11]. We first describe briefly the S-I-S junctions and the DC and AC Josephson effects. We then replace the insulating barrier by a normal metal and described how the proximity effect is changed in this case to finally described the different types of SNS junctions.

1.3.1 . DC and AC Josephson effect

We develop in this section the two Josephson equations that serve as the basis of the proximity effect. To do so, we consider the case of the SIS junction represented in Fig. 1.2. The superconductors are described by their wavefunctions written

$$\psi_j = \sqrt{n_j} e^{i\varphi_j} \quad j = 1, 2 \tag{1.46}$$

where n_j are the density of Cooper pairs and φ_j are the superconducting phases. If the electric potential difference across the junction is V, the energy difference between the two superconductors is $2eV$ as the charge of a Cooper pair is $2e$.

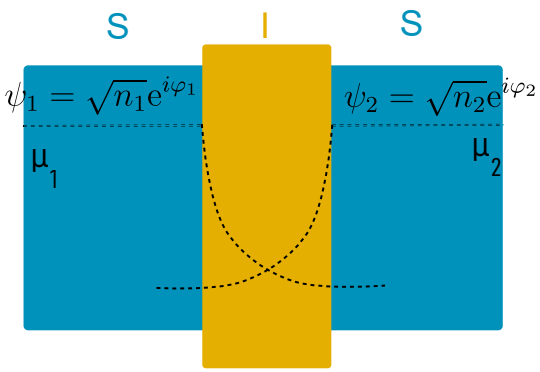

FIGURE 1.2 – Sketch of the considered Josephson junction, with in blue the superconductors (S) and in yellow the insulating barrier (I). The superconductors are described by their wavefunctions $\psi_j = \sqrt{n_j} e^{i\varphi_j}$, j = 1, 2. The dashed line represents $|\psi_j|$ across the junction. The energy difference between the two superconductors is given by $\mu_2 - \mu_1 = 2eV$ if a voltage V is applied.

The evolution the system is given by the coupled Schrödinger equations :

$$\begin{aligned} i\hbar \frac{\partial \psi_1}{\partial t} &= \mu_1 \psi_1 + \kappa \psi_2 \\ i\hbar \frac{\partial \psi_2}{\partial t} &= \mu_2 \psi_2 + \kappa \psi_1 \end{aligned} \tag{1.47}$$

where κ is a constant representing the coupling between the two superconductor.

We incorporate eq. 1.46 into eq. 1.47 to obtain :

$$\begin{aligned} \hbar\frac{\partial n_1}{\partial t} = -\hbar\frac{\partial n_2}{\partial t} = 2\kappa\sqrt{n_1 n_2}\sin(\varphi_2 - \varphi_1) \\ \hbar\frac{\partial(\varphi_2 - \varphi_1)}{\partial t} = \mu_2 - \mu_1 = 2eV \end{aligned} \tag{1.48}$$

The time-derivative of the density of Cooper pairs $\partial_t n_j$ yields a current I. Writing $\varphi = \varphi_2 - \varphi_1$ the phase difference between the two superconductors, and $I_0 = 2\kappa\sqrt{n_1 n_2}/\hbar$ equations 1.48 can be rewritten as :

$$I = I_0 \sin(\varphi) \tag{1.49}$$

$$\frac{\partial\varphi}{\partial t} = \frac{2eV}{\hbar} \tag{1.50}$$

known as the Josephson equations. Equation 1.49 shows that even at zero bias, a non-dissipative current flows through the non-superconducting link and this current is modulated by the phase difference between the two superconductors : this is the DC Josephson effect, and the relation between the current and the phase is called the Current-Phase Relation (CPR). Once a voltage bias is applied, the phase difference varies according to eq. 1.50 : even for a time-independent V, the supercurrent will oscillate at frequency $2eV/\hbar$. These two equations are the building block of the proximity effect. In the SIS picture, the Cooper pairs can tunnel from one superconducting lead to the other, yielding a supercurrent in the insulating part of the junction.

In SNS junctions, the proximity effect is not due to the tunneling of the Cooper pairs but takes its origin from an other mechanism called Andreev reflection [12], whose derivation relies on the excitations inside a superconductor.

1.3.2 . Bogoliubov-de Gennes equations and Andreev reflection : the NS interface

The elementary excitations in a superconductor are superpositions of electrons and holes quasiparticles called Bogoliubon. Formally, these excitations are described by spinors, with one component describing the electronic part and the other the hole. These spinors are derived from the Bogoliubov-de Gennes equations :

$$\begin{pmatrix} H - E_F & \Delta(\vec{r}) \\ \Delta^*(\vec{r}) & E_F - H^* \end{pmatrix} \begin{pmatrix} u(\vec{r}) \\ v(\vec{r}) \end{pmatrix} = E \begin{pmatrix} u(\vec{r}) \\ v(\vec{r}) \end{pmatrix} \tag{1.51}$$

where H is the Hamiltonian in absence of superconductivity, E_F the Fermi energy and Δ the superconducting order parameter. This formalism is well suited to describe inhomogenous superconductivity or at an interface when $\Delta = \Delta_0 e^{i\varphi}$ is space-dependent, therefore it is the one used to formally describe the problem at the NS interface.

Let us describe the problem at the NS interface. When an electron coming from the normal metal arrives at the NS interface, what it sees is a gap Δ in the density of states of the superconductor : there are no available states for the electron to

enter and it has to be reflected or to penetrate as an evanescent wave. This last process leads to the reflection as a hole of an electron arriving at the NS interface : this is the Andreev reflection depicted in Fig. 1.3.

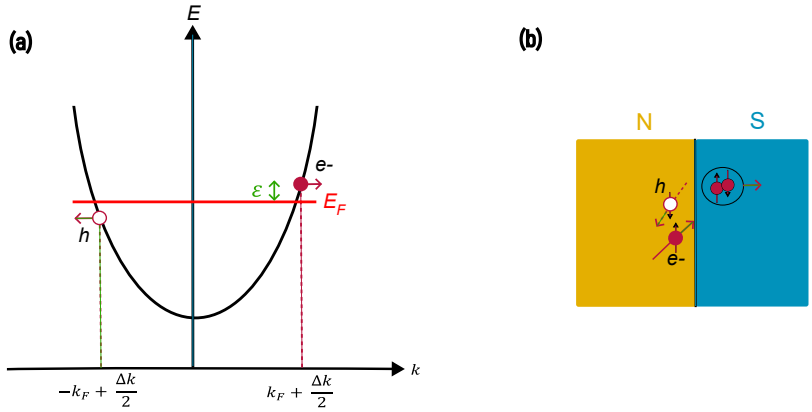

FIGURE 1.3 – (a) An electron of energy $E_F+\varepsilon$ and wavevector $k_F+\delta k/2$ is reflected as a hole of energy $E_F-\varepsilon$ and momentum $-k_F+\delta_k/2$. (b) Illustration of the Andreev reflection. The incident electron is retro-reflected as a hole. This process is equivalent of a transfer of Cooper pair inside the superconductor.

The Andreev reflection can be summarized as follows : the incident electron of energy $\varepsilon_e = E_F + \epsilon$ where E_F and wavevector $k_e = k_F + \Delta k/2$ arrives at the NS interface and is reflected as a hole of energy $\varepsilon_h = E_F - \varepsilon$ and wavevector $k_h = -k_F + \Delta k/2$. The Cooper pair has energy 2ε so that the energy is conserved in the process. The incoming electron and the reflected hole have quasi equal wavevectors (the difference being $2\varepsilon/\hbar v_F$) but opposite direction of motion shown in Fig. 1.3(b) : the Andreev reflection is a retro-reflection. At the interface, the hole acquires a phase $\varphi + \arccos(\varepsilon/\Delta)$, where φ is the phase of the superconductor, which is addeed to the original electron phase φ_e. If the quasiparticle arriving at the interface is a hole, it will also be retro-reflected as an electron. The inverse process also exists : if a Cooper pair arrives at the NS interface, it is transmitted as an electron-hole pair.

1.3.3 . Andreev bound states : the SNS junction

In an SNS junction, the Andreev reflection occurs at the two NS interfaces, as depicted in Fig. 1.4.

These reflections impose phase-dependent boundary conditions on the eigenstates of the non-superconducting region, that can be obtained by solving the Bogolioubov-de Gennes equations, and are coherent superpositions of electron and hole wavefunctions that are called Andreev bound states (ABS). Let us consider the case of ballistic transport in the normal region, and the electrons/holes travel perpendicularly to the NS interface. We describe each superconductor by its order parameter $\Delta e^{i\varphi_{L,R}}$ (L = left, R = right) and consider a Cooper pair coming from the left superconducting lead :

— This Cooper pair is first transmitted in the normal metal as an electron-hole pair at the left interface. The electron has energy ε slightly above E_F

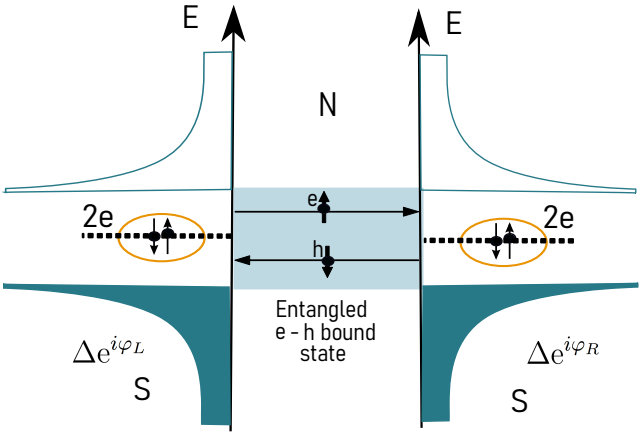

FIGURE 1.4 – Andreev reflections at both ends of a SNS junction, leading to the formation of entangled electron-hole bound states, called Andreev bound states.

and the the hole has an energy $-\epsilon$. Their phases are linked by the relation $\varphi_{e,L} - \varphi_{h,L} = \arccos(\varepsilon/\Delta)) - \varphi_L$.

— While propagating in the normal metal of length L_N, the electron acquires a phase $k_e L$. Its phase when arriving at the right interface is then $\varphi_{e,R} = \varphi_{e,L} + k_e L_N$.

— Another Andreev reflection occurs at the right interface and the electron is reflected as a hole. The phase of this hole is $\varphi_{h,R} = \varphi_{e,R} + \varphi_R + \arccos(\varepsilon/\Delta)$.

— The hole is propagating from the right to the left interface, acquiring a phase $k_h L_N$ when it arrives at the left interface.

This corresponds to a complete cycle, and the energy of the ABS can be found by equating the phase shift acquires during this cycle to an integer multiple of 2π, which corresponds to :

$$\frac{2\varepsilon_n L_N}{\hbar v_F} + 2\arccos(\frac{\varepsilon_n}{\Delta}) \pm \varphi = 2\pi n \qquad n \in \mathbb{N} \tag{1.52}$$

in which we wrote $\varphi = \varphi_L - \varphi_R$ as the superconducting phase difference and v_F the Fermi velocity. Equation 1.52 can be rewritten by replacing the term $2\varepsilon_n L_N/\hbar v_F$ by $\varepsilon_n L_N/\xi_S\Delta$ where $\xi_S = \hbar v_F/2\Delta$ is the superconducting coherence length. This equation can also be extended in the case of a disorder normal metal by considering an impurity potential given by $V(x) = V_s\delta(x-a)$ (in 1D) yielding :

$$\frac{L_N\varepsilon_n}{\xi_S\Delta} + 2\arccos(\frac{\varepsilon_n}{\Delta}) \pm \alpha = 2\pi n \quad [13] \tag{1.53}$$

where the phase α is given by :

$$\cos\alpha = \tau\cos\varphi + (1-\tau)\cos(\frac{L_N - 2a}{\xi_S}\frac{\varepsilon_n}{\Delta}) \tag{1.54}$$

where we introduced a finite transmission τ. Equation 1.53 gives the Andreev spectrum of the system. As we can see from this equation, the spectrum highly depends on the relative magnitude between ξ_S and L_N. This allows us to make a first dinstinction between two limits :

— The **short** junction limit, $L_N < \xi_S$.
— The **long** junction limit, $L_N > \xi_S$.

And a further distinction can be made when the transport in the normal metal is ballistic or diffusive, depending on the relative magnitude between l_e (the elastic mean free path) and L_N :

— The junction is said to be **ballistic** if $l_e > L_N$.
— The junction is said to be **diffusive** if $l_e < L_N$.

(a) Ballistic transport in the short and long regime

For simplicity, we consider first the short junction for a single channel of transmission τ. In this case, equation 1.53 when the first term is neglected gives :

$$\varepsilon^{\pm} = \pm\Delta\sqrt{1 - \tau\sin^2(\varphi/2)} \tag{1.55}$$

When the junction is clean, i.e. if we take $\tau = 1$, at phase $\varphi = \pi$ the spectrum is degenerates and there is no gap in the Andreev spectrum, but the degeneracy is lifted when $\tau < 1$ and it open a gap at phase π given by :

$$\delta = 2\Delta\sqrt{1 - \tau} \tag{1.56}$$

It is worth noticing that the energy spectrum doesn't depend on the length of the normal metal L_N in this case.

In the long ballistic limit, without the presence of an impurity, the spectrum is linear for $\varepsilon \ll \Delta$, according to :

$$\varepsilon_n = [((2n+1)\pi \mp \varphi]\frac{\xi_S}{L_N} \tag{1.57}$$

and we observe a degeneracy when the phase is an multiple of π. However, the spectrum is no more linear when the energy gets close to the superconducting gap. When we take into account the impurity, the spectrum becomes more rounded but also lifts the degeneracy as in the short regime, also opening a gap. Spectra in the short and long regime and in presence or not of an impurity are plotted in Fig. 1.5.

(b) Diffusive transport in the short and long regime

In the diffusive regime, the number of channels is not defined and we have to define a number of independent effective conduction channels denoted $M_{eff} = Ml_e/L_N$ and M computed as in the ballistic case. Several ABS states of different transmissions coexist in the normal metal. In the short regime, the diffusive Andreev spectrum is also given by :

$$E_n^{\pm} \pm \sqrt{1 - \tau_n\sin^2(\varphi/2)} \tag{1.58}$$

and instead of calculating the sum of the M_{eff} effective conducting channels, it is usually done by integration using the probability of transmission given by :

$$P(\tau) = \frac{\pi}{2e^2R_N}\frac{1}{\tau\sqrt{1-\tau}} \quad [14] \tag{1.59}$$

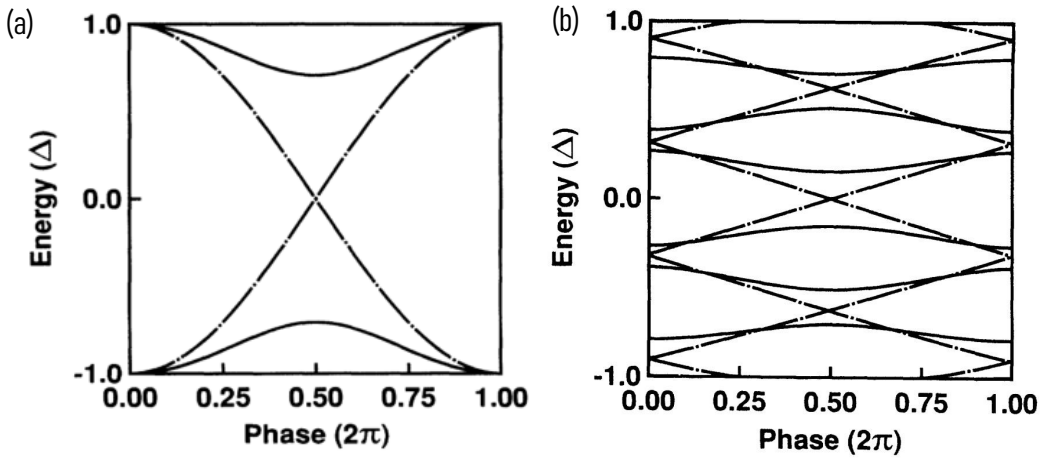

FIGURE 1.5 – Ballistic Andreev spectrum. (a) Short junction with (solid line) and without (dashed line) the presence of an impurity. The impurity opens a gap at phase π given by $\delta = \Delta\sqrt{1-\tau}$, lifting the degeneracy. (b) Long junction with (solid line) and without (dashed line) the presence of an impurity. The impurity rounds the spectrum while lifting the degeneracies at 0, π and 2π. From [13].

R_N being the normal state resistance. In the long diffusive regime, this approach is not possible, and the calculation of the spectrum can be either done using Green formalism or by numerical diagonalization of the Bogoliubov-de Gennes Hamiltonian. The spectra shown in Fig. 1.6 are obtained this way.

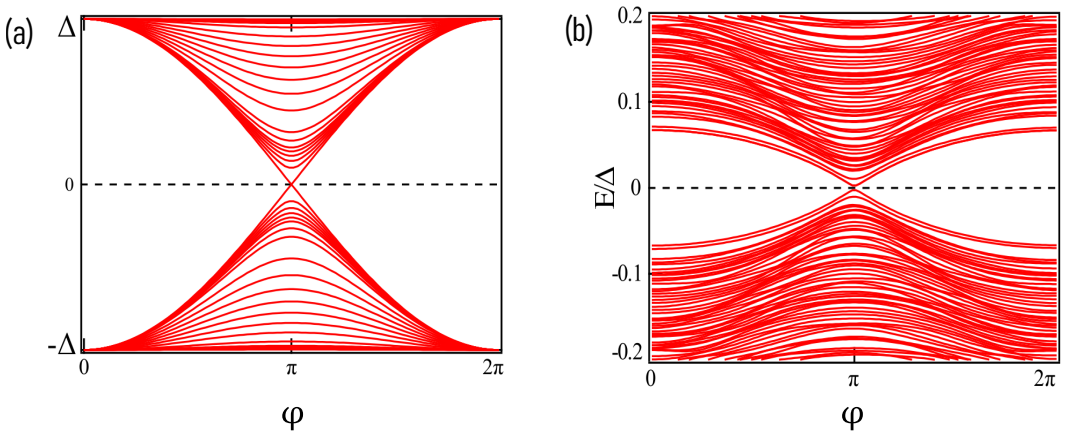

FIGURE 1.6 – Diffusive spectrum in the (a) short junction regime and (b) long junction regime. In the latter, a phase-dependent gap of amplitude much smaller than the superconducting gap appears : the minigap. From [15].

The long diffusive regime is interesting because of the apparition of a gap of amplitude much lower than Δ appearing. This so-called minigap is phase-dependent, and yields a new energy scale to the system, that we discuss in the following section.

(c) Characteristic energy scales

Up to now we described the different regimes in terms of length scales, but it can be more interesting to describe them in terms of energy scale. The first one is indeed the superconducting gap Δ, which we can compare to the characteristic energy of the ABS, the Thouless energy, defined as :

$$E_{Th} = \frac{\hbar}{\mathcal{T}} \tag{1.60}$$

with $\mathcal{T}$ the time for the Andreev pair to cross the junction, depending on the transport regime in each junction. This defines the Thouless energy as :

$$\begin{aligned} E_{Th}^{b} &= \frac{\hbar v_F}{L_N} \quad \text{for ballistic transport} \\ E_{Th}^{d} &= \frac{\hbar D}{L_N^2} \quad \text{for diffusive transport} \end{aligned} \tag{1.61}$$

with $D \approx \frac{1}{d} v_F l_e$ the diffusion coefficient in dimension d. This allows us to rewrite the definition of the short and long regime with :

$$\begin{aligned} \Delta &\ll E_{Th} \quad \text{for a short junction} \\ \Delta &\gg E_{Th} \quad \text{for a long junction} \end{aligned} \tag{1.62}$$

In the case of the long diffusive junction, the phase-dependent gap is also an important energy scale. Its amplitude and phase-dependence are given by the following equation :

$$E_g(\varphi) = 3.1 E_{Th} \times |\cos(\frac{\varphi}{2})| \tag{1.63}$$

1.3.4 . Current-phase relations

The derivation of the Andreev spectra in the different regimes of the previous sections is a first step towards the current-phase relations of the SNS junctions, which are more complex than the first Josephson relation of equation 1.49. The current carried by one Andreev level is given by :

$$i_n(\varphi) = \frac{2\pi}{\Phi_0} \frac{\partial \varepsilon_n}{\partial \varphi} \tag{1.64}$$

with $\Phi_0 = h/2e$ the superconducting quantum of flux. The total supercurrent in the junction is the sum of the single level currents multiply by their occupation probability given by the Fermi-Dirac distribution :

$$\begin{aligned} I(\varphi) &= \sum_n f_{FD}(\varepsilon_n) i_n(\varphi) \\ &= \frac{2\pi}{\Phi_0} \sum_n f_{FD}(\varepsilon_n) \frac{\partial \varepsilon_n}{\partial \varphi} \end{aligned} \tag{1.65}$$

The phase-dependence of the ABS spectrum then directly yields the phase-dependence of the current-phase relation and are summarized in Fig. 1.7

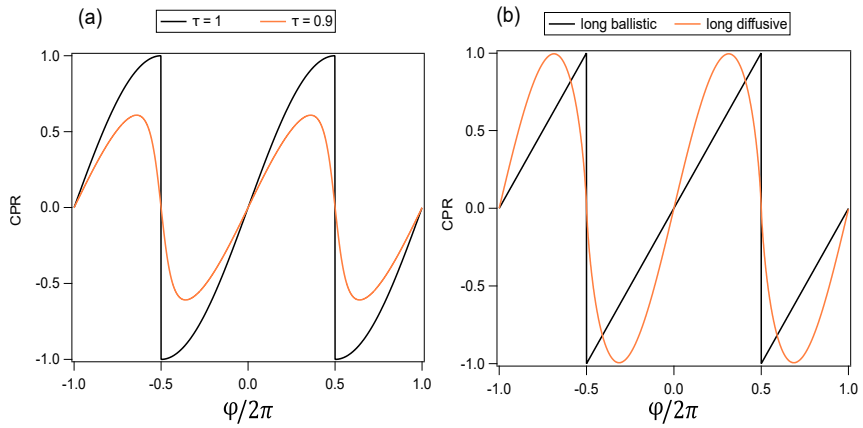

FIGURE 1.7 – Shape of the Current-Phase Relations in various regimes (a) In the short regime, for $\tau = 1$ (black) and $\tau = 0.9$ (orange). (b) In the long regime, with ballistic transport (black) and diffusive transport (orange).

As for the phase-dependence and the shape of the CPR, the amplitude of the critical current can also be deduced from the regime we consider, by the product $eR_N I_c$ where R_N is the normal state resistance and I_c the critical current at zero temperature [16] :

— For a short ballistic junction $eR_N I_c = \pi\Delta$ [17]

— For a short diffusive junction $eR_N I_c = 2.07\Delta$ [18]

— For a long ballistic junction $eR_N I_c = 10.82 E_{Th}$ [19]

— For a long diffusive junction, $eR_N I_c = E_{Th}$. [20]

We discuss now only the long junction. For a ballistic junction the normal state resistance is given by the quantum of resistance, $R_N = R_Q$ independent of the junction's geometry. This yields directly :

$$I_c^b = \frac{\hbar v_F}{eR_Q L_N} \tag{1.66}$$

whereas in the diffusive case, R_N can be developed using the Drude model. In this case, we have :

$$R_N = \frac{\rho L_N}{S} = \frac{m}{ne^2}\frac{L_N}{S}\frac{v_F}{l_e} \tag{1.67}$$

with $D \propto v_F l_e$, this yields a $1/L_N^3$ dependence for the critical current :

$$I_c^d \propto \frac{ne}{m}\frac{l_e^2}{L_N^3} \tag{1.68}$$

and we can compare the current in a ballistic junction with the critical current in the diffusive junction, yielding :

$$\frac{I_c^b}{I_c^d} \propto \left(\frac{L_N}{l_e}\right)^2 \tag{1.69}$$

The amplitude of the supercurrent is helpful to discriminate between ballistic and diffusive transport in a long SNS junction, and is therefore a powerful tool to study the transport in any kind of material.

1.4 . Noise and conductance of a superconducting junction : a two-level toy model

We consider in this part a superconducting quantum point contact of perfect transmission to illustrate the fluctuation-dissipation theorem in the simplest case of superconducting junction.

1.4.1 . Supercurrent noise in a superconducting and perfectly transmitting quantum point contact

We consider the case described by Averin and Imam in 1996 [21].

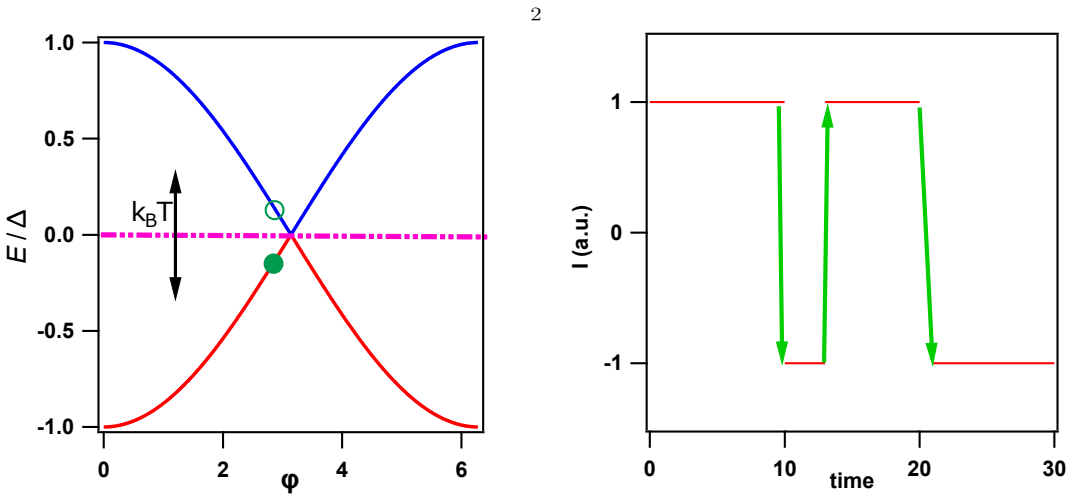

FIGURE 1.8 – Energy spectrum of our toy model and supercurrent fluctuations. The energy spectrum of a short ballistic junction, with one occupied level (filled green circle) and the excited state at the same phase (empty green circle). These two states carried an opposite supercurrent. The filled state can be thermally excited and the excited state can relax, yielding to the fluctuations in supercurrent, highlighted by the green arrows on the right graph.

Fig. 1.8 represents the energy spectrum with respect to the superconducting phase difference φ. We consider a two level system, with respective energies :

$$E_{\pm} = \pm\Delta\cos(\frac{\varphi}{2}) \tag{1.70}$$

yielding a current per level :

$$I_{\pm} = \mp\frac{\Delta}{2}\sin(\frac{\varphi}{2}) = \mp I(\varphi) \tag{1.71}$$

We consider now te instantaneous occupancy $n_{\pm} = 0, 1$ of each state E_{pm}. We thus have the relations :

$$n_{+} + n_{+} = 1 \tag{1.72}$$

$$\Delta n = n_{+} - n_{-} = \pm 1 \tag{1.73}$$

The total current at a given phase is the sum of the two single-level weighted by their occupation probability. In our case, we have :

$$\begin{aligned} I(t) &= n_+(t)I_+ + n_-(t)I_- \\ &= n_+(t)I_+ - n_-(t)I_+ \\ &= \Delta n(t)I_+ \end{aligned} \tag{1.74}$$

If we consider a finite relaxation time τ between the two states, the difference Δn obeys a master equation :

$$\frac{d\Delta n}{dt} = -\frac{\Delta n - \overline{\Delta n}}{\tau} \tag{1.75}$$

where $\overline{\Delta n}$ is the occupation at thermal equilibrium. With $\overline{n_{+,-}} = f_{FD}(\pm E(\varphi))$, we get $\overline{\Delta n} = \tanh \beta \frac{E(\varphi)}{2}$ where $\beta = 1/k_B T$ and we can solve eq. (1.75).

$$\Delta n(t) = (\Delta n(0) - \overline{\Delta n}) \exp(-\frac{t}{\tau}) + \overline{\Delta n} \tag{1.76}$$

Using $\Delta n(t)$ we can compute the current autocorrelation function :

$$\begin{aligned} \langle I(t)I(0)\rangle &= \langle([\Delta n(0)^2 - \overline{\Delta n}\Delta n(0)]\mathrm{e}^{-t/\tau} + \overline{\Delta n}\Delta n(0))I_+^2\rangle \\ &= [(\overline{\Delta n^2} - \overline{\Delta n}^2)\mathrm{e}^{-t/\tau} + \overline{\Delta n}^2]I_+^2 \end{aligned} \tag{1.77}$$

It is easier to compute :

$$\begin{aligned} \langle I(t)I(0)\rangle - \langle I(0)\rangle^2 &= [\overline{\Delta n^2} - \overline{\Delta n}^2]\mathrm{e}^{-t/\tau} I_+^2 \\ &= (1 - \tanh^2((\varphi)/2))\mathrm{e}^{-t/\tau} I_+^2 \\ &= \frac{1}{\cosh^2(\frac{\beta E(\varphi)}{2})}\mathrm{e}^{-t/\tau} I_+^2 \end{aligned} \tag{1.78}$$

And the current noise spectrum can be defined as :

$$\begin{aligned} S_I(\omega) &= 2 \times \mathcal{R}\mathfrak{e}(\mathfrak{F}(\langle I(t)I(0)\rangle) \\ &= 2\frac{1}{\cosh^2(\frac{\beta E(\varphi)}{2})} I_+^2 \times \mathcal{R}e(\frac{1}{1/\tau + i\omega\tau}) \\ &= 2\frac{I^2(\varphi)}{\cosh^2(\frac{\beta E(\varphi)}{2})} \frac{\tau}{1 + \omega^2\tau^2} \end{aligned} \tag{1.79}$$

where the factor 2 accounts for the negative and positive frequencies.

1.4.2 . Conductance of the quantum point contact

We introduce a small time-dependent component in the superconducting phase difference of the junction and we want to detail the response of the system to such perturbation.

$$\varphi(t) = \varphi_0 + \delta\varphi \mathrm{e}^{-i\omega t} \tag{1.80}$$

with $\delta\varphi \ll \varphi_0$. Hence now we have $I(t) = \frac{\Delta}{2}\sin(\frac{\varphi_0+\delta\varphi e^{-i\omega t}}{2})$ with :

$$\sin(\frac{\varphi_0 + \delta\varphi e^{-i\omega t}}{2}) \approx \sin(\frac{\varphi_0}{2}) + \cos(\frac{\varphi_0}{2})\delta\varphi e^{-i\omega t} \tag{1.81}$$

by keeping only the first order contributions. The small perturbation in φ yields a small perturbation in Δn that we write :

$$\Delta n(t) = \overline{\Delta n}(\varphi(t)) + \delta\Delta n(t) \tag{1.82}$$

where $\overline{\Delta n}(\varphi(t))$ is an "instantaneous" equilibrium : it follows adiabatically the phase. Equation 1.75 is now :

$$\frac{d\Delta n(t)}{dt} = -\frac{\Delta n(t) - \overline{\Delta n}(\varphi(t))}{\tau} \tag{1.83}$$

yielding the following equation for $\delta\Delta n(t)$:

$$\begin{aligned}\frac{d\Delta n(t)}{dt} &= \frac{\partial\delta\Delta n}{\partial t} + \frac{\partial\overline{\Delta n}}{\partial\varphi}\frac{\partial\varphi}{\partial t} \\ &= -i\omega\delta\Delta n(t) + \frac{\partial E}{\partial\varphi}\frac{\partial\Delta n}{\partial E}(-i\omega)\delta\varphi e^{-i\omega t} \\ &= -\frac{\delta\Delta n}{\tau}\end{aligned} \tag{1.84}$$

Developing the derivatives, eq. 1.84 can be expressed as :

$$-\frac{\delta\Delta n}{\tau} = -i\omega\delta\Delta n + i\omega\delta\varphi e^{-i\omega t}\frac{\Delta}{2}\sin(\varphi(t)/2)\frac{\beta}{2}\frac{1}{\cosh^2(\beta E(\varphi)/2)} \tag{1.85}$$

in which we recognize the expression of $I(\varphi(t))$, so that we get :

$$\delta\Delta n = i\omega\varphi I(\varphi)\frac{\beta}{2}\frac{1}{\cosh^2(\beta E(\varphi)/2)}\frac{\tau}{i\omega\tau - 1} \tag{1.86}$$

We incorporate this expression in $I(t)$, and keep only the first order terms :

$$\begin{aligned}I(t) &= [\frac{\Delta}{2}\sin(\varphi_0/2) + \frac{\Delta}{2}\delta\varphi e^{-i\omega t}\cos(\varphi_0/2)](\overline{\Delta n} + \delta\Delta n) \\ &= \frac{\Delta}{2}[\sin(\varphi_0/2)\tanh(\beta E(\varphi)/2) \\ &+ \delta\varphi e^{-i\omega t}\cos(\varphi/2)\tanh(\beta E(\varphi)/2) \\ &+ \sin(\varphi/2)\frac{\tau}{i\omega\tau - 1}i\omega\delta\varphi e^{-i\omega t}\sin(\varphi/2)\frac{\beta}{2}\frac{1}{\cosh^2(\beta E(\varphi)/2)}]\end{aligned} \tag{1.87}$$

The admittance Y of the system is defined as :

$$Y = \frac{\delta I(\varphi(t))}{i\omega\delta\varphi e^{-i\omega t}} \tag{1.88}$$

The part of interest here is the conductance, i.e. the real part of the admittance Y. We finally get :

$$G = \frac{1}{2k_BT} \frac{I^2(\varphi)}{\cosh^2(\beta E(\varphi)/2)} \frac{\tau}{1+(\omega\tau)^2} \tag{1.89}$$

Similar to the expression of conductance for a metallic ring derived by Büttiker and Landauer in 1985 [22]. As pointed out by Averin, Bardas, Imam and by Yeyati and Martin Rodero [21, 23], the phase-dependence of $G(\varphi)$ gives the phase-dependence of the supercurrent noise due to the fluctuation-dissipation theorem. With our two-level model, the direct comparison between equations (1.79) and (1.89), we obtain directly :

$$S_I(\varphi) = 4k_BTG(\varphi) \tag{1.90}$$

This derivation shows that we can, from simple arguments, expect a supercurrent thermal noise for a superconducting junction. This supercurrent thermal noise is associated with a finite conductance via the fluctuation-dissipation theorem.

In this PhD, we investigated a long junction in the long diffusive regime, that is to say we investigated a system we much more channel than the one describe above. We summarize the contributions to the conductance of such system in the following section.

1.4.3 . Susceptibility of a long diffusive SNS junction

The analytical derivation of χ using linear response theory has been done previously by B. Dassonneville, and the next section summarizes this work to further understand the results that are presented in this work. Before going to the analysis on the susceptibility, we describe briefly the system we are interested in : the long diffusive SNS junction. In this case, we consider the Andreev spectrum shown in Fig. 1.6(b)).

The response of the diffusive NS ring is obtained the same way we obtained the response of the normal ring in section 1.2.2. In this part, we recall results described in [24] and explain the different mechanisms behind the susceptibility in our system.

We recall first that several energy scales coexist in this system : temperature k_BT, frequency $\hbar\omega$, minigap E_g and inelastic relaxation $h\gamma$. If we consider $k_BT \ll E_g$ (for instance at phase 0), thermal excitations are suppressed and then a priori no fluctuations in the supercurrent are expected.

We start with ω small compared to the other energy scales and internal time scales of the junction. In this case, the system follows adiabatically the excitation and the susceptibility is just the derivative of the supercurrent with respect to the phase. This term is due to the phase-dependence of the Andreev spectrum and does not depend on the frequency : it is a purely reactive term and it is written :

$$\begin{aligned} \chi' &= \frac{-2\pi}{\Phi_0} \frac{\partial I}{\partial \varphi} \\ \chi'' &= 0 \end{aligned} \tag{1.91}$$

When the frequency is of the order of magnitude to the inelastic scattering rate γ, some levels are driven out-of-equilibrium due to the dynamic variations of Andreev states within the same level [18]. This contribution is noted χ_D for diagonal as it stems from the diagonal elements of the current matrix J_{nm}. This quantity is complex, meaning its imaginary part describes a dissipative behaviour.

$$\chi_D = -\frac{i\omega}{\gamma - i\omega} \sum_n |J_{nn}|^2 \frac{\partial f_n}{\partial \varepsilon_n} \tag{1.92}$$

This expression is similar to the diagonal conductivity presented in section 1.2.2 and is only due to the finite relaxation time towards equilibrium.

Finally, we compare ω to the minigap. The excitation can induce transition between levels, even when the temperature is lower than the minigap.

$$\chi_{ND} = -\sum_{n,n\neq m} |J_{nm}|^2 \frac{f_n - f_m}{\epsilon_n - \epsilon_m} \frac{i\hbar\omega}{i(\epsilon_n - \epsilon_m) - i\hbar\omega + \hbar\gamma} \tag{1.93}$$

The three mechanisms presented are illustrated and summarized in Fig. 1.9.

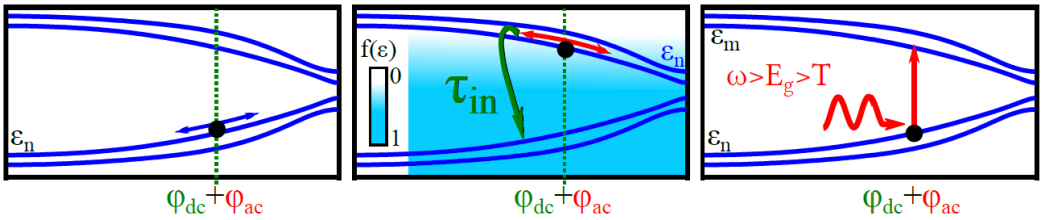

FIGURE 1.9 – Different mechanism responsible of the non-zero susceptibility. (Left) : when the excitation frequency is small compared to the other energy scales, the system follows adiabatically the excitation. The quantity measured is then the derivative of the current-phase relation and is purely reactive. (Middle) When the the frequency is on the order of the inelastic scattering rate of the ABS. The dissipative component is directly related to the non-dissipative current flowing at equilibrium and is denoted χ_D. (Right) Illustration of the microwave induced transitions, when $\omega > E_g > T$. From [24].

In the previous experiments in our group, the resonators were multimode and working at higher frequency ($\approx$ GHz) whereas we chose to work with a single mode resonator to prevent the coupling with the electromagnetic environment. The main idea for the future is to probe the supercurrent noise in a junction made with a topological insulator, for instance bismuth nanowires [25], Bi_4Br_4 or WTe_2, materials studied in our group. In those experiment, it has been shown that γ is within the kHz ([26]) to the GHz frequency scale. The topological signatures resides in the diagonal contribution [27]. Working in the regime where χ_D is maximal (i.e. $\omega\tau_{in} = \omega/\gamma \approx 1$) hints towards the working frequency interesting and relevant for the experiment.

The main goal of this first experiment is to verify that we are able to measured the supercurrent thermal noise of the NS ring and understand its link to dissipation

in the relatively well known case of an SNS junction. The measurements on the gold-based SNS junctions [28, 29], as well as the theoretical predictions for the long and diffusive SNS junction [15] allows to work on a well known system. By measuring both the susceptibility and the thermal noise (and ensuring the validity of the fluctuation-dissipation theorem for such hybrid systems), we provide a way of determining the conductance of these devices without any contact at thermal equilibrium.

2 - Supercurrent noise in a phase-biased superconductor-normal ring in thermal equilibrium

In SNS junctions, the supercurrent is mediated via ABS controlled by the phase difference between the two superconductors. Theory has long predicted significant noise of such supercurrent in equilibrium due to thermal excitation between the ABSs. Via the fluctuation-dissipation theorem (FDT), this leads to a finite dissipative conductance that coexists with the supercurrent bit is hidden in dc measurement. In this part of the thesis we directly measure the supercurrent noise at radio frequency in a phase-biased SNS ring inductively coupled to a superconducting resonator. We also measure the admittance of the same system whose real part is the dissipative conductance and quantitatively verify the FDT relation of the SNS ring.

In section 2.1 we detail the concept of conductance for a phase-biased Josephson junction in a ring geometry and show how to measure it via radio frequency susceptibility measurement. Section 2.2 is dedicated to the description of the experimental setup, the fabrication of the sample and the modeling of the transmission measurement. In section 2.3 we describe the calibration precedure and present the experimental results on section 2.4. Finally we give theoretical insights using numerical calculations to analyze these results in section 2.5.

2.1 . Conductance of a phase-biased Josephson junction in a ring geometry.

2.1.1 . Defining the conductance of a superconducting junction

Classically, the conductance of a normal conductor is defined by the small variations of current induced by a small variation of voltage in the linear regime :

$$G = \frac{\partial I}{\partial V} \tag{2.1}$$

However for a SNS junction, this standard way of measuring becomes hard to imagine. If we current bias an SNS junction, a supercurrent exists until the critical current is reached, characterized by a jump in the resistance : there is no linear regime. A rigorously pure DC voltage bias is impossible considering that the DC resistance of the junction is 0 and, even if it was, the AC Josephson effect would result in a non-linear regime.

However, the conductance can be well defined at finite frequency and measured by realizing a flux biasing in a ring geometry. This gives, according to Lenz law :

$$V = -\frac{\partial \Phi}{\partial t} \tag{2.2}$$

The flux Φ through the ring is related to the superconducting phase difference φ by :

$$\varphi = -2\pi \frac{\Phi}{\Phi_0} \tag{2.3}$$

where $\Phi_0 = h/2e$ is the superconducting flux quantum. Applying a time-dependent flux means controlling the phase difference of the junction : this is the so-called **phase biasing**. Indeed, it is equivalent to apply a voltage :

$$V = \frac{\Phi_0}{2\pi}\frac{\partial\varphi}{\partial t} \tag{2.4}$$

This phase/flux biasing allows to define a susceptibility :

$$\chi = \frac{\partial I}{\partial \Phi} \tag{2.5}$$

In the linear regime, all the physics is encoded in this response function. χ is complex and we further decompose it into its real and imaginary part $\chi = \chi' + i\chi''$. The real part χ' represents the in-phase response of the system to a finite frequency phase-biasing and is seen as an inductive response in the following. The out-of-phase part χ'' represents the dissipative response, i.e. the conductance of the ring, and is obtained via the relation :

$$G = \frac{\chi''}{\omega} \tag{2.6}$$

The susceptibility is directly related to the admittance Y of the system using :

$$Y = i\omega\chi \tag{2.7}$$

The ring geometry and the application of a flux then allows us to extract the admittance of the system. However, using this method, we extract the ring's response to an excitation and not directly the junction's one. In the subsequent part, we detail the effect of flux screening in our measurement.

2.1.2 . Ring's response and junction's response : screening effect

Due to the finite inductance of the loop and the diamagnetic nature of the superconducting junction, the flux that modifies the phase difference across the junction and the flux passing through the ring are not exactly equal : this is the screening effect. We consider the case of the isolated ring represented in Fig. 2.1.

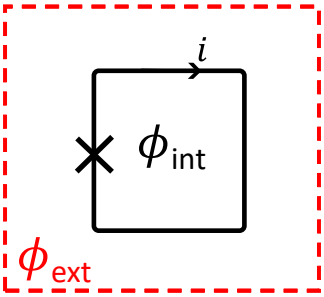

FIGURE 2.1 – Sketch for the screening effect. The junction is represented as a cross whereas the black lines represent the superconducting ring. The red dashed box can be seen as a "black box". This black box is the physical object we probe.

The current in the junction evolves with Φ_{int}, so that the current phase relation is given by $I_J(\Phi_{int})$. However, the ring's response χ_{ring} is obtained via Φ_{ext}

$$\chi_{ring} = \frac{\partial I_S}{\partial \Phi_{ext}} \tag{2.8}$$

whereas the junction's response is given by

$$\chi_j = \frac{\partial I_S}{\partial \Phi_{int}} \tag{2.9}$$

The external and internal flux are linked by the relation :

$$\Phi_{int} = \Phi_{ext} + L_l I_S(\Phi_{int}) \tag{2.10}$$

where L_l is the inductance of the superconducting loop. Equation 2.10 gives a direct relation between the ring's response and the junction's response :

$$\begin{aligned} \chi_{ring} &= \frac{\partial I_S}{\partial \Phi_{ext}} \\ &= \chi_J \frac{\partial \Phi_{int}}{\partial \Phi_{ext}} \\ &= \chi_J (1 + L_l \chi_{ring}) \end{aligned} \tag{2.11}$$

inverting this last equation gives the relation between χ_{ring} and χ_J :

$$\chi_{ring} = \frac{\chi_j}{1 - L_l \chi_j} \tag{2.12}$$

We now know what quantity we want to measure, and in the next section we introduce the experimental setup used to measure either the susceptibility, either the thermal noise of such systems.

2.1.3 . Susceptibility measurement : coupling a Josephson junction to a resonator

In this part we present the basic ideas to measure the response of a SNS junction to a finite frequency excitation. This technique has been developed by H. Bouchiat and B. Reulet and consists on coupling inductively the ring to a superconducting resonator, as illustrated in Fig. 2.2(a). This technique has been used previously in our group to study the dynamical effects of long SNS junction [30], to probe the mechanism behind dissipation in hybrid superconducting systems [24] and applied to more exotic materials such as higher-order topological insulators [27]. To measure the susceptibility, we need a DC component Φ_{DC} and an AC component Φ_{AC}. The DC flux is provided by a superconducting coil creating a DC magnetic field. The AC phase bias is provided by the superconducting resonator. The current in the resonator oscillates at a frequency ω and creates an AC flux $\Phi_{AC} = \delta\Phi \sin(\omega t)$ in the loop. This AC phase bias generates a current response in the loop. This current generates in turn an AC flux and modifies the resonance of the resonator and its quality factor. Those shifts in resonance frequency and quality factor are the quantities measured experimentally. The reactive and dissipative part of the susceptibility can be deduced from δf and $\delta(1/Q)$ respectively, which will be derived later (see equations 2.32 and 2.33). By scanning Φ_{DC}, we vary the phase from 0 to 2π and probe the whole spectrum of the junction, as illustrated in Fig. 2.2(b).

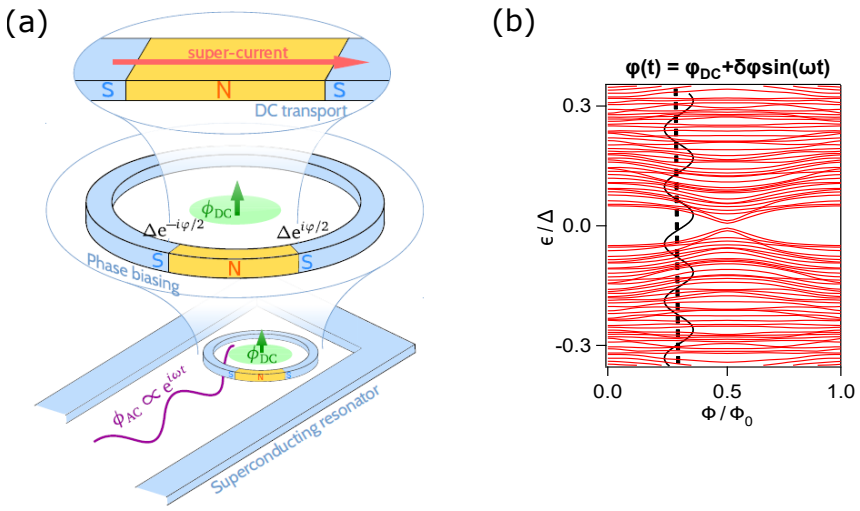

FIGURE 2.2 – Principle of the experiment. (a) the NS ring is inductively coupled to a superconducting resonator, the latter being characterized by its resonance frequency f_r and quality factor Q. The supercurrent in the resonator oscillates at frequency $\omega_r = 2\pi f_r$ providing a small AC flux Φ_{AC} inside the ring, modifying the current in the loop. This ac current modifies the resonance frequency and quality factor of the resonator. Those shifts are related to the susceptibility χ of the ring as detailed in section 2.2.3. From [31]. (b) Illustration of the phase biasing on the long diffusive Andreev spectrum. By scanning the phase φ_{DC} from 0 to 2π, we probe the entire spectrum.

2.1.4 . Noise measurement in the same configuration

Whereas in the susceptibility measurement the resonator is excited via the ac generator, in the noise measurement no power is sent to the resonator. This means that $\Phi_{AC} = 0$ in this measurement and we only vary Φ_{DC}. What we measure is the time dependence of the voltage at the output of the resonator, and the noise is obtained from the Fourier transform of this signal using an oscilloscope with the spectrum analysis function (TELEDYNE Lecroy HRO WaveRunner 6 Zi). Finally, because Because of the small coupling between the ring and the resonator, the expected noise signal is small and we had to develop a cryogenic amplifier adapted for this measurement.

2.2 . Experimental setup

Now that the principle of the experiment has been introduced, we detail the specificity of the experiment. We start by introducing the amplifier used in our experiment in section 2.2.1. This amplifier is directly connected to the sample (the superconducting resonator coupled to the ring), and we detail its fabrication before describing the sample and its fabrication process in section 2.2.2. Finally, we link the junction's inductance and conductance to the ring's and to the physical quantities measured in section 2.2.3, and detail the terms appearing in the total thermal noise

we measure.

2.2.1 . The CryoHEMT amplifier

The primary tool for building this experiment is chosing the best amplifier to detect the noise. Several tests were performed to optimize the amplifier.
We are looking for a setup that allows us to measure directly the total voltage across the resonator. For microwave systems, the standard technique is to use RF amplifiers with an input impedance of 50 Ω. This adds a lot of dissipation in the circuit, resulting in the reduction of the quality factor. The conventional solution it to use a coupling capacitance, but it acts as a voltage divider and by definition a fraction of the signal is lost.
To preserve both the quality factor and access the whole signal, the idea we had was to use a high impedance amplifier (whose impedance was higher than the resonator's impedance on resonance) designed in collaboration with Y. Jin's team. At high frequency, the current noise dominates. The CryoHEMT fabricated by their team are very low noise. The current noise increases with frequency, going from 0.06 fA/$\sqrt{\text{Hz}}$ at 1kHz to 2 fA/$\sqrt{\text{Hz}}$ at 1MHz, while the voltage noise decreases from 1.4 nV/$\sqrt{\text{Hz}}$ to 0.25 nV/$\sqrt{\text{Hz}}$ within the same frequency range [32]. Above 200 MHz the current noise of such amplifier is too important and is one of the reasons we limited our experiment to about 100 MHz, which could be sufficient for adapting the system to topological insulators. We further discuss some characteristics of this amplifier as well as its advantages in our systems by detailing the circuit model shown in Fig. 2.3

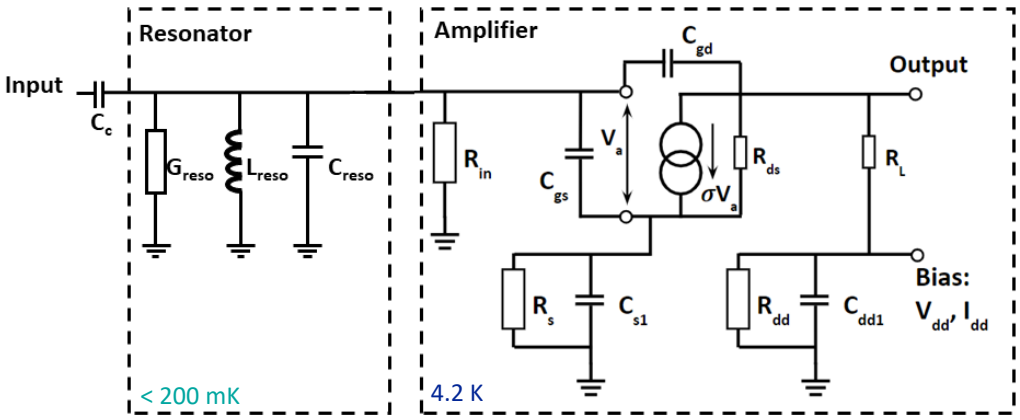

FIGURE 2.3 – Circuit model of the cryogenic HEMT amplifier design, modeled as voltage-controlled current source, directly connected to the resonator. The resonator is coupled to the RF power source via the coupling capacitance C_c and is thermally anchored to the mixing chamber of the dilution refrigerator, reaching temperatures of the order of the mK range. The amplifier is placed on the 4.2 K stage.

— The input impedance of the amplifier is $R_{in} = 1.3$ GΩ at 100 MHz, considerably larger than the loss resistance of the resonator, preserving the quality factor of the resonator.

— The output impedance is $Z_{out} = R_{ds}||R_L = 50\,\Omega$ and it matches the impedance of the transmission line.
— The transconductance is $\sigma = 42.5$ mS, giving an unloaded gain $\sigma Z_{out} = 2.26$.
— The loaded gain (obtained when connecting a 50Ω at the output of the amplifier) $g = 1.13$ is small, but it limits the Miller effect [33], which changes C_{gs} and C_{gd} to $C_a = C_{gs} + (1+g)C_{gd}$ the effective input capacitance of the amplifier. The bigger the gain, the bigger the effective capacitance yielding to an effect on the resonance frequency $1/\sqrt{LC}$ and quality factor $Q = RC\omega$, (with $C = C_{reso} + C_a + C_c \approx C_{reso}$).

The signal is further amplified using three cascaded room temperature amplifiers with low voltage noise (the voltage noise of the first amplifier is around 1 nV/$\sqrt{\text{Hz}}$), adapted to 50 Ω for a total measured gain at 100 MHz of 14125.

2.2.2 . Sample fabrication

(a) Design of the resonator

The superconducting resonator has then to match the working frequency of the amplifier. The resonator is fabricated using a LC circuit by e-beam lithography. To reach a frequency range on the order of 100 MHz, one needs relatively high value for L and C. We start with the inductive component. Since the inductance is proportional to the length (see eq. 2.13), the meander lines should be long enough to reach these relatively low frequencies and it makes the fabrication harder. To avoid the problem of size, we chose a material with a non-negligible kinectic inductance and use a coplanar stripline resonator as shown in Fig. 2.4. The total inductance $L = L_{geo} + L_{kin}$ is generated by the superconducting meander lines, where the geometric inductance L_{geo} is determined by the length of the meander while the kinetic inductance L_{kin} is determined by the superconducting gap Δ and the disorder. We can approximate them via the relation :

$$\begin{aligned} L_{geo} &\approx \mu_0 \times l \\ L_{kin} &= \frac{R_\square h}{2\pi^2 \Delta_0} \times \frac{l}{w} \end{aligned} \tag{2.13}$$

where l and w are respectively the length and the width of the meander lines, $R_\square = R/\square$ is the material's square resistance and depends also on the metal thickness. 80 nm thick Molybdenum-Rhenium compound was used as the superconducting material. Its kinetic inductance per square is $L_{K,\square} = 9$ pH/$\square$. Using this material has several advantages :

— The superconducting meander lines can be shorter and then fits in the window of the e-beam lithography : if only the geometric inductance was considered, the resonator could not fit in a square of 2 mm × 2 mm. This problem can be solved using a material with relatively high kinetic inductance.
— The design of the coupling inductance, in parallel with the junction (see Fig. 2.4). The signal we want to measure is proportional to $L_c I_c$ with L_c the value of the coupling inductance. Thanks to the kinetic inductance and by

playing with the geometry (with the number of "squares"), a correct coupling can be obtain even on a small length.

Because it is hard to fit a high enough capacitance in a square 2 mm × 2 mm designed by e-beam lithography, we use lumped components mounted on a printed circuit board directly bonded to the resonator for both the coupling capacitance to the RF generator and for the capacitance of the resonator. We use special capacitances working at low temperature [34]. A picture of the fabricated system resonator and the coupling to the NS ring is shown in Fig. 2.4, and the values of the inductances and capacitances considered are detail in tab. 2.1

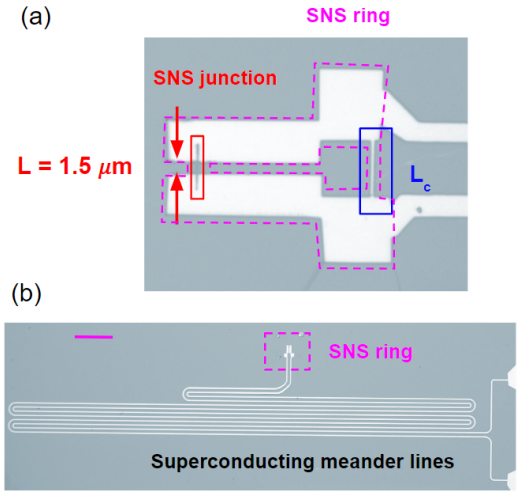

FIGURE 2.4 – Optical image of the sample. **(a)** The SNS ring, (magenta dashed lines) and the SNS junction (red rectangle). The inductive coupling L_c is highlighted by the blue rectangle. **(b)** A large scale image of the sample, showing the SNS ring (magenta rectangle) and the superconducting meander lines. Scale bar : 60µm

L_{reso}	40 nH
C_{reso}	47 pF
L_c	200 pH
C_c	1.2 pF

TABLE 2.1 – Designed inductances of the resonator and the coupling to the junction, and chosen resonator's and coupling capacitance to the generator.

(b) Lithography and metal deposition

The sample is fabricated with two steps of standard electron beam lithography. We use a chemical semi-amplified positive e-beam resist (CSAR) [35] with high spatial resolution on a SiO_2/Si chip.

— The first lithography step defines the normal part of the NS ring, the red rectangle on Fig. 2.4. It is a wire of length l = 1.5 μm and width w = 100 nm.

5 nm of titanium and 100 nm of gold are then deposited by electron-beam evaporation.
— After deposition and a second deposition of resist, there is a second step of e-beam lithography to define the superconducting meander lines and the coupling inductance.
— Once the resonator is defined, we etch slightly the gold wire by ion beam etching (IBE) to improve the contact between the gold wire and the metal deposited in the next step.
— Shortly after IBE, 80 nm of MoRe is deposited by sputtering in Argon gas.

Finally, the chip is dipped in dioxolane for about an hour for the lift-off process.

2.2.3 . Modeling the transmission and noise measurements

(a) Transmission measurement : inductance and conductance of the ring

In this part we model the SNS ring coupled to the resonator and obtain the link between the total inductance, the inductance of the ring and its relation with the inductance of the junction, as well as its dissipative part i.e. the effective conductance of the ring. We start by describing the circuit consisting of the SNS junction inconporated in the resonator, forming the NS ring. In this part, we consider the sample as presented in the optical image Fig. 2.4. We build step by step the expressions of the inductance of the system as a function of the admittance (or equivalently susceptibility) of the junction.

In the following process, the circuit is modeled with :

— $Z_j = i\omega L_j + 1/G_j = 1/Y_j$ is the impedance of the junction.
— L_c is the coupling inductance, closing the loop. It is shared with the superconducting resonator.
— L_l is the inductance of the loop, including the coupling inductance closing it. Therefore, the loop without considering the coupling inductance is described by the inductance $L_l - L_c$. These two values can be approximated by their designed value.
— L_{reso} is the intrinsic inductance of the closed superconducting resonator, therefore $L_{reso} - L_c$ is the total inductance due to the meander lines and the inductance to be considered during the calculation.
— G_{reso} is the total conductance of the resonator.

We start first by writing the impedance of the NS ring.

$$Z(\Phi) = i\omega L_c + \frac{\omega^2 L_c^2}{i\omega L_l + 1/Y_j(\Phi)} \quad (2.14)$$

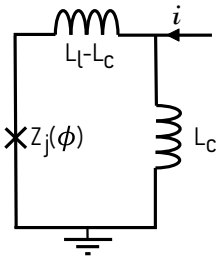

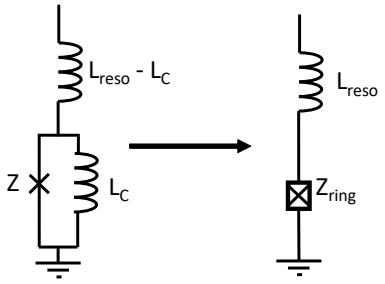

To the previous circuit we add the intrinsic inductance of the resonator $L_{reso} - L_c$ since the ring and the resonator share the coupling inductance. This step is to transform the circuit on the left to the totally equivalent circuit on the right, Z_{ring} describing the impedance of the ring. It reads :

$$Z_{ring}(\Phi) = +\frac{\omega^2 L_c^2}{i\omega L_l + 1/Y_j(\Phi)} \tag{2.15}$$

If our case we can assume $Z_{ring} \ll \omega L_{reso}$ and we have for the conductance of the resonator with the NS ring :

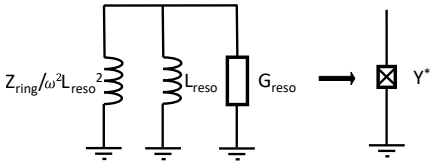

$$(i\omega L_{reso} + Z_{ring}(\Phi))^{-1} \approx \frac{1}{i\omega L_{reso}} + \frac{Z_{ring}(\Phi)}{\omega^2 L_{reso}^2} \tag{2.16}$$

This is the transformation represented on the right, to which we added the conductance of the resonator G_{reso} to modelize the losses.

Finally, this yields the admittance of the system consisting of the ring coupled to the resonator Y^*

$$Y^*(\Phi) = \frac{1}{i\omega L_{reso}} + \frac{L_c^2}{L_{reso}^2}\frac{Y_j(\Phi)}{1 + L_l Y_j(\Phi)} + G_{reso} \tag{2.17}$$

And by expressing this in terms of the susceptibility $\chi_j = -i\omega Y_j$, which we decompose in real and imaginary part as $\chi_j = \chi_j' + i\chi_j''$, we get :

$$\begin{aligned} i\omega Y^* &= \frac{1}{L_{reso}} - \frac{L_c^2}{L_{reso}^2}\frac{\chi_j' + i\chi_j''}{1 - L_l\chi_j' - iL_l\chi_j''} + i\omega G_{reso} \\ &= \frac{1}{L_{reso}} - \frac{L_c^2}{L_{reso}^2}\frac{\chi_j'(1 - L_l\chi_j') - L_l(\chi_j'')^2 + i\chi_j''}{(1 - L_l\chi_j')^2 + (L_l\chi_j'')^2} + i\omega G_{reso} \\ &\approx \frac{1}{L_{reso}} - \frac{L_c^2}{L_{reso}^2}\frac{\chi_j'}{1 - L_l\chi_j'} - i\frac{L_c^2}{L_{reso}^2}\frac{\chi_j''}{(1 - L_l\chi_j')^2} + i\omega G_{reso} \end{aligned} \tag{2.18}$$

where the approximation is made because we only considered the experimentally relevant limit, $L_l\chi_j''| \ll |L_l\chi_j'| < 1$. In equation (2.18), the real part represent the the inductance L^* and the imaginary part the conductance G^* of the equivalent circuit, yielding :

$$\frac{1}{L^*} = \frac{1}{L_{reso}} - \kappa \frac{\chi_j'(\Phi)}{1 - L_l \chi_j'(\Phi)} = \frac{1}{L_{reso}} - \frac{\kappa}{L_{ring}}(\Phi) \tag{2.19}$$

$$G^* = G_{reso} - \kappa \frac{\chi_j''(\Phi)}{(1 - L_l \chi_j'(\Phi))^2} = G_{reso} - \kappa G_{ring}(\Phi) \tag{2.20}$$

with :

$$\kappa = \frac{L_c^2}{L_{reso}^2} \tag{2.21}$$

the inductive coupling coefficient,

$$L_{ring} = \frac{\chi_j'}{1 - L_l \chi_j'} \tag{2.22}$$

$$G_{ring} = \frac{\chi_j''}{(1 - L_l \chi_j')^2} \tag{2.23}$$

the ring contribution to both the inductance and the conductance of the system. It does not correspond to what we called Z_{ring} since it does not include the coupling between the ring and the resonator, but it is similar in expression to the screening effect defined in equation 2.12 linking the ring's response to the junction's, justifying this name.

(b) Transmission coefficient and quantities measured

We consider now the whole measuring circuit, shown in figure 2.5(b) and first derive the expression of the transmission coefficient $\Gamma(\omega)$ defined in equation 2.25.

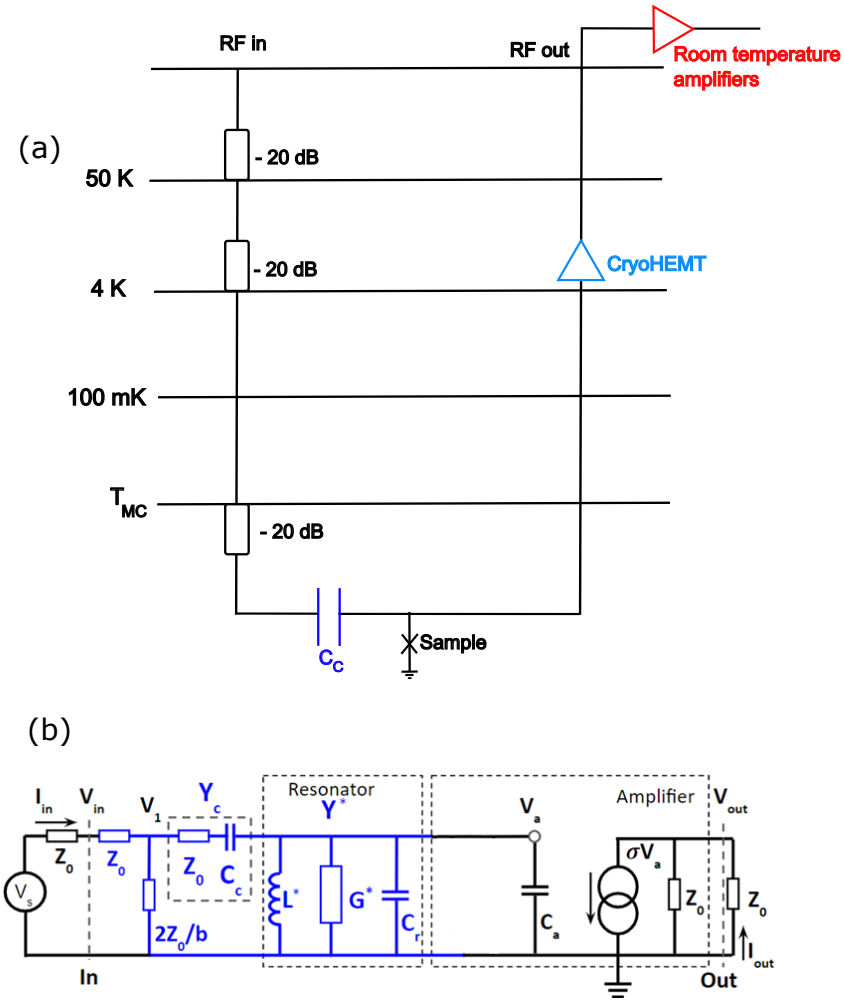

FIGURE 2.5 – (a) Sketch of the wiring in the dilution refrigerator. On the 50K, 4K and the mixing chamber stage of the refrigerator we put three attenuators. The sample (SNS ring and resonator) is coupled to the RF lines via the two coupling capacitances highlighted in pink. The CryoHEMT (blue) is placed in the 4K stage of the dilution refrigerator, and outside the refrigerator the three cascaded amplifiers are sketched in red. (b) Circuit model of the measurement setup, from the RF source to the CryoHEMT amplifier and the measured voltage. The blue part represents the sample, thermally anchored to the mixing chamber whose temperature is withing the experiment going from tens to hundreds of mK. The attenuators are modeled as a T-shaped resistor network with b the attenuation factor.

The left part of the sketch is the RF source. The blue part is thermally anchored to the mixing chamber. The cryogenic amplifier described in the first part of this chapter in on the 4K stage of the dilution refrigerator. There are three attenuators along the transmission line from the input, and they are described by the T-shaped resistor network in the drawing with b the attenuation factor and $Z_0 = 50\ \Omega$. The coupling between the RF generator and the resonator is described by its admittance Y_c. It reads :

$$
\begin{aligned}
Y_c &= \frac{1}{Z_0 + 1/(j\omega C_c)} \\
&= \frac{\omega^2 C_c^2 Z_0}{1+\omega^2 C_c^2 Z_0^2} + j\omega \frac{C_c}{1+\omega^2 C_c^2 Z_0^2} \\
&\approx G_c + j\omega C_c
\end{aligned}
\tag{2.24}
$$

The total conductance $G_{tot} = G^* + G_c$ with $G_c = \omega_r^2 C_c^2 Z_0$ and $C_c = 1.2$ pF, is due to the coupling between the generator and the resonator. It adds a very small effective conductance G_c in parallel to the resonator, preserving its quality factor. The transmission coefficient is defined by :

$$
\Gamma = \left. \frac{V_{out}}{V_{in}} \right|_{Z_{out}=Z_0}
\tag{2.25}
$$

where $V_{out,in}$ are defined in Fig. 2.5. Defining $Y_{reso} = G_{reso}//L_{reso}//C_{reso}$, Γ reads :

$$
\begin{aligned}
\Gamma &= \frac{I_{out} Z_0}{V_{in}} \\
&= -\frac{\sigma V_a Z_0}{2 V_{in}} \\
&= -\frac{Z_0}{2} \times \frac{V_a}{V_1} \times \frac{V_1}{V_{in}} \\
&\approx \frac{\sigma Z_0}{2} \frac{2}{b} \times \frac{Y_c}{Y_c + Y_{reso}} \\
&\approx -\frac{\sigma Z_0}{b} \times \frac{G_c + j\omega C_c}{G_{tot} + i[\omega C_{tot} - \frac{1}{\omega L^*}]} \\
&\approx -\frac{(\sigma Z_0/b)[i\omega C_c/(G_{tot})]}{1 + i\frac{1}{G_{tot}}\sqrt{\frac{C_{tot}}{L^*}}(\frac{\omega}{\omega_r} - \frac{\omega_r}{\omega})}
\end{aligned}
\tag{2.26}
$$

This derivation yields the model for the transmission coefficient and the definition of the resonance frequency and quality factor.

$$
|\Gamma| = \frac{\Gamma_r}{\sqrt{[1 + Q^2(\omega/\omega_r - \omega_r/\omega)^2]}}
\tag{2.27}
$$

$$
\omega_r = 1/\sqrt{L^* C_{tot}}
\tag{2.28}
$$

$$
Q = 1/[L^* G_{tot} \omega_r]
\tag{2.29}
$$

It is directly seen that a change in the total inductance will lead to a change in the resonance frequency ω_r. Similarly, the change in the quality factor due to the variation of inductance and conductance can be calculated.

$$\frac{\delta\omega_r}{\omega_r} = -\frac{\delta L^*}{2L^*} \approx \frac{L_{reso}}{2}\delta(\frac{1}{L^*}) \tag{2.30}$$

$$\delta(\frac{1}{Q}) = \frac{\delta\omega_r}{2Q\omega_r} + L^*\omega_r\delta G_{tot} \approx L_{reso}\omega_r\delta G_{tot} \tag{2.31}$$

The approximation is made because experimentally relevant. As we will show later, $L^*\omega_r\delta G_{tot}$ is two orders of magnitude higher than $\delta\omega_r/2Q\omega_r$. We have seen that these changes are coming from the ring, and we finally arrive at the expression of L_{ring} and G_{ring} with respect to the physical quantities measured $\delta\omega_r$ and $\delta(1/Q)$

$$\delta(\frac{\kappa}{L_{ring}}) = \frac{2}{L_{reso}}\frac{\delta\omega_r}{\omega_r} \tag{2.32}$$

$$\delta(\kappa G_{ring}) = \frac{1}{\omega_r L_{reso}}\delta(\frac{1}{Q}) \tag{2.33}$$

(c) Current fluctuations of the circuit

Let us noW derive the expression for the noise of the circuit. We consider the very same circuit shown in Fig. 2.5 but this time the input is shorted by a 50Ω resistance Z_0. The main noise sources of the system are the following :

- The SNS junction generates the supercurrent noise we want to measure. We denote it $S_{I,j}$.
- Due to its finite conductance, the resonator is also a noise source and it obeys the fluctuation-dissipation theorem [36]. In terms of current noise, we write this contribution $4k_BTG_{reso}$.
- The amplifier contributes to the total noise of the system. The internal current and voltage noise $S_{I,a}$ and $S_{V,a}$ are considered decorrelated. Their contribution to the total current noise is denoted $S_{I,amp}$.

The simplified circuit is represented in Fig. 2.6 where the thermal contribution to the noise is noted $S_{I,th}$ and the amplifier's contribution $S_{I,amp}$.

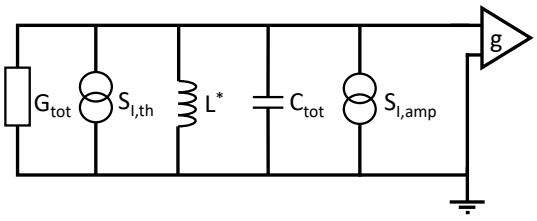

FIGURE 2.6 – Simplified circuit model considering the noise, with g the total gain including the room temperature amplifiers.

Similarly to what has been done for the transmission measurement, we can decompose the total thermal current noise coming from the ring coupled to the

resonator by :

$$S_{I,th} = 4k_B T G_{reso} + \kappa S_{I,ring} \tag{2.34}$$

with

$$S_{I,ring} = \frac{S_{I,j}}{(1 - L_l/L_j)^2} \tag{2.35}$$

The amplifier contribution to the current noise is obtained by adding the two internal noise contributions. To do so, we transform the internal voltage noise into an effective current noise.

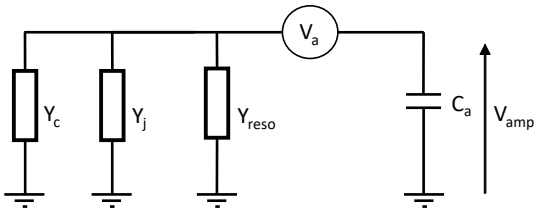

FIGURE 2.7 – Circuit model to convert the internal voltage noise of the amplifier into a current noise.

Fig. 2.7 shows the circuit model considered for the conversion. We have a voltage source V_a and we want to derive the expression of the measured V_{amp} across the capacitance. This circuit is equivalent to a voltage divider, and we can write V_{amp} as

$$\begin{aligned} V_{amp} &= \frac{(i\omega C_a)^{-1}}{(i\omega C_a)^{-1} + \frac{1}{Y_{reso}+Y_j+Y_c}} \times V_a \\ &= \frac{Y_c + Y^*}{Y_c + Y^* + i\omega C_a} \times V_a \end{aligned} \tag{2.36}$$

because $Y_c + Y^* + i\omega C_a$ represents the total admittance of the system, we finally get :

$$I_{amp} = (Y_c + Y^*) \times V_a \tag{2.37}$$

and finally, since the current (resp. voltage) noise can be written as $S_i = \langle I^2 \rangle$ (resp. $S_v = \langle V^2 \rangle$) and we can add the two sources independently, we get

$$S_{I,amp} = S_{I,a} + S_{V,a} \times |Y_c + Y^*|^2 \tag{2.38}$$

What we measure is in fact the total voltage noise spectrum $S_v(f)$,

$$S_v(f) = S_{V,th}(f) + S_{V,amp}(f) \tag{2.39}$$

and the conversion to current noise is $S_I(f) = S_v(f) \times |Y^* + Y_c + i\omega C_a|^2$. The dependence of $S_{I,amp}$ on Y^* yields a significant phase-dependence of this term in the noise. Thus, a precise calibration of all the terms involved in $S_{I,amp}$ and the further separation of this term to obtain $S_{I,th}$ is needed. Those are the key challenges of the experiment.

2.3 . Calibration procedure

The quantitative knowledge of the circuit elements shown in Fig. 2.5 is important to extract quantitatively and further analyse the supercurrent noise and compare it to the dissipation measurement. Several parameters have to be taken into account :

— The exact temperature to be considered, detailed in the first part of this section.

— The calibration of the circuit elements is the subject of the second part.

— The transmission measurement and the precise extraction of $\delta\omega_r(\Phi)$ and $\delta(1/Q)(\Phi)$.

2.3.1 . Electronic temperature

At cryogenic temperature, the thermalization of the electrons is difficult due to weak electron-phonon coupling [37]. The best way to calibrate the exact electronic temperature is by measuring the $S_V - T$ relation. To do so, we measured the noise close to the resonance and assumed at high temperature $S_V(T) \approx 4k_BT/G_{reso} + constant$. The temperature dependent part yields the exact electronic temperature, whereas the constant part includes the noise coming from the amplifier.

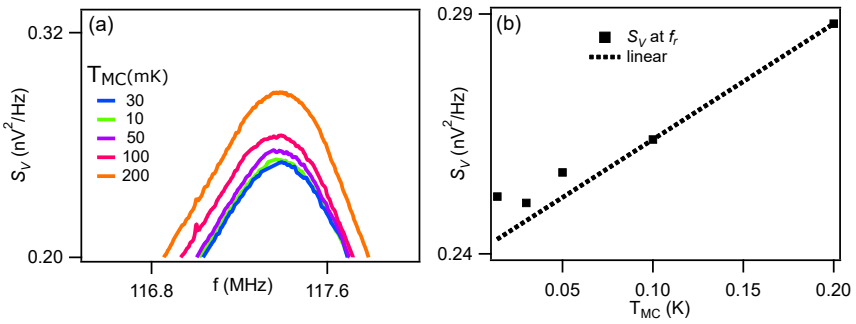

FIGURE 2.8 – Calibration of the electronic temperature. **(a)** $S_v(f)$ as measured close to the resonance. The displayed temperatures are the temperature of the mixing chamber. **(b)** Relation between the voltage noise on resonance $S_V(f_r)$ and T, and the fitted linear relation.

Fig. 2.8 shows the measured voltage noise without any applied field. By taking the value of the noise on resonance, the linear extrapolation $S_V = a \times T + b$ is performed on the two high T (above $T_{MC} = 100$ mK) where we assume the correspondance between the mixing chamber temperature and the electronic temperature ($T_{MC} = T$). The fit yields $a = 2.2 \times 10^{-19}$ V^{2}Hz^{-1}K^{-1} and $b = 2.4 \times 10^{-19}$ V^{2}Hz^{-1}. At lower temperatures, where the data points deviates from the linear relation the electronic temperatures are determined by inverting the $S_V - T$ relation : $T = [S_V(T_{MC}) - b]/a$. The summarized conversion between mixing chamber temperatures and electronic temperature is listed in Tab. 2.2.

$G_{reso}(T, \Phi = 0)$ can also be extracted from a : $G_{reso} = 4k_B/a$. The obtained values are summarized in table 2.3 and will be discussed in section 2.3.2.

We acknowledge the lack of points for the linear fit in temperature. Fortunately it seems to be sufficient for the purpose of this experiment as will be seen in section

T_{MC}(mK)	T (mK)
10	50
30	45
50	60
100	100
200	200

TABLE 2.2 – Mixing chamber and electronic temperatures.

2.4.2. It is nevertheless a point to take care of for further experiments of this kind. The second point that can be disturbing is the non-monotonic change from T_{MC} to T, as for instance $T_{MC} = 10$ mK is in fact hotter that $T_{MC} = 30$ mK. Very short powercuts occured during the experiments that could have affected the specification of the dilution refrigerator. This doesnt' affect the further presented experimental results as the experiments performed at one temperature didn't suffer from any perturbation of this kind as they were done on the minimum of time required and any possible drift in that time is taken into account. The precise calibration of the circuit elements presented in the next part is also done independently for every temperature.

2.3.2 . Calibration of circuit elements

The quantitative comparison between the supercurrent noise and the ac admittance of the ring needs precise calibration of all circuit elements. Still at phase $\varphi = 0$, this is done by measuring $\Gamma(\omega)$ and $S_V(\omega)$. For calibration the ring contribution is neglected since the inductive coupling coefficient $\kappa = L_c^2/L_{reso}^2$ is small and won't affect the calibrated parameters.

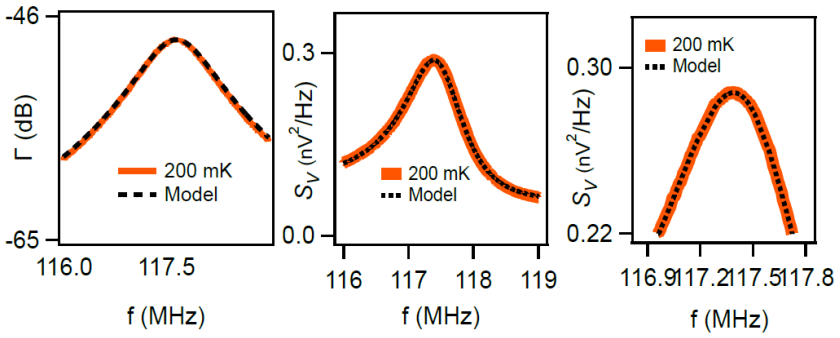

FIGURE 2.9 – Calibration of circuit elements at T = 200mK using the models for **(a)** $\Gamma(f)$ with eq. 2.27 and **(b)** $S_v(f)$ with eq. 2.39. **(c)** Zoomed-in plot of (b) closer to the resonance.

We explain the calibration process for one temperature only (T = 200 mK), but the process is the same for all the temperatures, yielding a few difference in certain parameters, all detailed below. As for the electronic temperature measurement, the calibration is done at zero magnetic field and we assume $\Phi = 0$.

— By measuring $\Gamma(f)$ as shown in Fig. 2.9(a) (solid lines) and fitting it to eq. 2.27, we obtain $Q = 105$ and $f_r = 117.5$ MHz.
— G_{reso} is directly obtained from the $S_V - T$ relation. At 200mK, $G_{reso} = 246.5$ μS.
— Since $Q = 1/L^* G_{tot} \omega_r$, we get $C_{tot} = 35$pF and $L_{reso} = 52.5$nH. This value of inductance is consistent with the resonator design, for which we expected 40nH for the calculated geometric and kinetic inductances 2.13. The obtained C_{tot} is assumed constant with temperature.

The amplifier parameters $S_{I,a}$, $S_{V,a}$, C_a are obtained via a fit of the total voltage noise spectrum $S_V(f)$ to equation 2.39, assuming $S_{I,th} = 4k_B T G_{reso}$ (only at phase 0) and fixing C_{tot} as 35 pF. This assumption is made because we don't expect the total capacitance to be affected too much by temperature or field. The result is displayed in Fig. 2.9(b) and Fig. 2.9(c) is a closer look on the spectrum on resonance. Our model fits the entire spectrum and not only the resonant part, which is important in the understanding of the measured fluctuations : for instance the asymmetry observed in 2.9 far from the resonance is due to the finite C_a and $S_{v,a}$. Those quantities could not be obtained if we took into consideration only the resonance.
Small drifts can occur due to temperature or time since the measurements can be long (two days at least for 20 points in phase at a given temperature). To compensate these phenomena we re-calibrate at zero field for each temperature. The calibrated values for the circuit elements obtained via this method are listed in Table 2.3 and they will be the ones used in the quantitative analysis coming in further sections.

T (mK)	200	100	60	50	45
G_{reso} (µS)	246.5	245.5	235.8	236.3	237.7
$1/L_{reso}$ (µH^{-1})	19.1	19.1	19.0	19.0	19.0
C_a (pF)	0.21	0.21	0.14	0.14	0.14
$\sqrt{S_{I,a}}$ (fA/$\sqrt{\text{Hz}}$)	93.5	94.7	96.6	95.2	96.8
$\sqrt{S_{V,a}}$ (nV/$\sqrt{\text{Hz}}$)	0.26	0.25	0.25	0.25	0.24

TABLE 2.3 – Summary of the calibrated circuit parameters

The fact that G_{reso} decreases as temperature decreases as expected (the lower the temperature, the lower the losses) indicates that our method is reliable.

2.3.3 . Calibration of transmission measurement

As stated in section 2.2.3, the physical quantities measured are the resonance frequency shift and inverse quality factor shift. In this section, we detail how we obtain these quantities and how we calibrate this measurement to quantitatively compare it to the noise measurement. We want to measure variations of δf with a precision of $\delta f/f < 10^{-6}$. To achieve this accuracy we use a frequency modulation technique. The setup diagram for measuring δf and $\delta(1/Q)$ is shown in Fig. 2.10.

The generator produces an FM-modulated signal whose center frequency ω_n is close to the resonance of the resonator, and its modulation depth is noted ω_m. The

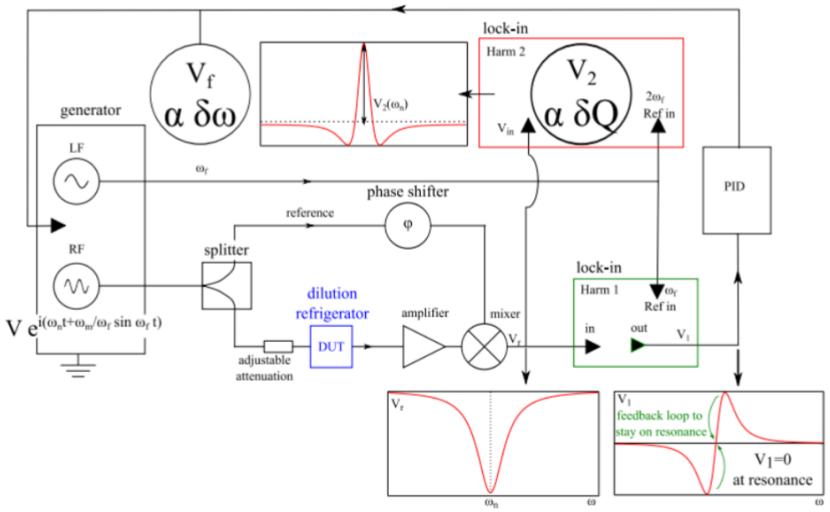

FIGURE 2.10 – Setup diagram for measuring δf and $\delta(1/Q)$. The figure is reproduced from [24] as the measurement process is similar.

modulation frequency ω_f is around 1 kHz to avoid 1/f noise. The instantaneous frequency reads $\omega(t) = \omega_n + \omega_m \cos(\omega_f t)$. The signal is sent to the resonator in the dilution refrigerator (DUT in Fig. 2.10) and the transmitted amplified signal is demodulated using the same signal split from the generator output.
Thus, the ouput of the mixer V_r is a low-frequency signal oscillating at the modulation frequency ω_f. This signal is then sent to two lockin-in amplifiers detecting at ω_f and $2\omega_f$ (respectively green and red in the figure).

- The ouput V_1 is a dc signal proportional to $\frac{\partial Re(\Gamma)}{\partial \omega}$, which is 0 on resonance. V_1 is sent to a PID module feeding back to the local oscillator of the signal generator. When the magnetic flux is sweeped, the feedback loop is closed and the local oscillator adjusts the center rf frequency ω_n such that V_1 is always 0, and outputs the resonance frequency shift with respect to the flux.
- Due to the feedback loop, the resonator stays on resonance during the sweep and the second lockin output has a variation $\delta V_2(\phi)$ on top of a large background $V_2(0)$ with respect to the flux.

This last quantity is related to $1/Q$ and thus to G_{ring}. On resonance, it can be shown [29] that the relation between $\delta(1/Q)$ and V_2 reads :

$$\delta(\frac{1}{Q}) = -\frac{1}{\alpha Q(0)} \frac{\delta V_2}{V_2(0)} \tag{2.40}$$

$Q(0) = 105$ is determined from the fit of $\Gamma(f)$ in section 2.3.2. The coefficient α needs to be determined in our experiment. When $\omega_m \ll \omega_r/Q$, one can show that $\alpha = 3$ [29]. However in our experiment ω_m is chosen around ω_r/Q to improve the signal-to-noise ratio of V_2. To determine α we start by measuring $V_2(f)$ and comparing with the numerical calculation. The numerical calculation uses the analytical expression of $Re(\Gamma)$ detailed in equation 2.27 and $\omega(t) = \omega_n + \omega_m \cos(\omega_f t)$ we obtain the calculated V_2 by taking the second Fourier component of $Re(\Gamma)$.

Fig. 2.11 shows a remarkable agreement between the model and the experimental data. This measurement setup then allows us to detect a very small variation of both the inverse inductance of the order of 1 nH^{-1} and in conductance of the order of 1 μS.

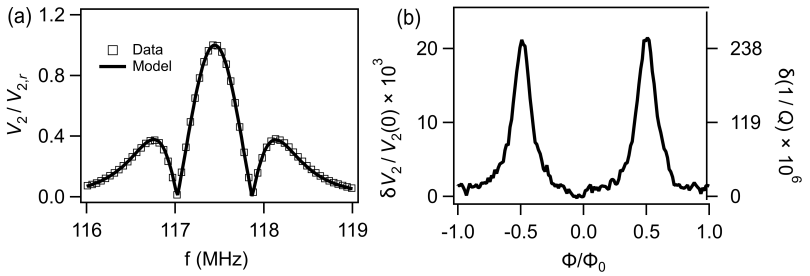

FIGURE 2.11 – Example of the calibration at T = 50 mK.**(a)** Normalized second harmonic V_2 of $Re(\Gamma)$ with respect to f (squares) and model obtained from numerical calculations (solid lines). **(b)** Directly measured δV_2 normalized by $V_2(0)$ (left axis) and the obtained $\delta(1/Q)$ using the calibrated α.

2.4 . Fluctuation and dissipation measurement : the SNS ring

The experimental results for both the transmission and noise are presented in this part. The first section describes the measurement of the inductance and conductance, to be compared with a DC control sample. The second section describes the noise measurement, along with the data processing and extraction of the supercurrent noise coming from the ring. Finally, we compare both experiments to check the fluctuation-dissipation for a NS ring.

2.4.1 . Inductance and conductance of the NS ring

(a) Inductances and current-phase relation

We explained in section 2.2.3 that the variations of inductance and conductance of the ring are linked to the shifts of resonance frequency and quality factor derived in equation 2.32 and (2.33). We start with the variations of the inductance of the ring. By equation 2.32 we get the results shown in Fig. 2.12.

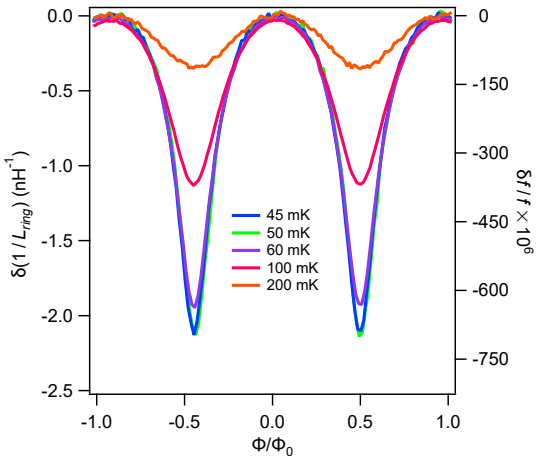

FIGURE 2.12 – Phase variation of the ring's inductance with respect to the flux, directly obtained from the measurement of the frequency shift using equation 2.32. On the right axis the directly measured $\delta f/f$ as a guide to the equivalence between $\delta f/f$ and $\delta(1/L_{ring})$.

The experimental result shown in Fig. 2.12 is the relative variation of the ring's inductance. It can be written more explicitely :

$$\delta(\frac{1}{L_{ring}}) = \frac{1}{L_{ring}}(\Phi) - \frac{1}{L_{off}} \tag{2.41}$$

in which L_{off} is the reference value of inductance of the ring, taken at $\Phi = 0$ in our experiment. In order to obtain the absolute $1/L_{ring}$, we need to determine L_{off}. This is done by first considering that we are working at relatively low frequency hence the adiabatic regime seems to be the regime to consider at least for the reactive contribution. In this case, by neglecting the screening effect, the inverse inductance can be written :

$$\frac{1}{L_{ring}} = \frac{\partial I_s}{\partial \Phi} \tag{2.42}$$

With I_s the current-phase relation. The offset in equation 2.41 adds a linear background in the CPR. To obtain the absolute L_{ring} we follow this recipe :

1. We start by integrating the obtained $\delta(1/L_{ring})$ as if we assumed L_{off} to be 0.
2. This yields a "tilted" CPR shown in Fig. 2.13(a). The linear background is plotted as a guide to the eye and the slope corresponds to L_{off}.
3. This L_{off} is added to the $\delta(\frac{1}{L_{ring}})$ of Fig. 2.12 to obtain the absolute L_{ring}.
4. This process is repeated using the corrected $1/L_{ring}$ until $I_s(\Phi)$ has no more linear background and is periodic in Φ_0, which is the only allowed form of the CPR (shown in Fig. 2.13(b)).

The result of this procedure is shown in Fig. 2.14

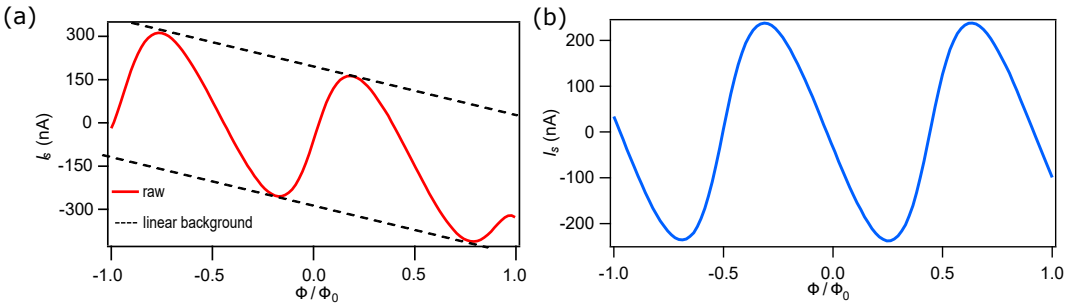

FIGURE 2.13 – Removing the offset in $1/L_{ring}$ can be done by integrating the CPR. (a) When directly integrated, the CPR (red, solid) has a tilted shape, the black dashed lines highlight the linear background to be removed. (b) When this linear background is removed, the CPR is periodic in Φ_0 : the offset has been determined.

Removing this linear background in the CPR would yield the current-phase relation as shown in Fig. 2.13(b). But in our case, the screening effects has a non-negligible impact and we can't assume $L_{ring} = L_j$ for the following. Taking into account this effect and with the absolute L_{ring} yields :

$$\frac{1}{L_j}(\Phi) = \frac{1/L_{ring}(\Phi)}{1 + L_l/L_{ring}(\Phi)} \tag{2.43}$$

with $L_l = 250$ pH dominated by L_C (measured) and $L_l - L_c$ thus estimated. In Fig. 2.15 we provide a comparison between L_j and L_{ring} for all the temperatures.

The difference between the inductance of the ring L_{ring} and the inductance of the junction L_j decreases with temperature. Indeed, the screening is characterized by :

$$\beta = L_l/L_j = \frac{2\pi L_l I_c(T)}{\Phi_0} \tag{2.44}$$

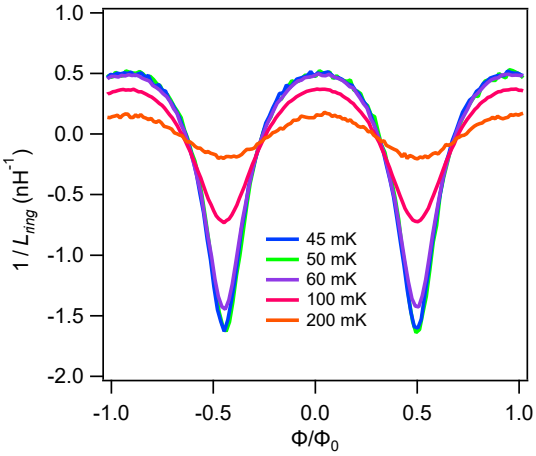

FIGURE 2.14 – Absolute L_{ring} obtained after adding the obtained L_{off} following the process described above.

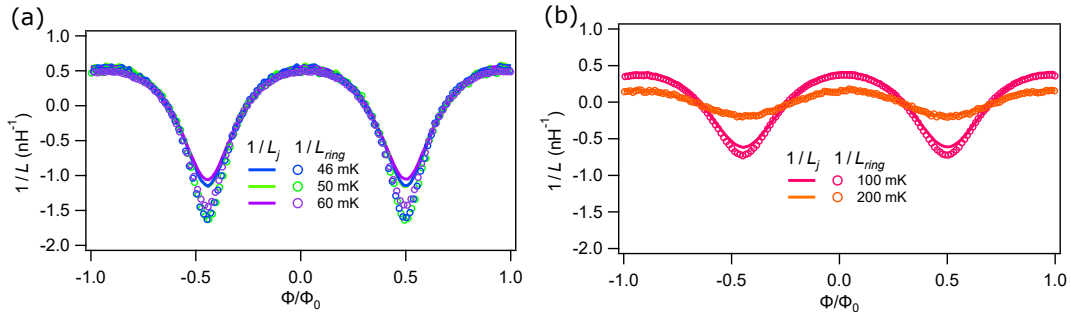

FIGURE 2.15 – Comparison between L_{ring}^{-1} (circles) and L_j^{-1} (solid) when the screening contribution is taken into account (a) at T = 45, 50 and 60 mK. (b) at T = 100, 200 mK.

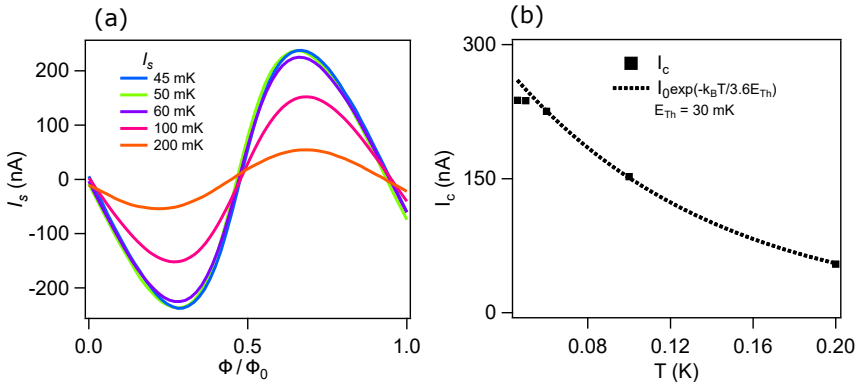

FIGURE 2.16 – **(a)** CPR obtained via numerical integration of $1/L_j$ at all temperature. **(b)** Temperature evolution of the critical current directly read from the CPR.

and I_c decreases exponentially with temperature. This is further seen by integration of $1/L_j(\Phi)$: The shape of the CPR is reminiscent of the long diffusive junction, similar to a distorted sine and becoming more and more sinusoidal with increasing

temperature (2.16(a)). By taking the maximal value of the CPR at every temperature, we build the $I_c(T)$ shown in Fig. 2.16(b) and fit it to :

$$I_c(T) \propto \exp(-k_B T/3.6E_{Th}) \tag{2.45}$$

which is the behaviour expected for a diffusive long SNS junction when the temperature is higher than E_{Th} [19]. We thus obtain the Thouless energy of the system, $E_{Th} = 30$ mK, in good agreement with previous experiments on a similar system [29], and with a control DC sample detailed later.

Finally, the total inductance of the system L^* can be obtained by adding the calibrated L_{reso} and by equation 2.19 we obtain the inductance of the total system vs. the phase plotted in Fig. 2.17.

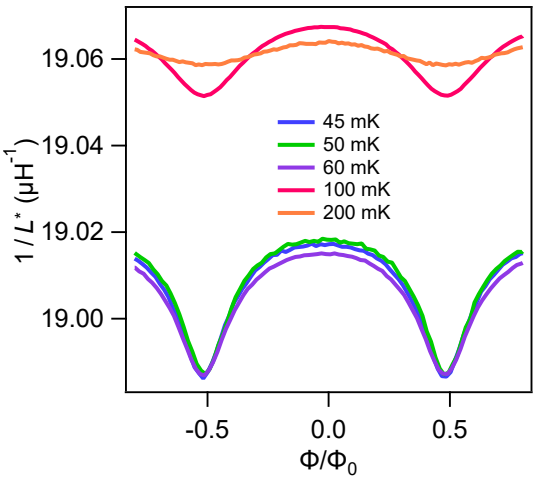

FIGURE 2.17 – Total inductance of the system using the directly measured $1/L_{ring}$ and the obtained L_{off} from the process described above. The resonator's inductance L_{reso} is added to finally obtain the phase-dependence of the whole circuit's inductance.

(b) Conductance

Similarly we can obtain the variation of conductance of the ring only with equation 2.33, shown in Fig. 2.18. Once again there is a offset to be taken into account to obtain the absolute G_{ring}, along with the screening effect on the measured conductance. This time, the absolute G_{ring} reads :

$$G_{ring} = \frac{G_j}{(1 - L_l/L_j)^2} \tag{2.46}$$

with L_j obtained in the previous section. To obtain this offset, we follow the process proposed in [29]. We first calculate the ratio :

$$r = \frac{|\delta G_{ring}|}{|\delta(1/L_{ring})|} \tag{2.47}$$

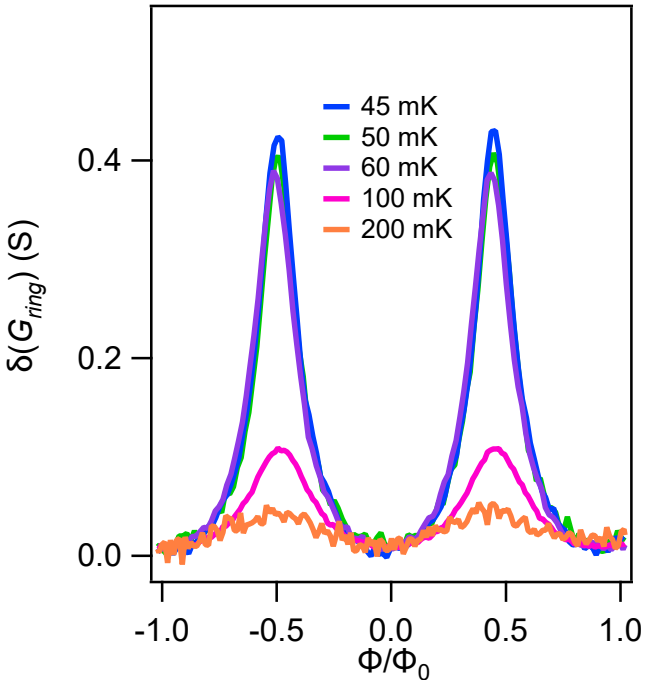

FIGURE 2.18 – δG_{ring} obtained after the directly measured $\delta(1/Q)$, following equation 2.33.

where δ refers to the amplitude of variation over phase of the considered quantity and is read directly from the measurement in Fig. 2.12 and 2.18. It correspond in our case to the difference between $\Phi = 0$ and $\Phi = 0.5\Phi_0$. For the expressions of L_{ring} and β, we write :

$$\begin{aligned}\left|\delta\left(\frac{1}{L_{ring}}\right)\right| &= \frac{1}{L_{ring}}(0) - \frac{1}{L_{ring}}(0.5\Phi_0) \\ &= \frac{\chi_j'(0.5\Phi_0)}{1-\beta(0.5\Phi_0)} - \frac{\chi_j'(0)}{1-\beta(0)} \\ &= \frac{1}{L_l}\frac{\beta(0.5\Phi_0)-\beta(0)}{[1-\beta(0.5\Phi_0)]\,[1-\beta(0)]}\end{aligned} \tag{2.48}$$

For the conductance, we assume the same values of G_j at phase 0 and π, yielding $G_j(0.5\Phi_0) = G_j(0) = G_0$. This assumption approximates the junction to be very weakly phase-dependent, and it will be proven true in a later section (see section

2.5) Therefore the difference $|\delta G_{ring}|$ is written :

$$\begin{aligned}
|\delta G_{ring}| &= \frac{G_0}{[1-\beta(0.5\Phi_0)]^2} - \frac{G_0}{[1-\beta(0)]^2} \\
&= G_0 \frac{[\beta(0.5\Phi_0)-\beta(0)][2-\beta(0.5\Phi_0)-\beta(0)]}{[1-\beta(0.5\Phi_0)]^2\,[1-\beta(0)]^2} \\
&= G_0 \frac{\beta(0.5\Phi_0)-\beta(0)}{[1-\beta(0.5\Phi_0)]\,[1-\beta(0)]} \\
&\times \left[\frac{1}{1-\beta(0)} + \frac{1}{1-\beta(0.5\Phi_0)}\right]
\end{aligned} \tag{2.49}$$

Combining equations (2.48) and (2.49) we arrive at :

$$r = L_l G_0 \left[\frac{1}{1-\beta(0)} + \frac{1}{1-\beta(0.5\Phi_0)}\right] \tag{2.50}$$

with $\beta(0, 0.5\Phi_0)$ and r respectively read and calculated from the measurement. The obtained G_0 is used to buid the screening contribution of the measured conductance :

$$G_s(\Phi) = \frac{G_0}{(1-\beta(\Phi))^2} \tag{2.51}$$

and it can be plotted : The offset is obtained by equating $G_{ring}(0)$ and $G_s(0)$.

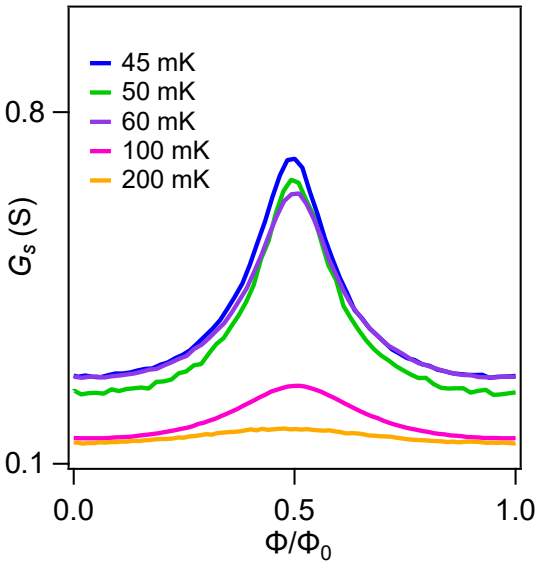

FIGURE 2.19 – Phase-dependent screening contribution to the measured conductance using equation 2.51. The phase-dependence of this conductance doesn't come from the conductance directly but from the inductance via the screening term $\beta(\Phi)$.

Using this method we obtain the absolute G_{ring} and the contribution to G_{ring} of the screening term. In Fig. 2.20 we plot the obtained G_{ring} and provide a direct comparison with G_s.

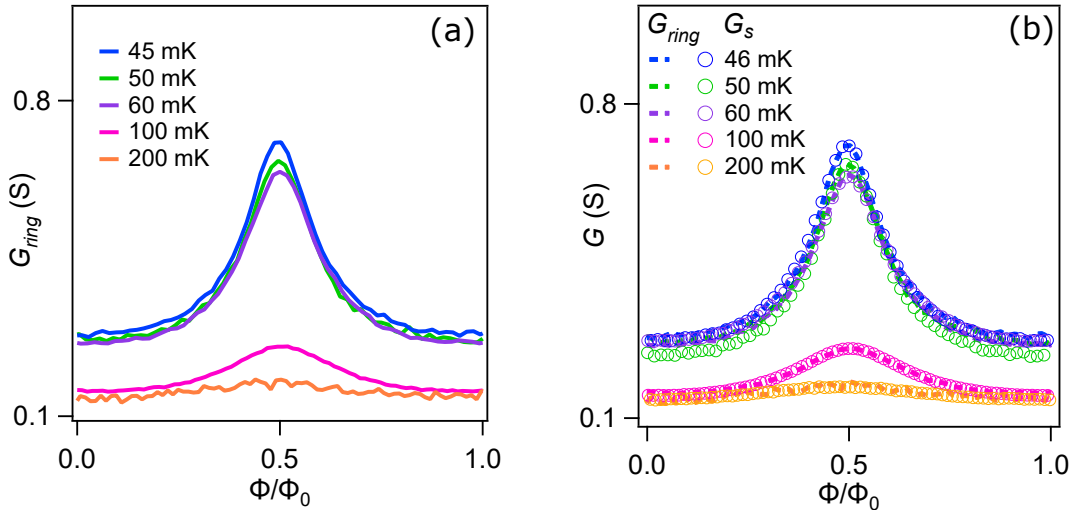

FIGURE 2.20 – **(a)** Absolute G_{ring} with considered offset, obtained by equation $G_s(0)$ and $G_{ring}(0)$. **(b)** Comparison between the absolute G_{ring} and the screening contribution G_s. We see that almost all the phase dependence of the conductance is due to screening.

It can be seen from Fig. 2.20(b) that the screening contribution provides most of the phase-depence of the conductance. Finally, now that the offset and the screening term has been obtained, we can obtain the junction's conductance alone by inverting equation 2.46, plotted in Fig. 2.21.

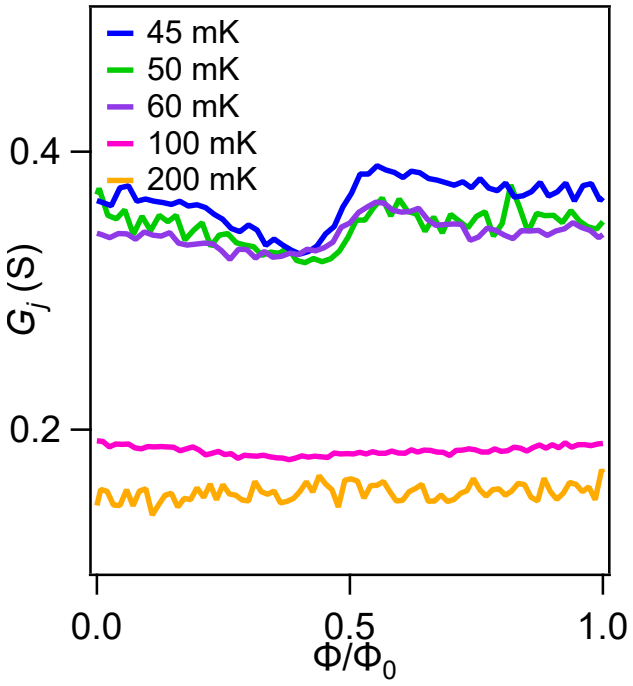

FIGURE 2.21 – Conductance of the junction alone : it is almost phase-independent (especially at high temperature), but also very strongly temperature dependent.

The weak phase-dependence of the junction will be discussed in the last section of this chapter. The other striking feature of the conductance is its strong temperature dependence. By taking the mean-value of G_j (which can be approximated by the value at $\Phi = 0.5\Phi_0$), we can plot $G_j(T)$ and fit it to the expression ([38, 39, 29]):

$$G_j(T) = G_N(1 + \frac{T^*}{T}) \tag{2.52}$$

whose result is shown in Fig. 2.22. The strong temperature dependance is a key difference between the SNS junction and the normal metal that seems surprising as the usual representation of the conductance, the Drude conductance, is temperature independent.

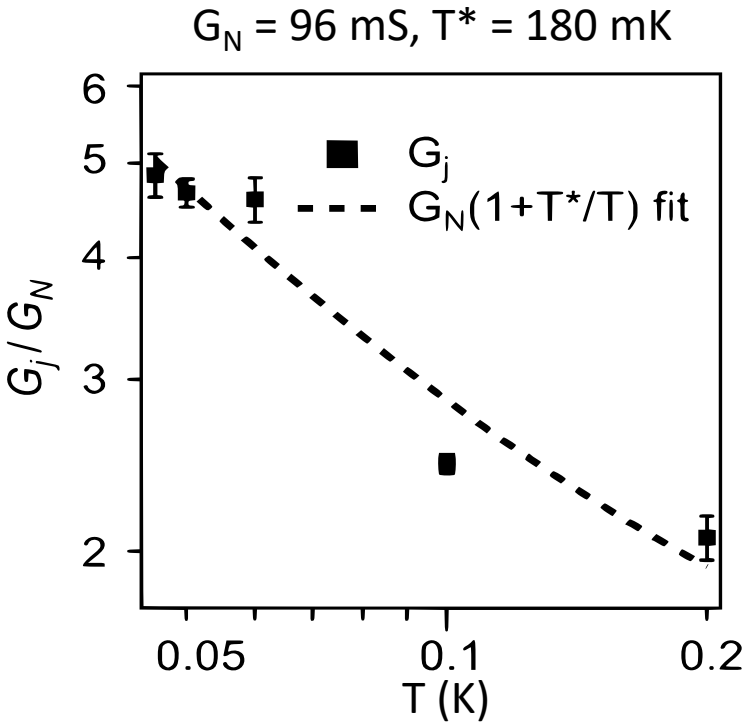

FIGURE 2.22 – G_j vs T with both axes in logarithmic scale.

The fit yields $G_N = 96$ mS and $T* = 180$ mK, that is six times the Thouless energy obtained from the fit in Fig. 2.16(b). On top of the strong temperature dependence, we note the enhanced conductance compared to G_N, with G_j going from $2 \times G_N$ at 200 mK up to $5 \times G_N$ at very low temperature. We discuss and provide an explanation of these results in section 2.5.

Finally, by adding the calibrated conductances of all the circuit elements we consider, we can plot the overall conductance of the system G_{tot} shown in Fig. 2.23.

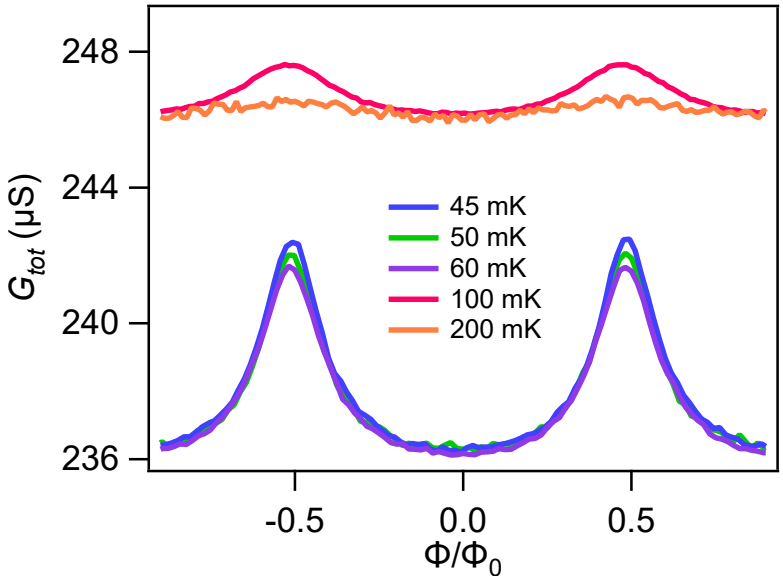

FIGURE 2.23 – Conductance of the whole circuit. The phase-dependent part is due to the ring, whereas the background comes from the calibrated circuit elements. The huge difference in order of magnitude compare to the results presented in Fig. 2.18 is due to the coupling factor $\kappa \approx 10^{-5}$.

(c) Comparison with a gold-based SNS control sample.

To further validate the experiment, we fabricated a gold-based SNS junction using a process similar to the one presented in section 2.2. The measurement performed in the DC limit yields the differential resistance curve presented in Fig. 2.24.

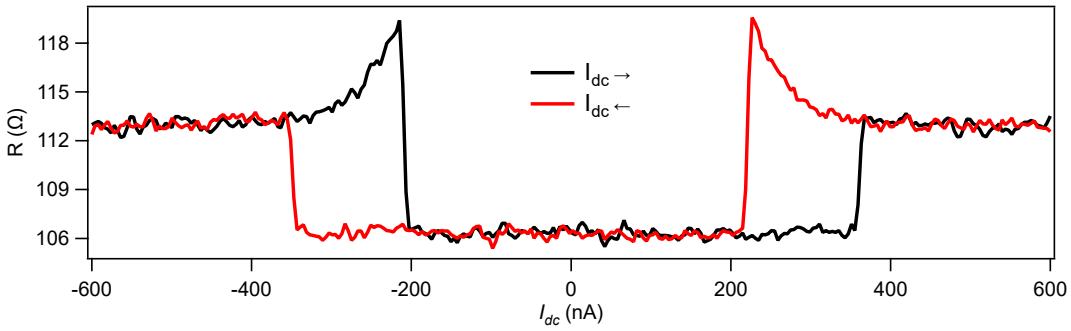

FIGURE 2.24 – Two wires differential resistance measurement of the control sample. The sweep in both direction of the current highlights the hysteretic behaviour. The jump between the low bias and the high bias region yields the normal state resistance $R_N = 7\ \Omega$, hence $G_N = 143$ mS. The retrapping current is $I_{rt} = 200$ nA and the switching current is $I_{sw} = 360$ nA. This yields a product $eR_N I_c \approx 48$ mK $\ll \Delta$.

The transition from the supercurrent state to the normal state occurs at a value of switching current of $I_{sw} = 360$ nA whereas the retrapping current $I_{rt} = 200\ nA$, comparable in order of magnitude to measured critical current of the NS ring at low temperature shown in Fig. 2.16. The jump of resistance between the low bias

and high bias region yields $R_{N,dc} = 7\ \Omega$, hence $G_{N,dc} = 143$ mS. There is a factor of roughly 1.5 between the RF (obtained from the fit) and the DC measurement. This could be explained by the different aspect ratios and/or mean-free paths of the two gold wires, as it can be seen from the product $eR_N I_C$ giving 24 mK for the RF sample and 45 mK for the RF sample. These comparable values confirm the results of this measument.

2.4.2 . Noise and validation of the FDT

(a) Extraction of the supercurrent thermal noise

In this part, we present the results on the noise measurement and the extraction of the quantities of interest. A comparison between the measured conductance of both the whole circuit and the ring is also given, leading to the validation of the fluctuation-dissipation theorem for a superconducting system.
The noise is measured by putting a 50 Ω resistance at the input of the circuit presenting on Fig. 2.5, during the same cooldown as the one for the transmission measurement. The voltage spectrum V_n is measured by an oscilloscope with the spectrum analysis function that converts the time-domain voltage into the voltage spectrum. This voltage spectrum is then converted into the noise spectrum by

$$S_v(f) = \frac{V_n^2}{g^2 \times RBW} \tag{2.53}$$

where $RBW = 954$ Hz is the resolution bandwidth and g the gain of the measurement setup. Each spectrum is averaged 10^4 times. One spectrum measurement thus takes around 2 hours to complete, and for 20 points in a complete period in Φ_0 a bit more than 40 hours. Indeed the measured noise is the total noise of the circuit. The part of interest is the thermal noise that we need to extract. As it was shown in section 2.2.3 the voltage noise originating from the amplifier is itself frequency and phase-dependent (see Fig. 2.25(a)). Using the calibrated circuit elements of table 2.3, we can reconstruct the term $S_{V,amp}$ and substract it to get only the thermal part, as shown in Fig. 2.25(b)

The extracted $S_{V,th}$ is a very small contribution of the total noise and its phase variation is even smaller (see Fig. 2.26(a)). The corresponding current noise $S_{I,th} = |Y^* + Y_c + i\omega C_a|^2 \times S_{V,th}$ is obtained and plotted around resonance at phase 0 and π in Fig. 2.26(b).

In the limit $k_B T \gg hf$, the noise should be frequency-independent. This is indeed the case in our experiment since $hf = 6$ mK. Therefore we can calculate the mean value and standard error around the resonance frequency to further reduce the data uncertainty using :

$$\begin{aligned} \overline{S_{I,th}} &= \frac{1}{N}\sum_{n=1}^{N} S_{I,th}(f_n) \\ \Delta S_{I,th} &= \sqrt{\frac{\sum_{n=1}^{N}[S_{I,th}(f_n) - \overline{S_{I,th}}]^2}{N(N-1)}} \end{aligned} \tag{2.54}$$

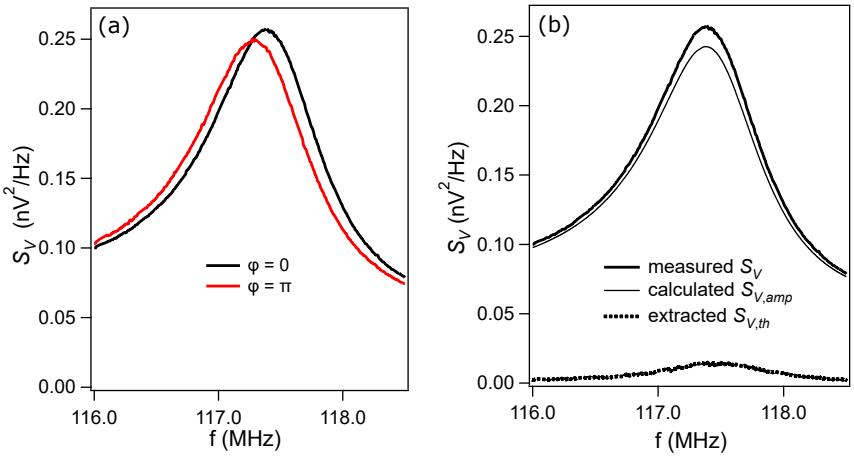

FIGURE 2.25 – **(a)** Example of the total voltage noise spectrum directly measured, at phase 0 and π. **(b)** Illustration of the different contributions at phase 0. The total voltage noise (thick solid line) is the sum of the effective amplifier voltage noise $S_{V,amp}$ (thin solid lines) and the total thermal voltage noise $S_{V,th}$, which is obtained by subtracting $S_{V,amp}$ from S_V.

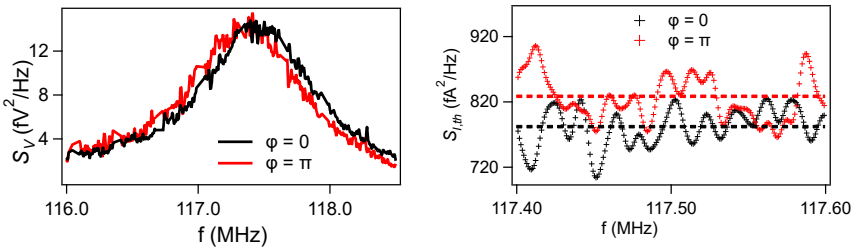

FIGURE 2.26 – **(a)** Closer look at the thermal voltage noise obtained from the extraction, at phase 0 and π. **(b)** Corresponding current noise. The dashed lines represent the mean value around resonance, and the phase-variation of this value is distinguisable from the uncertainty.

where $N \sim 200$ is the number of data points. Once the mean values are obtained at each phase, we can finally plot the phase-dependent $S_{I,th}$, with an example at $T = 50$ mK in Fig. 2.27(a). A linear background appears in $S_{I,th}$. This linear background could be coming from a small drift in G_{reso} with time. We can check the validity of the FDT by comparing the measured conductance to $S_{I,th}/4k_bT$. In Fig. 2.27(b) we show the difference in conductance between the uncorrected and the corrected G_{tot} : $G_{corrected} = G_{raw} + \text{slope}$. Since the response of the system should be periodic, removing the slope in either the conductance or the noise is justified, and adding the linear background to G_{tot} removes the linear background in $S_{I,th}$ as shown in Fig. 2.27(c).

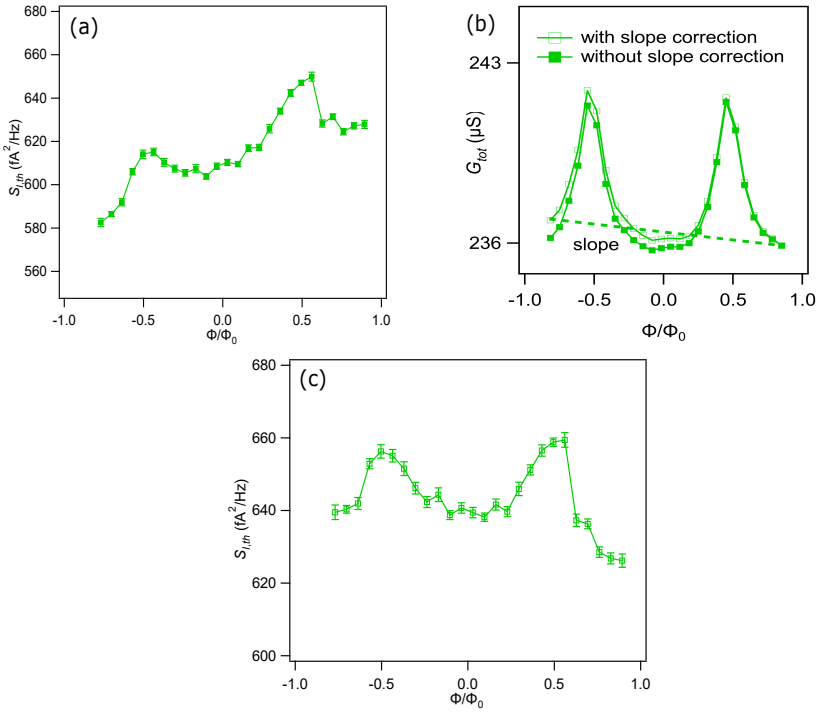

FIGURE 2.27 – Thermal noise and slope correction at T = 50 mK. (a) Example of $S_{I,th}(\Phi)$ directly obtained with the process described above. The linear background we observe is explained by the drift of G_{reso} with time. (b) The slope correction on G_{tot} mimics the drift of G_{reso} with time, even if G_{tot} must be periodic in Φ_0. The filled squares to G_{tot} obtained from inverting $S_{I,th} = 4k_BTG$ and the unfilled square is obtained by adding the linear background, shown in dashed line.(c) Thermal current noise $S_{I,th}$ obtained after the slope correction.

(b) Verification of the fluctuation-dissipation theorem

The validation of the fluctuation-dissipation theorem is given by

$$S_{I,th}(\Phi) = 4k_BTG_{tot}(\Phi) \tag{2.55}$$

We verify the fluctuation-dissipation theoreml for the whole system by comparing the noise measured with $4k_bTG_{tot}(\Phi)$ where $G_{tot}(\Phi)$ is deduced from the transmission measurement. The direct comparison between those two terms is plotted in Fig. 2.28. Several conclusions can be made :

- The plotted quantities are $S_{I,th}$ the **total** thermal noise and G_{tot} the **total** conductance.
- The quantitative agreement between the noise and the conductance for the phase independent baseline is the verification of the FDT for the resonator alone (which we assumed to be correct only at phase 0).
- The quantitative agreement between the phase-dependent parts is a direct demonstration of the FDT for the ring.
- The temperature entering in equation 2.55 is identical from the ones obtained in Fig. 2.8 giving the electronic temperature of the measurement

circuit. This result indicates a good thermalization between the Andreev bound states and the resonator. This is otherwise not trivial to confirm experimentally.

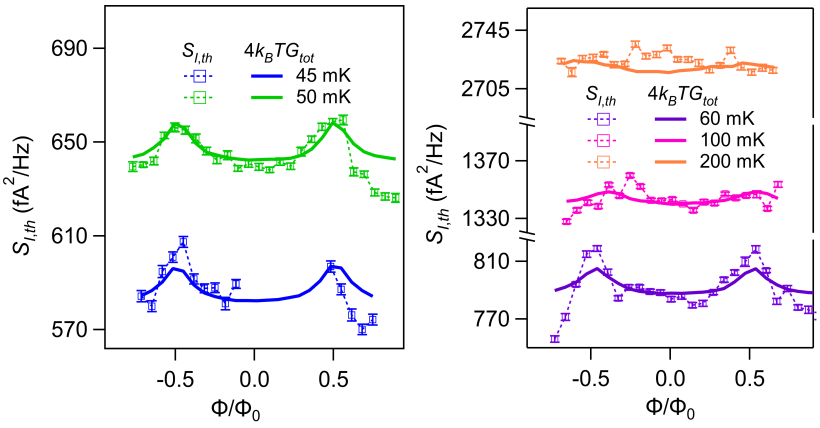

FIGURE 2.28 – Phase-dependent fluctuation-dissipation theorem : Comparison between $S_{I,th}$ (squares) and $4k_BTG_{tot}$ (solid lines). **(Left)** At T = 45, 50 and 60 mK. **(Right)** At T = 100 and 200 mK.

This measurement and experimental verification of the fluctuation-dissipation for such hybrid superconducting device paves the way for new studies on noise on more exotic system, and may be applied in the future to the topological SNS junction whose supercurrent thermal noise should reveal evidence of topological protection between the Andreev levels. [40]

2.5 . Understanding phase and temperature dependence of the conductance

The experimental results on the phase-dependence of L_j and G_j shown in section 2.4.1 can be a bit surprising in comparison with previous work from our group [29, 15, 27] in which the measured inductances and conductances are indeed strongly phase-dependent in a different range of frequency and temperature. This is nevertheless not the case in our system (Fig. 2.21), in which a weak phase-dependence is observed only at low temperature and disappears completely at high temperatures. The other striking feature is the confirmation of the strong temperature dependence of the junction's conductance, which exceeds at low temperature the Drude conductance. In this section, we provide an explanation of the observed weak phase-dependence of the conductance and its temperature dependence. We begin by performing numerical simulations and further calculations using linear response theory.

2.5.1 . Tight-binding model for the long diffusive SNS ring

We can write the Bogoliubov-de Gennes Hamiltonian describing the SNS junction as :

$$\mathcal{H} = \begin{pmatrix} H - E_F & \Delta \\ \Delta^* & E_F - H^* \end{pmatrix} \tag{2.56}$$

with H the Hamiltonian without superconductivity, E_F the Fermi level, $\Delta = \Delta_0 e^{i\varphi}$ the complex superconducting order parameter in which φ incorporates the phase difference between the two superconducting leads. $\Delta = 0$ in the normal part of the junction. The considered lattice is a two-dimensional square lattice of lattice parameter a, and this Hamiltonian is further discretized into :

$$\mathcal{H} = \sum_{n=1}^{N} [\epsilon_i \sigma_z + \Delta_0 e^{i\varphi}\sigma_x]|i\rangle\langle i| + \sum_{i \neq j} t_{ij}\sigma_z |i\rangle\langle j| \tag{2.57}$$

with the classical notations : i for the i-th site, N the total number of sites (normal and superconducting), $\sigma_{x,z}$ the Pauli matrices, ϵ_i the onsite potential and $t_{i,j} = -t$ the hopping term non-zero only when i and j are nearest neighbors. Considering half-filling, we chose $E_F = 4t$ so that the onsite potential reads $\epsilon_i = 4t - E_F + V_i = V_i$, with V_i the on-site random disorder uniformly distributed within range $[-D, D]$ (D being the disorder strength). Parameters are $D = 0.4t$ and $\Delta = 0.05t$., length $L = 160a$ and width $W = 20a$ so that the aspect ratio $L/W = 8$ reflects the experimental one. The Andreev spectrum calculated by diagonalizing the Hamiltonian for each phase between 0 and 2π and the obtained spectrum is shown in Fig. 2.29

From this spectrum, the minigap $E_g = 6.2\hbar v_F l_e/2L^2 = 0.005t$ [42] is read at phase $\varphi = 0$. Because $\hbar v_F = 2ta$ in this tight-binding model, the mean-free path can be calculated and is $l_e \approx 20a$. The obtained superconducting coherence length $\xi = \hbar v_F/2\Delta \approx 20a$, so that finally $\xi, l_e \approx L/10$, yielding a long diffusive regime.

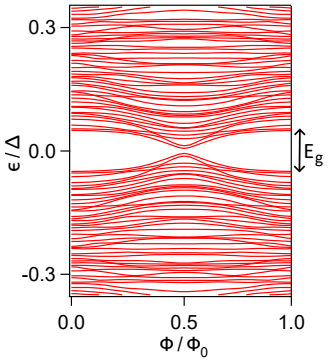

FIGURE 2.29 – Obtained Andreev spectrum from calculation using [41]. This spectrum is characteristic of a long diffusive junction. The important parameters are $L = 160a$, $W = 20a$, $D = 0.4t$, $\Delta = 0.05t$. We obtain $E_g = 0.005t$, $\xi \approx l_e \approx 20a$.

The current operator is computed in [15] and it reads :

$$\begin{aligned} J_{nm} &= \langle n|(\hbar/i)\nabla|m\rangle \\ &= \frac{\hbar}{i}\sum_{l,l'}\langle n|x_l,y_l\rangle\langle x_l,y_l|\nabla|x_{l'},y_{l'}\rangle\langle x_{l'},y_{l'}|m\rangle \\ &= \frac{\hbar}{l}\sum_{l}\Psi_n^{e*}(x_l,y_l)[\Psi_m^e(x_l+1,y_l)-\Psi_m^e(x_l,y_l)] \\ &+ \Psi_n^{h*}(x_l,y_l)[\Psi_m^h(x_l+1,y_l)-\Psi_m^h(x_l,y_l)] \end{aligned} \tag{2.58}$$

where $\Psi_n^{e/h}(x_l,y_l)$ corresponds to the electron/hole components of the wavefunction at position (x_l,y_l). From this expression and using linear response theory [29, 15], the junction conductance at finite frequency ω is :

$$\begin{aligned} G_j &= G_D + G_{ND} \\ G_D &= -\hbar\sum_n |J_{nn}|^2 \frac{h\gamma}{(\hbar\omega)^2+(h\gamma)^2}\frac{\partial f_n}{\partial E_n} \\ G_{ND} &= -\hbar\sum_{n\neq m} |J_{nm}|^2 \frac{h\gamma}{[\hbar\omega-(E_n-E_m)]^2+(h\gamma)^2}\frac{f_n-f_m}{E_n-E_m} \end{aligned} \tag{2.59}$$

with γ the inelastic scattering rate and f the Fermi-Dirac distribution.

2.5.2 . Phase dependence of G_D and G_{ND}

We now dig into more details of the response function. We remind that the relative magnitudes between the working frequency ω, the inelastic scattering rate γ (equivalently τ_{in}^{-1}), E_g the minigap and temperature T define the shape of the inductance (the reactive response) and the conductance (the dissipative response) as a function of phase. The first observation is that the shape of the inductance L_j hints towards the adiabatic regime. In this case the inductance is given by the derivative of the current-phase relation of the junction (a sine with additional harmonics), consistent with the previous work from the group [29]. This was used

when we integrated L_j in order to obtain the CPR of the junction. The conductance is a bit more difficult to understand at first glance. There is a big difference between the ring's conductance G_{ring} and the junction's one G_j. As explained before, the phase-dependence observed via G_{ring} is dominated by screening effects, whereas the conductance G_j of the junction is nearly phase-independent. Let us summarize the different time and energy scales :

— The working frequency is around 117 MHz, leading to hf = 6 mK $\ll$ k_BT in the experiment. This frequency is smaller than the frequency previously investigated.

— Furthermore, from I_c(T) obtained in Fig. 2.16(b) we get E_{Th} = 30 mK and $E_g(\varphi = 0) = 3.1E_{Th}$. Hence, at high temperature, we have $k_B T \gg E_g \gg hf$.

The last relevant quantity to be determined in the ordering is then γ. The previous experiments performed in our group [29] yielded $\gamma \approx 5$ GHz for $T > 500$ mK. However the present experiment was performed at much lower temperature. Two other considerations differentiate the experiments :

— They used multimode resonators, whereas here use a single-mode resonator. The use of a single-mode resonator should reduce the inelastic scattering caused by the environment. [43]

— The quality of the gold wire : in the previous experiment they used Au 6.9 (99.9999% pure gold) and in our case we used Au 5.9.

limiting the comparisons with the previous experiments. In order to estimate the range of γ, we perform the numerical simulations with several values of γ to see which order of magnitude yields a result similar to the one of the experiment. To simulate the high temperature behaviour, the parameters used are :

— $E_g = 0.005t$

— $k_B T = 4E_g$

— $hf = 0.02E_g$

The calculated G_j and its two components are shown in Fig. 2.30.

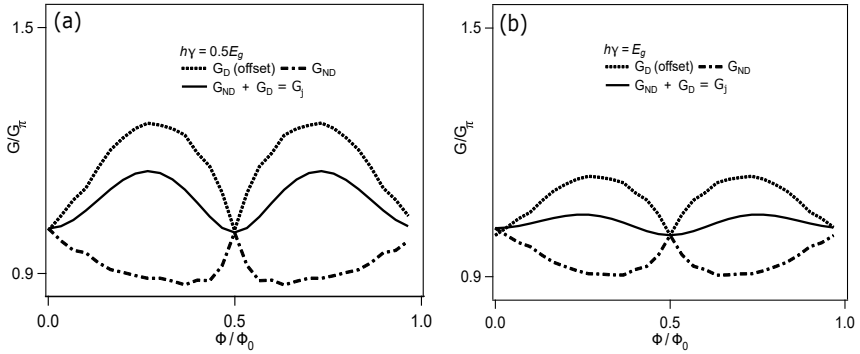

FIGURE 2.30 – Calculated $G_j(\phi)$ with $k_B T = 4E_g$, $\hbar\omega = 0.02E_g$ and in **(a)** $h\gamma = 0.5E_g$, in **(b)** $h\gamma = E_g$. A slightly higher $h\gamma$ than E_g weakens the phase-dependence of G_j. The curves are normalized by $G_\pi = G_j(0.5\Phi_0)$. G_D is 0 at $\Phi = 0.5\Phi_0$ and is offset for the comparison with G_{ND}.

The result for $h\gamma \sim E_g$ is similar to the experimental result. Then, in order to

recover the weak phase-dependence of the conductance and considering the results already obtained, the regime to consider is the following :

$$hf \ll E_g \lesssim h\gamma \lesssim k_B T \tag{2.60}$$

This is further seen analytically when taking the expressions of G_D and G_{ND} of equations 2.59. In both G_D and G_{ND}, we can use $\hbar\omega = 0$ since the frequency is the lowest energy scale. $\partial f_n/\partial\epsilon_n$ is proportional to $1/T$. Therefore we rewrite G_D as :

$$G_D \propto -\frac{1}{(\gamma T)} \sum_n |J_{nn}|^2 \tag{2.61}$$

The main difficulty is in simplifying G_{ND} as the energy difference between levels appear in its expression. We are interested in the phase-dependence, which the spectrum of Fig. 2.29 shows that the largest phase dependence comes from the states closes to the Fermi energy and from levels that are symmetrical around it. Considering the phase dependance, we can argue that $E_n - E_m < E_g$. From the calculated G_j using our model and shown in Fig. 2.30, the regime closer to the experiment yields $h\gamma > E_g$. Considering that the higher the levels, the less the contribution, the second term can be approximated by its derivative :

$$\frac{f_n - f_m}{E_n - E_m} \approx \frac{\partial f_n}{\partial E_n} \tag{2.62}$$

yielding

$$G_{ND} \propto -\frac{1}{\gamma T} \sum_{n \neq m} |J_{nm}|^2 \tag{2.63}$$

Finally, the total conductance can be written :

$$G_j \propto \frac{1}{\gamma T} \left(\sum_n |J_{nn}|^2 + \sum_{n \neq m} |J_{nm}|^2\right) \tag{2.64}$$

$$\approx \frac{1}{\gamma T} \mathrm{Tr}(J^2) \tag{2.65}$$

where we extended the sum to all the levels since the contribution of the highest levels is negligible. The trace of the current operator does not depend on the Aharonov-Bohm phase because

$$\mathrm{Tr}(\mathcal{H}) = \frac{m}{2e^2} \mathrm{Tr}(J^2) + \mathrm{Tr}(V) \tag{2.66}$$

does not depend on the phase, as it can be seen in [15] and detailled in Fig. 2.31.

This simple analysis reveals explains the unexpected phase-indepedence of the conductance of the SNS junction. From the simple expression of equation 2.65, we also recover the temperature dependence observed experimentally and predicted in [38].

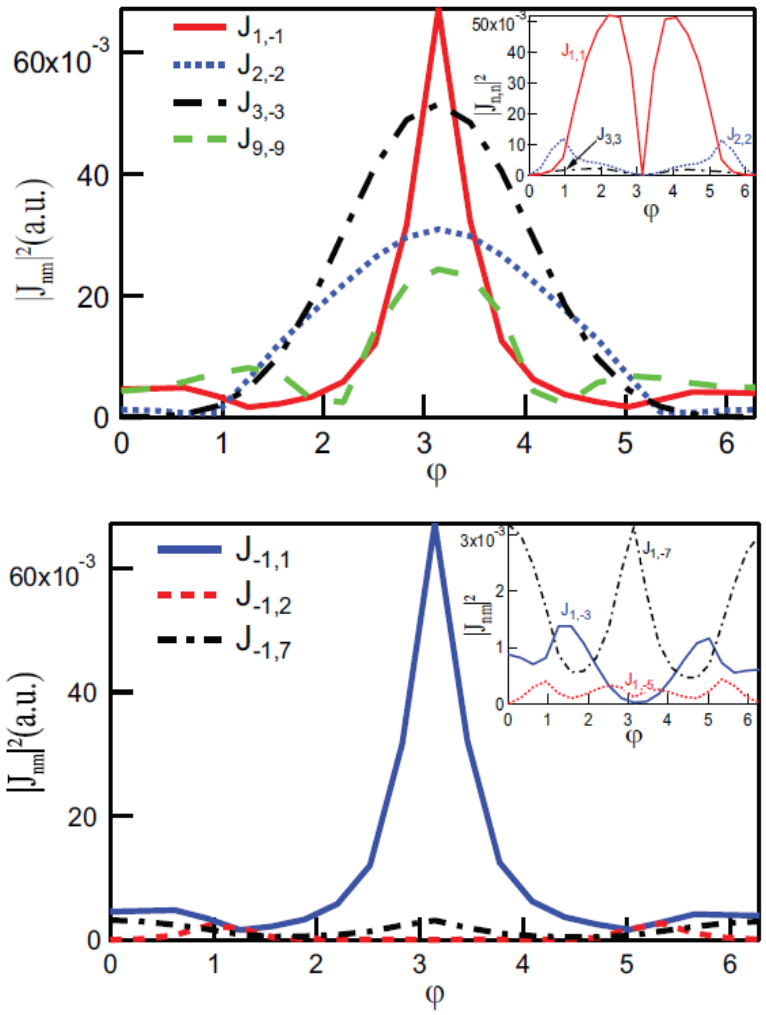

FIGURE 2.31 – (Top) $|J_{n,-n}|^2$ for $n = 1, 2, 3$ calculated from the exact diagonalization of the Bogolioubov-de Gennes equations for a long diffusive SNS junction. The inset is the calculated $|J_{nn}|^2$. The addition of these two quantities is almost phase-independent, and the higher n is, the less phase-dependent is the matrix element. (Bottom) $|J_{-1,m}|^2$ and $|J_{1,-m}|^2$ (inset) with $m = 1, 2, 3, 7$. Again, the main contribution comes from $n = -m$ as explained in the main text. $J_{1,-m}$ is at least an order of magnitude lower.

2.6 . General conclusion

In this PhD work, we have demonstrated that the supercurrent flowing through an SNS junction is actually noisy, i.e. the supercurrent presents thermal fluctuations at equilibrium. This has been done thanks to the high freqyency set-up based on a ultrasensitive cryogenic amplifier, which allowed us to detect independently the conductance and the noise of the junction. The careful comparison between these two quantities yields a first experimental demonstration of the FDT in an SNS junction. Indeed, although FDT tells us that conductance and noise yields the same information, they are not equivalent experimentally. Equilibrium noise measurements, although more challenging, provide a unique advantage over other measurements that involve sample biasing, for which the linear regime can not be maintained over the full current versus phase relation.

3 - Ballistic hinge states in multilayer tungsten ditelluride

This chapter is devoted to the study of multilayer tungsten ditelluride and its supposed higher order topological insulator phase. This part can be divided into three main components :

— In the first part, we give a short introduction to topology in condensed matter physics in section 3.1. We develop two main properties of the topological insulators : band inversion and topological protection. We finally describe the superconducting proximity effect in those systems.

— A second part is dedicated to the presentation of tungsten ditelluride, the material probed during this PhD, as well as some of its properties. This is the purpose of section 3.2.

— Finally, the last sections are dedicated to the experiments we perform, from the principle of the experiment 3.3, fabrication 3.4, measurement techniques 3.5 and the results obtained 3.6.

3.1 . Introduction to topological insulators

This introduction to topology in condensed matter is inspired by M. O. Goerbig's lecture notes [44] and online courses available online from Delft University of Technology [45].

3.1.1 . Topological band structure

Electronic properties of a material can be determined by their band structure. A material is said to be insulating if its Fermi level lies in the gap between the conduction and valence bands. Contrary to a conventional insulator, a topological insulator is characterized by a band inversion [46], in which the curvature of the bands (the mass, $m \propto (\partial^2 E/\partial k^2)^{-1}$, changes sign). The first model of topological insulator proposed in [47] proposed that a strong spin-orbit coupling gaps the crossing point of the inverted bands and non trivial topology can emerge in the bulk material. This non trivial topology manifests itself as the presence of conducting states at the surface as stated by the bulk-edge correspondence principle. This idea is summarized in Fig. 3.1.

The first example of 3D material insulating in the bulk and conducting in the surface is Bi_xSb_{1-x} [50, 51]. In a 2D TI, the surface is insulating and the 1D edges are conducting. This was theoretically expected and measured a year later in HgTe quantums wells [52, 53]. In 2017 and 2018, the idea of *higher-order topological insulators* emerged, characterized by gapped bulk and surface states but 1D conducting hinges [54, 55, 56, 57]. A second (higher) order topological insulator is characterized by a double-band inversion, illustrated in Fig. 3.2.

A simple classification can be made depending on the dimension of the material and the dimension of conduction :

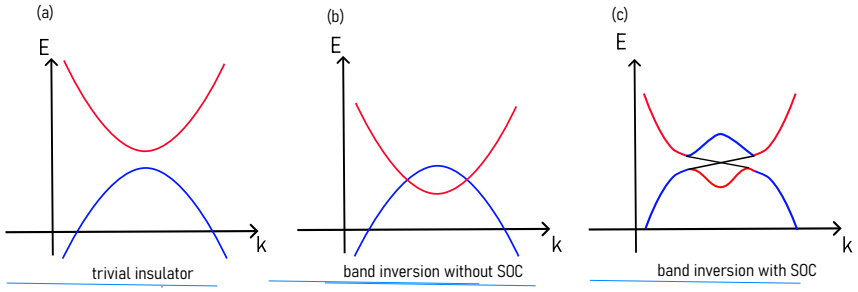

FIGURE 3.1 – Schematic representation of band inversion and comparison with a trivial insulator. (a) Band structure of a trivial insulator. The valence band is represented in blue and the conduction band in red. There is a gap between the two bands and the Fermi energy (not represented) is between the valence and conduction band. (b) Band structure and band inversion without (or with weak) spin-orbit coupling. The band inversion is illustrated with the switching between the red and blue curves between the two crossing points, and corresponds to a change in the sign of mass $m \propto (\partial^2 E/\partial k^2)^{-1}$. (c) When combined, band inversion and SOC leads to gapped bulk states but metallic surface states, represented by the black solid lines. Adapted from [48, 49].

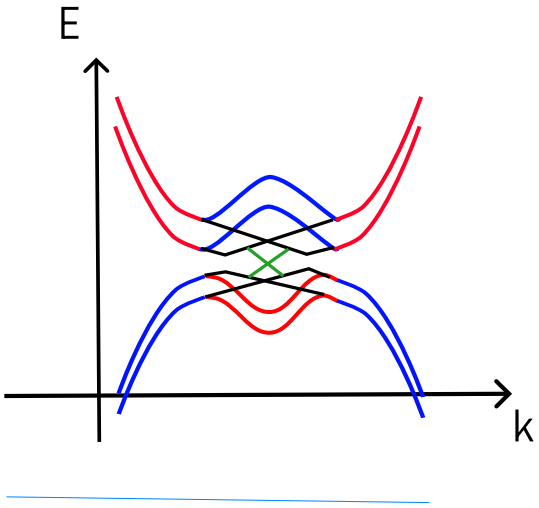

FIGURE 3.2 – Illustration of the double-band inversion. The red and blue linesare inverted twice. The black solides lines are gapped surface states and the green lines the conducting hinge states. Adapted from [49].

— A material of dimension d, conducting in dimension $d-1$ and lower is said to be a first-order topological insulator.
— A material of dimension d, insulating in dimension d and $d-1$ but conducting in dimension $d-2$ is said to be a second-order topological insulator.

An example of this classification is shown in Fig. 3.3.

These materials convey specific properties compared to an ordinary insulator. In particular, their conducting states are protected by the conservation of a topological invariant as explained below.

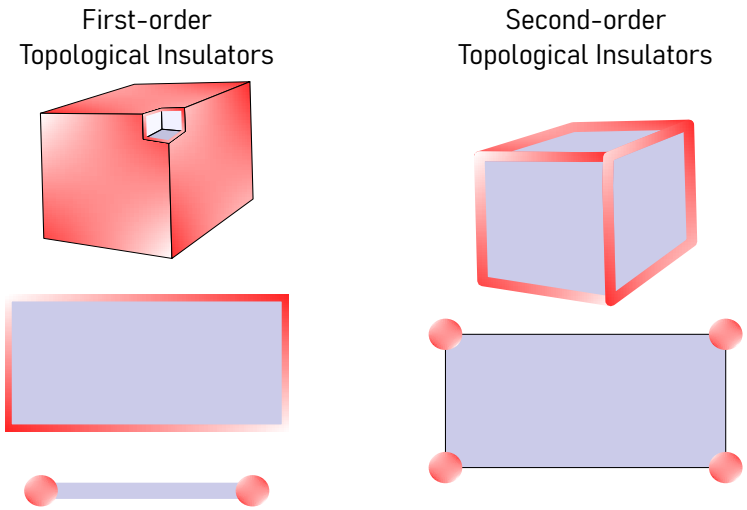

FIGURE 3.3 – First-order and second order topological insulators in various dimensions. The first-order TIs of dimension d (left column) exhibit conduction in dimension $d-1$, whereas the second order TIs of the same dimension show conduction only in dimension $d-2$.

3.1.2 . Topological protection and spin-momentum locking

Let us consider the case of a 2D topological insulator, with an insulating bulk and conducting edges. The symmetry and presence of SOC impose that edge states are helical : their spin is tied to the momentum direction : this is the spin-momentum locking.

This spin-momentum lockin is of major importance as it protects the states from disorder. For instance backscattering is forbidden for a non-magnetic impurity since backscattering requires spin-flip event. This process is illustrated in Fig. 3.4

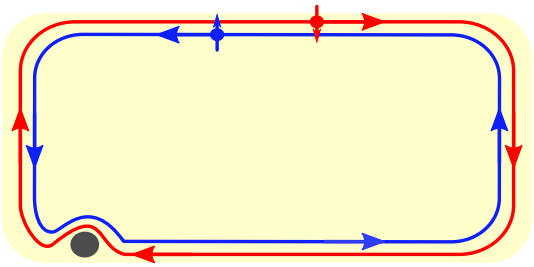

FIGURE 3.4 – Illustration of the spin-momentum locking and topological protection on a 2D topological insulator. The surface of the material is insulating and the direction of motion of the electrons at the hinges is associated to a spin. For an electron to backscatter on the grey impurity, it spins should change sign (from red to blue). The helical states "ignore" the impurity.

3.1.3 . Superconducting proximity effect and topological insulators

In this PhD, we were interested only in 1D helical states, that is to say that the material we probed were either a 2D topological insulator or a 3D second-order

topological insulator. In this part, we discuss the effect of induced superconductivity on the edge states of the topological insulator.

We consider the junction of Fig. 3.5, and the calculated Andreev spectrum in the short and long junction regimes.

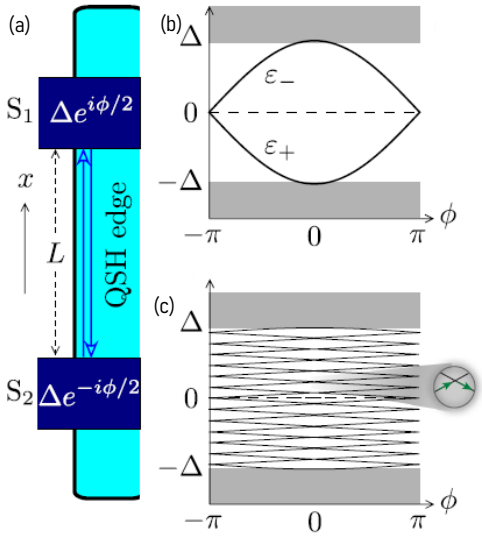

FIGURE 3.5 – (a) Representation of the S/QSHI/S junction considered, with spin-determined ballistic channels at the edges represented by the two opposite arrows. (b) Andreev spectrum in the case of the short junction as calculated in [40]. (c) Andreev spectrum calculated in the long regime in [58]. The change of slope in the spectrum is highlighted by the two green arrows. From [58].

The two spectra are very similar to the ballistic junctions presented in 1.5. However, contrary to the conventional case, the level crossed at π and so the state with minimum energy corresponds to two different level in a full period. If we take the example of the short junction, the state of minimum energy is the state with energy ε_+ between $-\pi$ and π, whereas between π and 2π it is the state with energy ϵ_-. The crossing at phase π is protected by the conservation of a topological number called the fermion parity (which corresponds to the number of fermions on one edge). This fermion parity conversation makes the spectra period in 4π instead of 2π as in a conventional SNS junction : this is refered to as the fermion parity anomaly. [40]

This 4π-periodicity should be seen in the current-phase relation as it is the derivative of the Andreev spectrum. However, quasiparticle poisoning and non-adiabatic transitions may restore the 2π-periodicity of the conventional junction. If we take the example of the spectrum presented in Fig. 3.5, this would be equivalent for the ABS to follow the negative energy branch, hence a similar spectrum as the ballistic but spin-degenerate ABS. However the ballistic CPR with a critical current of $eE_{Th}/\hbar$, is a tell-tale sign of topological transport in these material [58] as illustrated in Fig. 3.6, and it was one of the first indication of Bismuth being a HOTI [25].

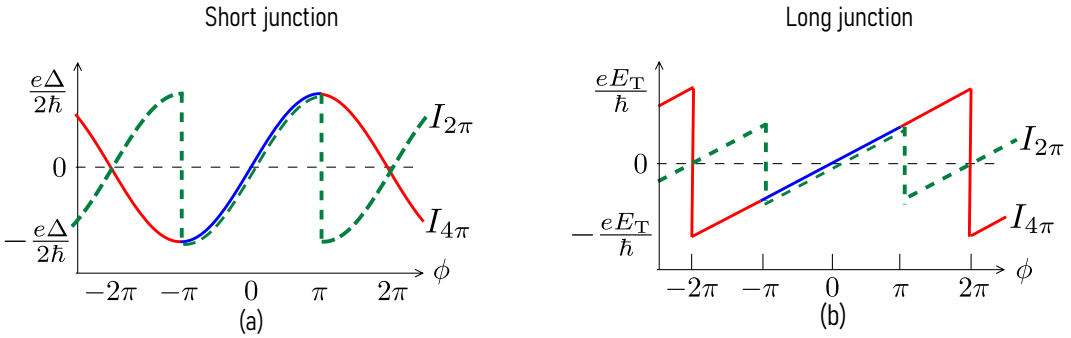

FIGURE 3.6 – CPR of topological junction in the **(a)** short and **(b)** long limit. The dashed green line represent the conventional ballistic junction whose CPR is 2π-periodic. The red and blue continuous lines represent the current of the positive and negative energy branches of the spectrum, yielding the 4π-periodic CPR. In the long regime, the factor 2 difference in the amplitude of the current is a sign of 4π-periodicity. Adapted from [58].

3.2 . Topological phases of Tungsten Ditelluride

Tungsten ditelluride (WTe_2) is one example of transition metal dichalcogenide (TMDs). TMDs are materials of the form MX_2 where M is a transition metal atom (M = W, Mo for instance) and X a chalcogen atom (O, S, Se, Te, Po and Lv) [1] whose first interest was their nature close to graphene but with different electronic properties : they are layered materials with weak Van der Waals interactions between the layers.

In 2014 it has been proposed that monolayers of MX_2 are QSHI [59] with the 1T'- structure shown in Fig. 3.7.

Among the TMDs, monolayer WTe_2 is the perfect candidate to observe the quantum spin Hall effect as it grows naturally in the 1T' structure. Monolayer WTe_2 was shown to be a perfect insulator with edge conduction [61, 62], STM measurements shown the existence of the topological states [63] and the quantum spin Hall effect has been observed up to 100 K in 2018 [64].

The case of the 3D crystal is however more complex. In the form of a 3D crystal, or multilayer, WTe_2's structure is changed towards its Td-phase, illustrated in Fig. 3.7. The first striking property of WTe_2 is its extremely large magnetoresistance [65], taking its origin from the compensation of the electrons and holes pockets [66, 67, 68].

However, the first topological phase identified for multilayer WTe_2 was its Type-II Weyl semimetallic state [69], whose typical band structure is illustrated in Fig. 3.8.

First experimental evidences of this Weyl nature were shortly found : extra quantum oscillations of the resistance due to the Weyl orbits [70] or asymmetric Josephson effect [71, 72]. Theoretical predictions concluded that WTe_2 would exhibit

1. The ones generally studied are Sulfur, Selenium and Telluride. Polonium and Livermorium are highly radioactive.

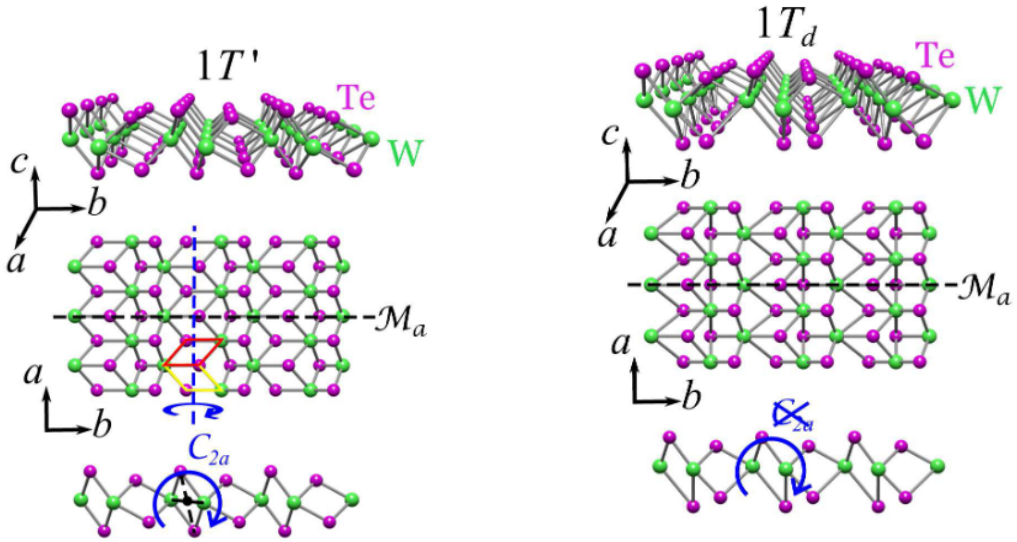

FIGURE 3.7 – Structure of WTe_2. W atoms are in green, Te atoms in purple. (Left) in its monolayer form. This structure is characterized by the mirror plane $\mathcal{M}_a$ and the screw rotate symmetry $\mathcal{C}_{2a}$. (Right) in its multilayer form. In this case, the rotational symmetry is broken. From [60].

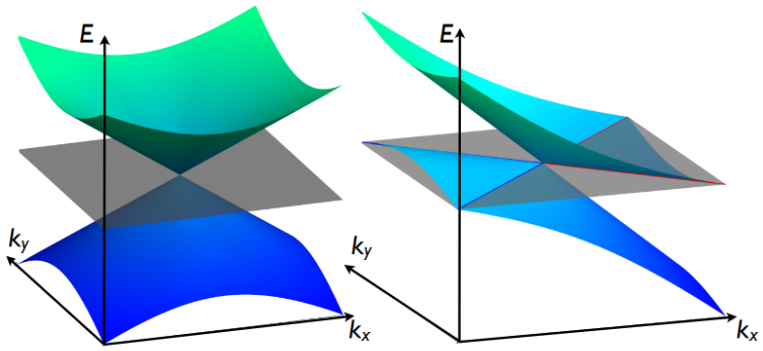

FIGURE 3.8 – Typical band structure of the two possibles Weyl semimetals (WSM). (Left) Type I with point-like Fermi surface. (Right) Type II. The cones are tilted and the Weyl point is the touching point between the electron and hole pockets. WTe_2 was predicted to be the first example of type II WSM. From [69].

8 Weyl points [73]. However, the Fermi arcs (surface) states observed in ARPES measurement were not sufficient to justify the existence of Weyl nodes in WTe_2 [74].

It seems that WTe_2 is a quantum spin Hall insulator when exfoliated up to its monolayer (1T' structure), but that the 3D crystal exhibits an other topological phase (1Td structure). A theoretical investigation [75] first made the prediction of a HOTI phase existing in multilayer WTe_2. The surface states were found to be inconsistent with the Fermi arc scenario from ARPES measurement and were suggested to be "vestiges of a HOTI phase, close in parameter space" [75]. This

could be explained by the relative resemblance between the 1Td and the 1T' crystal structure : under realistic experimental conditions, a small strain could annihilate the Weyl points and results in a HOTI phase [76, 75]. This HOTI phase takes its origin from double band inversion, like bismuth. [77], and illustrated in Fig. 3.9

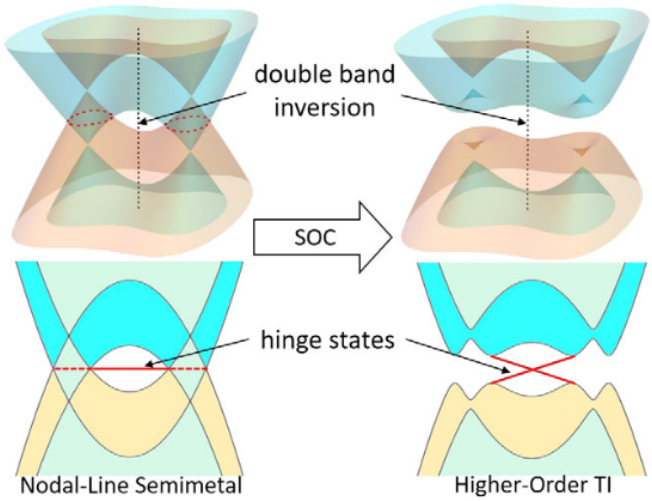

FIGURE 3.9 – Origin of the HOTI phase of multilayer WTe_2. The nodal line semimetal phase is another type of topological phase, not described in this manuscript. The double band inversion process is seen without and with SOC. In the first case, it results in a higher-order topology in a bulk-gapless system, whereas in the second case we recover the higher-order topological insulating phase. From [75].

Even if it exhibits a HOTI phase, i.e. it has topological conducting states at its hinges, WTe_2 remains a semimetal, and the distinction between topological and non-topological states in a non-superconducting system is difficult. This led to the first experiments [78, 79, 80] performed on multilayer WTe_2 using the Josephson effect. The three experiments indicate the existence of topological hinge states only along its a-axis, as summarized in Fig. 3.10. However, the ballistic nature remained elusive in these experiments. This idea is the purpose of our experiment. To do so, we measure the current-phase relation of the states localized at the hinges of WTe_2.

3.3 . Current-Phase Relations measurements

Since the CPR is one of the best tool to probe the nature of transport in a conductor, we introduce in this section the tool used during this work : the asymmetric DC Supercurrent QUantum Interference Device (SQUID). We start with an introduction on the DC SQUID.

3.3.1 . Superconducting Quantum Interference Device

The DC SQUID consists on two Josephson junctions in parallel, illustrated in Fig. 3.11. We consider that these junctions, indexed by $i = 1, 2$, are described

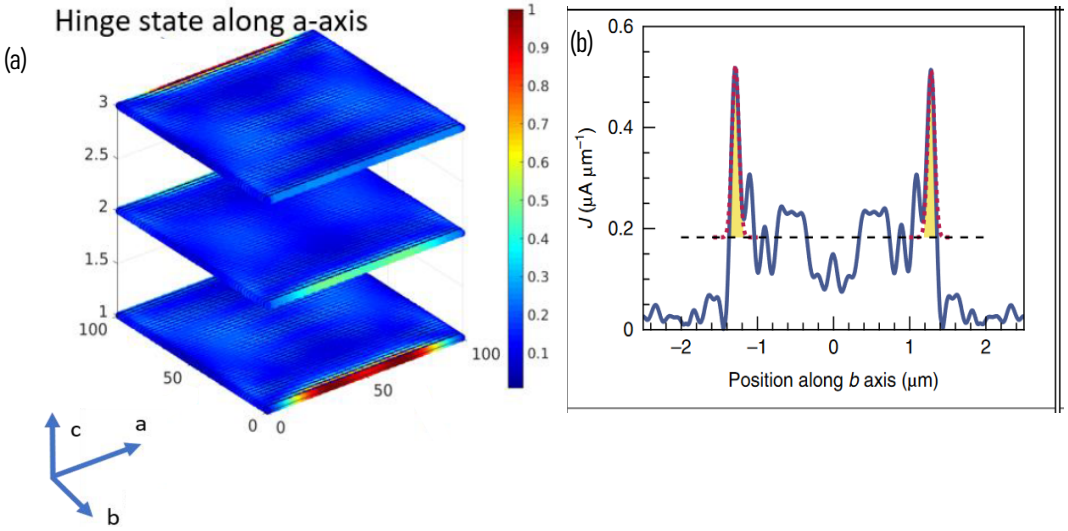

FIGURE 3.10 – (a) Calculated wavefunction of the hinge states as a function of the position of the position in multilayer WTe_2, in the case of a conducting bulk. The edge states along the b-axis are merged into the bulk states but this is not the case along the a-axis. Furthermore, they show that the hinge states are localized on opposite hinges of the flake. (b) Current spatial distribution for a thick WTe_2-based SNS junctions. The bulk states are uniformly distributed along the b-axis, hence the threshold at 0.2 µA/µm. The peaks appearing at the edges of the current distribution correspond to the edges of the flake when the leads are parallel to the b-axis, i.e. the states are localized along the a-axis. From [78].

by their critical current $I_{c,i}$ and a generic current-phase relation $f_i(\varphi_i)$ with φ_i the phase difference between the superconducting leads of junction i, such that we have :

$$I_i = I_{c,i} f_i(\varphi_i), \quad i = 1, 2 \tag{3.1}$$

We apply a magnetic field B imposing a flux $\Phi_{ext} = B \times S$.

The fluxoid quantization gives the relation between the phase difference for both junctions and the flux :

$$\varphi_1 = \varphi_2 + \frac{2\pi\Phi_{ext}}{\Phi_0} + 2\pi n \tag{3.2}$$

and we can write the total current in the SQUID, recalling that the CPRs are 2π-periodic :

$$\begin{aligned} I(\varphi_1, \varphi_2) &= I_{c,1} f_1(\varphi_1) + I_{c,2} f_2(\varphi_2) \\ &= I_{c,1} f_1(\varphi_2 + \frac{2\pi\Phi_{ext}}{\Phi_0}) + I_{c,2} f_2(\varphi_2) \\ &= I_{c,1} f_1(\varphi_2 + \frac{2\pi B \times S}{\Phi_0}) + I_{c,2} f_2(\varphi_2) \\ &= I(B, \varphi_2) \end{aligned} \tag{3.3}$$

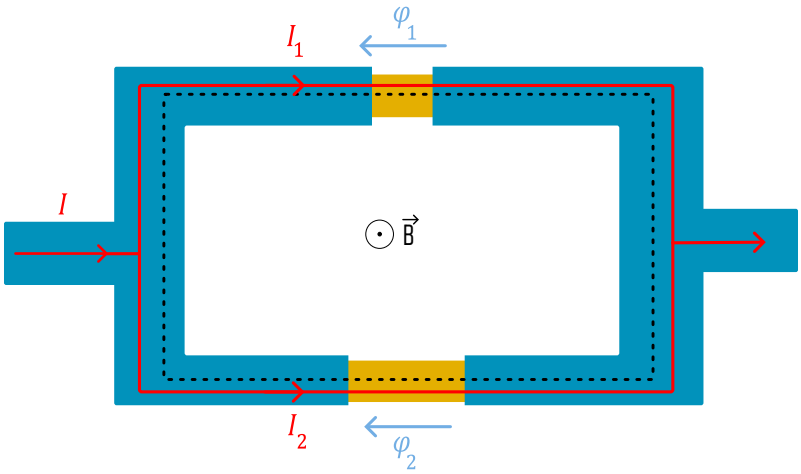

FIGURE 3.11 – Sketch of a DC Superconducting QUantum Interference Device (SQUID). The superconducting parts are drawn in blue and the normal part of the junction in yellow. The surface of the SQUID is highlighted by the black dashed line. When we apply a magnetic field B perpendicular to the SQUID, a flux Φ_{ext} passes through the surface. The red solid line corresponds to the current going through the two junctions placed in parallel, described by their phase difference φ_i with $i = 1$, 2. The total current in the SQUID is thus $I = I_1 + I_2$.

The measured quantity is not the current-phase relation of the whole SQUID but its maximal value, i.e. the critical current of the SQUID. For clarity we change the notations with $i_1 = I_u$ and $I_2 = I_{ref}$ and we consider an asymmetric situation in which $I_{c,ref} \gg I_u$. The critical current of the SQUID is defined as :

$$\begin{aligned} I_c(B) &= \max_{\varphi_2}[I(B,\varphi_2)] \\ &= I(B,\varphi_2^{max}) \\ &\approx I_u(\varphi_2^{max} + \frac{2\pi B \times S}{\Phi_0}) + I_{c,ref} \end{aligned} \tag{3.4}$$

with $I_{c,ref} = \max_{\varphi_2}[I_{ref}(\varphi_2)] = I_{ref}(\varphi_2^{max})$ is the phase that maximized the current in this junction. From this equation we see that the only magnetic field dependence comes from the term $I_u(\varphi_2^{max} + \frac{2\pi B \times S}{\phi_0}$. The critical current of the asymmetric DC SQUID shows modulations that is the CPR of the unknown junction, which has a lower critical current than the reference junction. An illustration of the quantity measured can be seen in Fig. 3.12

This perfect scenario however doesn't take into account other effects of the magnetic field that can happen in a SNS junction, such as the diffraction phenomena, which is the subject of the next subsection.

3.3.2 . Diffraction phenomena in a single Josephson junction

(a) General derivation

As a consequence of the wavelike nature of the Cooper pair, a striking feature of the Josephson junction are the diffraction phenomena of the supercurrent when

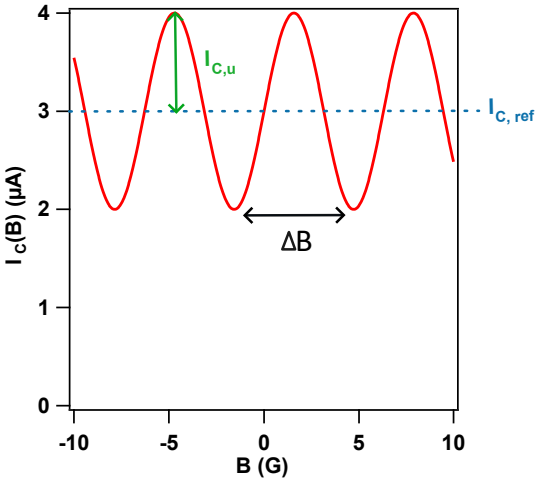

FIGURE 3.12 – Illustration of the critical current of a SQUID. From this curve, it can be seen that the reference junction has a critical current of 3 µA (blue dashed line), and the CPR of the unknown junction is a sine (red) with critical current 1 µA (green arrow). The period ΔB is given by the surface of the SQUID.

magnetic fields are applied. These phenomena, first described with the SIS junction, still exist in the case of the SNS junction. Inspired by [81], we start by recalling the diffraction effect in a Josephson junction. This leads to explaining the shape of the diffraction pattern in the case of a SNS junction placed in a perpendicular field as it will be important to understand the experimental results later on. We consider a 2D Josephson junction of length L along the x-axis and width w along the y-axis. The junction is placed in a magnetic field in the perpendicular direction $\overrightarrow{B} = B_0\overrightarrow{u_z}$. The junction is represented in Fig. 3.13.

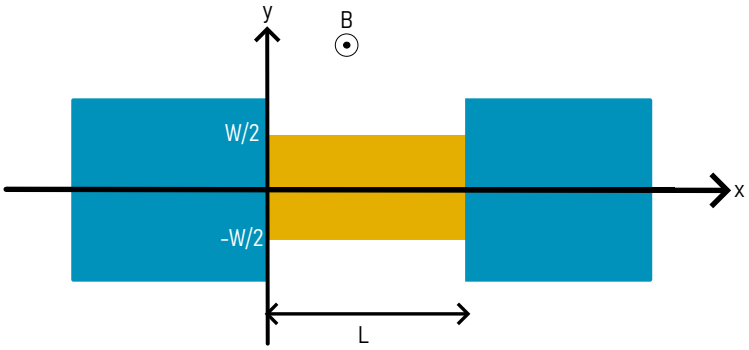

FIGURE 3.13 – Sketch of the Josephson junction we consider for the following derivation. Superconductors are in blue and the weak link in yellow. The normal part is of length L (x-axis) and width w (y-axis). A magnetic field is applied perpendicularly to the junction, on the z-axis.

We have chosen the gauge $\overrightarrow{A} = -By\overrightarrow{u_x}$ with $\overrightarrow{A}$ the vector potential and we

introduce the gauge-invariant phase-difference

$$\theta = \varphi - \frac{2\pi}{\Phi_0} \int \overrightarrow{A} \cdot d\overrightarrow{r} \tag{3.5}$$

with φ the superconducting phase difference between the two superconducting leads. The phase acquired by a pair transmitted ballistically from a vertical coordinate y across the junction reads :

$$\theta = \varphi + \frac{2\pi\Phi}{\Phi_0} \frac{y}{w} \tag{3.6}$$

with $\Phi = BLw$ the flux inside the insulating part. The Dynes and Fulton description [82] allows for the computation of the supercurrent based on a few approximations :

— The low-transparency of the interfaces. This approximations yields a sinusoidal current-phase relation for one state.

— The supercurrent flows perpendicularly to the leads and the supercurrent density only depends on the y coordinate.

This yield the total current in the considered junction to be expressed as :

$$I(\Phi, \varphi) = \int_{-w/2}^{w/2} dy j(y) \sin(\varphi + \frac{2\pi\Phi}{\Phi_0} \frac{y}{w}) \tag{3.7}$$

and $j(y)$ is the current density profile of the junction. The total current results from the weighted integration over all the CPRs. Similarly to the calculation presented in section 3.3.1 for the DC SQUID, if we maximize with respect to φ equation 3.7, we obtain the critical current with respect to Φ (equivalently B) and the so-called diffraction pattern $I_c(B)$ [2]. This transformation can be seen as the Fourier transform of the current distribution $\mathcal{F}[j(y)]$:

$$\begin{aligned} I_c(B) &= \max_\varphi |I(\Phi, \varphi)| \\ &= \mathcal{F}[j(y)] \end{aligned} \tag{3.8}$$

The approximation of $I_c(B)$ being the Fourier transform of the current distribution is technically only true when the CPR consider is purely sinusoidal and the geometry purely rectangular. However, we will see in the following that this definition can be extended and it was used in particular to evidence the edge states of topological insulator.

(b) Uniform current distribution : Fraunhofer pattern

In the case of a uniform current distribution, $j(y)$ can be expressed as :

$$j(y) = \frac{I_c}{w} \tag{3.9}$$

2. We wish to avoid any confusion between $I(\varphi)$ the current-phase relation and $I_c(\Phi)$ the diffraction pattern with Φ the flux, hence the choice of $I_c(B)$ for the notation.

and we can inject this expression onto equation 3.8. It yields the standard Fraunhofer pattern :

$$\frac{I_c(B)}{I_c(B=0)} = |\,\mathrm{sinc}(\pi\frac{\Phi}{\Phi_0})| \tag{3.10}$$

Barone and Paterno [83] performed the calculations on SIS junction with different geometry, highlighting the dependence on the shape of the junction of the diffraction pattern. For comparison we show the difference between the rectangular geometry we deal with and a circular geometry in Fig. 3.14.

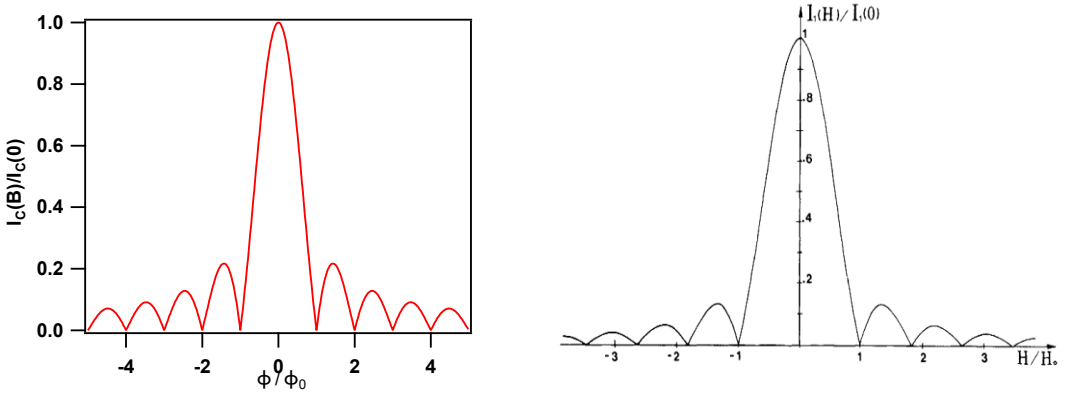

FIGURE 3.14 – (Left) Fraunhofer pattern calculated for a rectanguler junction following equation 3.10 : the central peak and the second maximum are distant by $1.5\phi_0$ and ϕ_0 after. (Right) Theoretical curve for a circular junction, from [83]. The periodicity changes in the circular junction as well as the amplitudes of the different lobes : for instance the second maximum is before $\phi = 1.5\phi_0$ and the distance between those maxima becomes irregular.

(c) SNS case : the example of the long diffusive junction

The case of the SNS junction is a bit harder to describe as a sinusoidal CPR doesn't exist with current flowing only perpendicularly to the superconducting leads. Let us take the case of the diffusive junction, for which the Fourier decomposition of the current-phase relation can be written :

$$I(\varphi) = \sum_n I_{c,n} \sin(n\varphi) \tag{3.11}$$

For which we summarize the results obtained theoretically for the diffusive by Cuevas and Bergeret [84] and experimentally by our group [85] in 3.15. The aspect ratio of the junction plays a major role in the diffusive SNS case. The larger and shorter ($W \ll L$, with W the width and L the length) the junction is, the more the diffraction pattern we observe is similar to the one presented in Fig. 3.14. On the other hand it highly differs from the Fraunhofer case when $L \gg W$ with a

gaussian diffraction pattern decaying . The diffraction pattern in a diffusive junction is then more complex and a specific attention will be given to it when we present our experimental results.

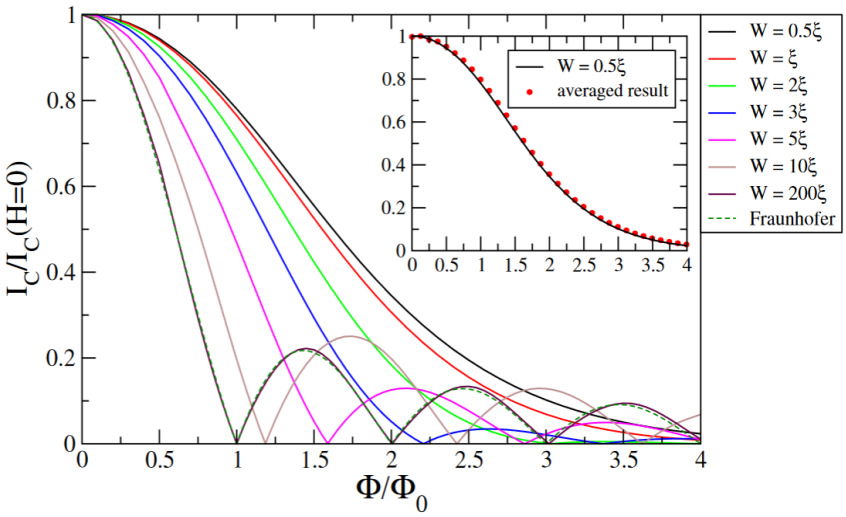

FIGURE 3.15 – (a) Diffraction pattern for several aspect ratio. $L = 8\xi$ is fixed and the width W varies from $L/16$ to $25L$. From [84].

It is important to note that all the phenomena describe can coexist within the SQUID experiment : for instance a gaussian pattern could be modulated by a sinusoidal CPR, as illustrated in Fig. 3.16 where the example of two sinusoidal Josephson junctions have been put in parallel but with $I_{c,ref} \gg I_{c,u}$.

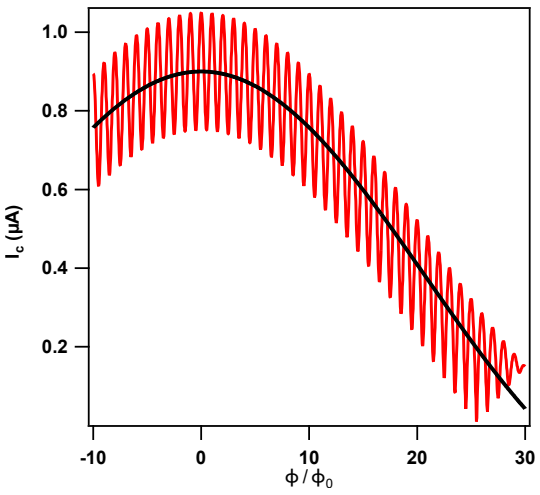

FIGURE 3.16 – Example of a pattern calculated using $I_{ref}(\varphi) = I_{c,ref}\sin(\varphi)$ and a gaussian decay, and the junction "probed" is described by $I_,u(\varphi) = I_{c,u}\sin(\varphi)$ an no decay with field. The example is calculated with $\ddot{I}_{c,ref} = 10 \times I_{c,u}$. The gaussian decay of the reference junction is plotted in black solid lines, whereas the measured pattern is plotted in red.

Now that the principle of the experiment has been explained, the following section is about the fabrication of the asymmetric DC SQUID.

3.4 . Device fabrication

In this part, we describe the fabrication process from exfoliation of the WTe_2 crystals to the superconducting material deposition. We also discuss the SQUID geometry and the choice of the superconducting material.

3.4.1 . Exfoliation and transfer

(a) Exfoliation

The crystals were grown by R. Cava and L. Schoop's group from Princeton University and we follow a process similar to the one presented in S. Wu et. al [64] for the exfoliation. The crystal used in our experiment has a residual-resistance ratio (rrr) of 1000, indicating the good quality of the material. For one sample, two silicon chips (usual undoped Si/SiO_2) were cleaned in ultrasonic baths, first with acetone and then with isopropanol. An optional O_2 plasma cleaining step was performed. The exfoliation takes place in a glovebox filled with argon with a low water and oxygen level (below 1ppm) as WTe_2 thin flakes are very sensitive to air and oxidize easily.

— We use adhesive tape and deposit a needle-shaped crystal of WTe_2 on it. By using a second piece of tape we glue and tear ("exfoliate") the crystal as slowly as possible, from 7 to 10 times, along the direction of the needle.
— The chip on which we deposit the flakes is heated at 90°C five minutes prior to deposition. It eases the peeling step.
— For a better deposition, the tape is gently rubbed with the back of the tweezers.
— The tape is the peeled very slowly (0.5mm/sec)

At this stage, many flakes are visible on the chip, see Fig. 3.17. Because of its crystalline structure, the long edge should correspond to the a-axis. The flake is selected at this stage and we just need to transfer it to a clean substrate for the further steps.

(b) Transfer

We use a standard transfer technique, similar to the one used for graphene, to transfer the flake of interest in a second chip prepared prior to the exfoliation.

To pick up the flakes, we first prepare a glass slide with a polycarbonate (PC) film covering a polydimethylsiloxane (PDMS) cube as illustrated in Fig. 3.18. When the flake is seen through the glass slide under the microscope, we follow this procedure :

— First we touch with the PC film the silicon chip close to the region of the flake of interest.
— We increase the temperature of the stage at 120°C. The contact region spreads and covers the flake due to thermal expansion.

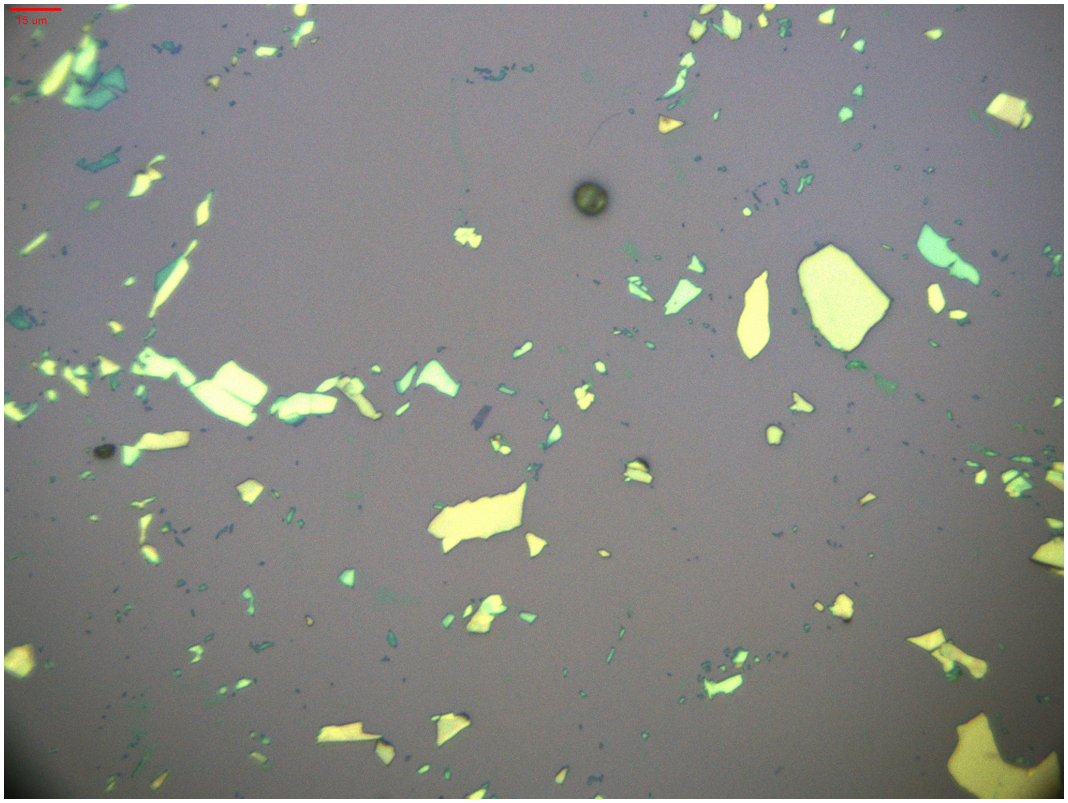

FIGURE 3.17 – Optical image right after the exfoliation step. Scale bar (top left) is 15 µm.

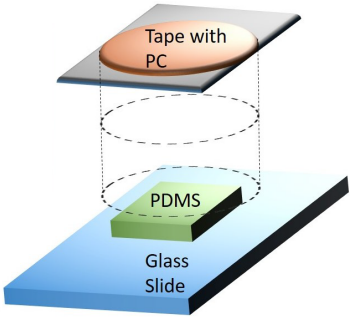

FIGURE 3.18 – Sketch of the transfer "device", constiting of a glass slide, PDMS and PC film. From [86].

— We stop the heating and let the stage cool naturally. The film retracts because of the temperature decrease, and picks up the flake.

The flake is then on the PC film. To drop off the flake on the clean chip :

— When the PC film and the substrate are in contact, we slowly increase the temperature up to 180°C.
— We slowly remove the glass slide.
— At some point, the PC film melts onto the chip. The flake is then on the

clean chip, cover by the PC film.
Due to its rather high thickness, the flake can be exposed to air without destroying it and is not protected with BN. The chip is soaked in chloroform for about 20 minutes to remove the PC film. After the exfoliation, the transfer and the cleaning, we obtain the flake presented in Fig. 3.19.

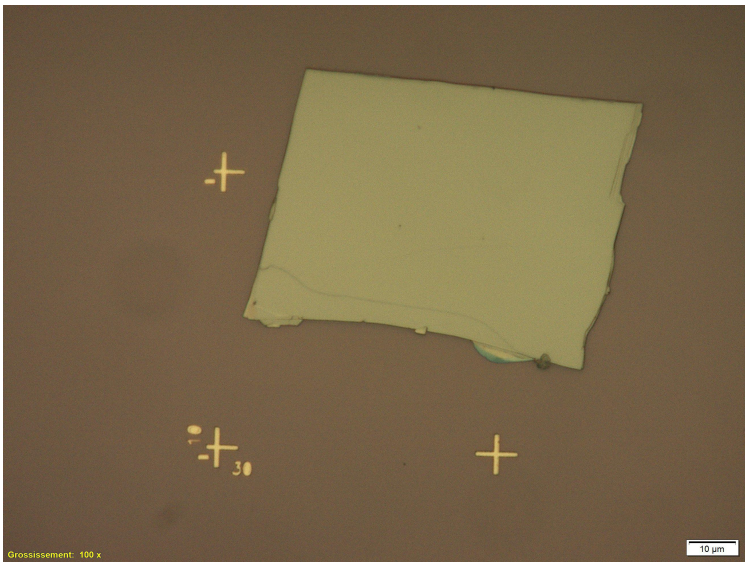

FIGURE 3.19 – Chosen flake after transfer onto a clean chip. It is around 60 μm long along the a-axis and 40 μm long along the b-axis, and 200nm thick (determined by AFM measurements)

.

3.4.2 . Sample design

The idea using a huge flake of WTe_2 is to use the metallic nature of the bulk to build the reference junction at the same time as we fabricate the junction on the edge of the flake. However, we need to make sure that the junction in the bulk will indeed be the junction with the highest critical current. To do so, the simplest way is to minimize the length of the junction. One could also fabricate a wide junction, but it increases the risks of directly connecting the two superconducting banks, creating a shortcut. To solve this problem, we design the junction to have a hourglass shape, for which we expect the most important contribution to come from the shortest part. The superconducting banks are placed not too far in the bulk when connecting the edges to avoid possible contribution from the bulk states. For the loop, since WTe_2's resistance shows a very anisotropic behaviour (the resistance along the b-axis is twice the one along the a-axis according to [78]), the loop is designed with a rectangular shape. Dimensions are chosen such that the period of oscillations should be around $\Delta B \approx 2$ G, accessible experimentally.

The design of the sample and its size scales are sketched in Fig. 3.20. The loop has a surface $S_{loop} = 14.4$ µm^2 and the length of the edge junction is designed to be 500 nm.

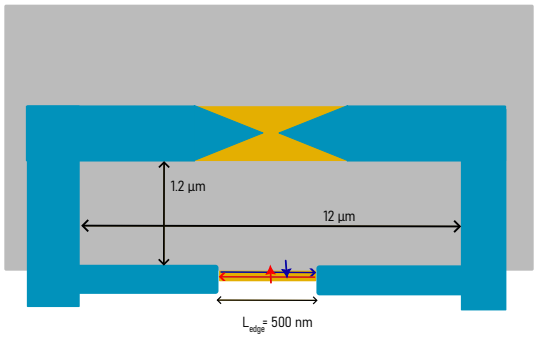

FIGURE 3.20 – Design of the SQUID using the bulk of WTe_2 for the reference junction. In grey the part of the flakes not affected by the superconducting proximity effect. In blue the superconductors and in yellow the normal part of the junctions. The hourglass geometry is the subject of section 3.6.1. The edge junction is 500 nm long, and we represented with the red and blue arrows the helical current expected to flow in this junction.

3.4.3 . Lithography and metal deposition

The lithography process is similar to the one presented in the first part of this manuscript. We use standard electron beam lithography with a chemical semi-amplified positive e-beam resist. The high spatial resolution is important for this sample because of the thin contact between the edges and the superconducting leads. Before the metal deposition, an argon ion-beam etching step of four seconds is performed to remove possible oxide coming from the small amount of time the flake saw air.

A thin film (8 nm) of Palladium is first deposited by sputtering. Palladium diffuses into the flake on a short distance, yielding a $PdTe_x$ alloy which is superconducting hence allowing transparent interface [87]. 80 nm of Niobium are deposited (also by sputtering) directly after the palladium as the superconducting leads. Finally the sample is soaked into 1-3 dioxolane for the lift-off process. A SEM image of the sample is shown in fig 3.21.

3.5 . Measurement techniques.

Once the sample is ready, we place it in a dilution refrigerator at the center of a superconducting magnet. Two techniques are used to measure the interference pattern of the sample.

3.5.1 . Differential resistance

At a fixed **B** field, we measure is the differential resistance of the sample. To do so, the sample is biased with a DC current bias I_{DC} to which a small oscillating current is added i_{ac} at low frequency (a few hundred of Hz at most), represented in Fig. 3.22 : the voltage sources are in series with the two resistances to current bias the sample. We measure the voltage drop v_m across the sample after amplification

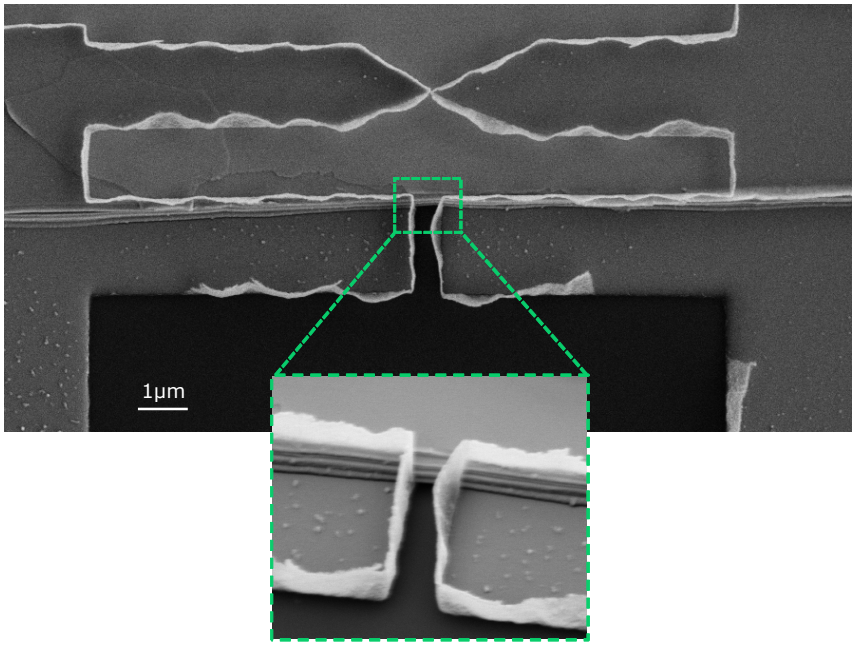

FIGURE 3.21 – Scanning electron microscope image of the considered sample in the following of this manuscript. The bulk junction has hourglass shape to ensure that it carries a higher supercurrent than the edge junction. The green-squared picture is a zoom on the edge junction, showing a few "terraces", of width between 40 nm and 100 nm.

using a lock-in amplifier, yielding $R(i_{dc}) = \frac{v_m}{i_{ac}} \approx \frac{dV}{dI}(I_{dc})$.
Let us assume that we start the current sweep at $I_{DC} = 0$. The sample is superconducting and then the measured v_{ac} is zero. When I_{DC} exceeds the critical current of the SQUID, the SQUID becomes resistive and a finite voltage is measured. The difference between the low bias and high bias region is the normal state resistance of the two junctions in parallel.

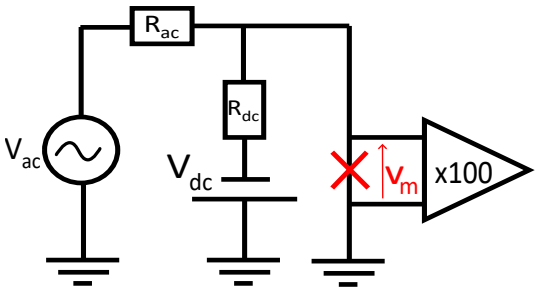

FIGURE 3.22 – Electronic circuit for the standard differential resistance measurement. The measured voltage v_m across the sample can be converted into resistance by the relation $dV/dI = v_m/i_{ac}$.

3.5.2 . Counter technique

The other method consists on measuring the switching current only. [3] rather than the full $dV/dI(I_{DC})$. To do so, the sample is biased with a linearly increasing current (a ramp) of period $1/f$ (with f around 17 Hz in our experiment). When the current reaches the switching current value, the sample becomes non-superconducting and a finite voltage appears. The time Δt between the beginning of the ramp and the superconducting-to-normal transition is measured repeatedly using a counter and the measured time is averaged over a hundred times.

In practice, we use an arbitrary function generator producing a voltage ramp of amplitude V_{pp}, in series with a resistance R_p to produce a current bias that is swept linearly in a period $1/f$. When the maximal voltage is reached, the generator goes back to 0 also linearly but with a faster rate to prevent any damage to the sample. This asymmetry in the ramp is characterized by a skewness parameter (also called duty, between 0 and 1), so that the ramp goes from 0 to V_{pp} in a time skewness$/f$ and from V_{pp} to zero in a time $(1 - \text{skewness})/f$. Time can be converted to the current via 3.12. The offset V_{off} corresponds to I_{min} slightly negative and is chosen to ensure that the measurement starts from the superconducting state of the sample.

$$I_c = \frac{1}{R_p}(V_{off} + \frac{V_{pp}}{\text{skewness}}(\Delta t \times f)) \tag{3.12}$$

The principle of the experiment is presented in Fig. 3.23

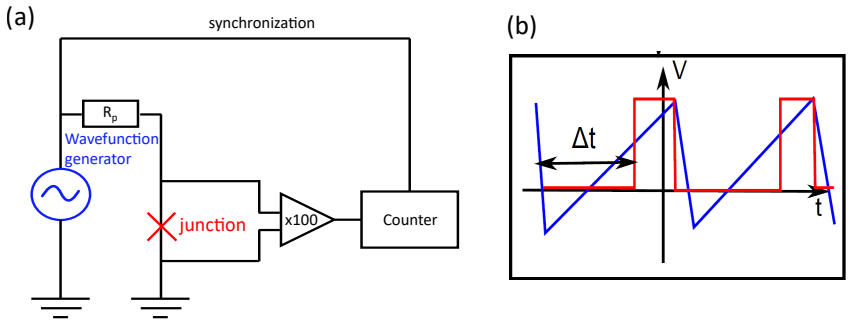

FIGURE 3.23 – (a) Counter technique principle for the measurement of the switching current. (b) Blue : voltage ramp produced by the generator. Red : voltage appearing across the junction when it enters the resistive state. The time difference Δt between the start of the ramp and the voltage jump is measured. Note the asymmetry and the small offset in the ramp.

3.5.3 . Advantages and drawbacks of the two techniques.

The two techniques described above are equivalent for the measurement we want to perform : by measuring the differential resistance we can extract the value of current where the transition occurs, which is directly obtained using the counter technique. The latter is indeed faster : the average time needed for a single point in field is on the order of 10 seconds, whereas the differential resistance measurement takes several minutes per point. However, the counter technique is very dependent

3. In this experiment, we do not measure the exact critical current

on the resistance of the sample considered : the lower the resistance the lower the voltage across the junction hence the measurement becomes harder. Although both techniques have been used for the sample we are studying, we show only the differential resistance measurement in the main part of this manuscript.

3.6 . Current-phase relation of topological hinge states in multilayer tungsten ditelluride

3.6.1 . Characterization of the reference junction.

(a) Conductance model for the hourglass junction

Now that the sample is ready and that we have the techniques to measure the critical current oscillations, we start by confirming that the hourglass-shaped junction is indeed the reference junction. To do so, we start by studying the differential resistance versus dc current ($dV/dI(I_{DC})$) of the whole SQUID. A first result at T = 20 mK and 0 magnetic field is shown in Fig. 3.24.

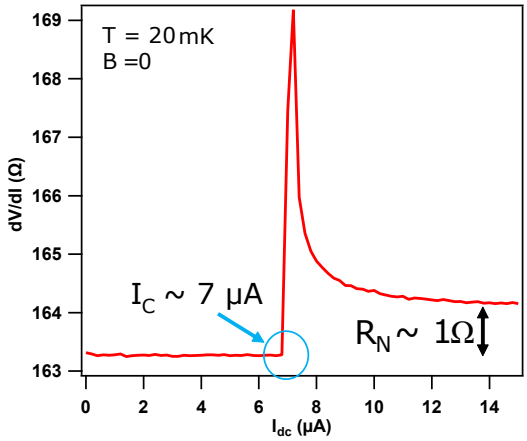

FIGURE 3.24 – Differential resistance curve taken at 0 field and T = 20 mK. The critical current, highlighted by the blue circle, is about 7 µA. The jump in resistance, i.e. the difference between the low bias and high-bias region is the resistance of the sample, about 1 Ω here. The non-zero resistance of 161.3 Ω is due to the filtered dc lines from the room temperature stage of the refrigerator to the sample, visible in the two wires measurement.

The jump of resistance is the equivalent resistance of the two junctions in parallel. We argue that this resistance is dominated by the bulk junction :

$$\begin{aligned} \frac{1}{R_{tot}} &= \frac{1}{R_{bulk}} + \frac{1}{R_{edge}} \text{where edge/bulk stands for their respective junctions} \\ &\propto L_{bulk}^{-1} + L_{edge}^{-1} \end{aligned} \tag{3.13}$$

with $L_{bulk/edge}$ the lengths of the junctions. The smallest length in the SQUID is the "crossing" point of the hourglass, hence it is the part that contributes the most

to the resistance. To further elaborate this statement, we consider the hourglass junction only, illustrated in Fig. 3.25 with the relevant parameters : $y_{max} = 0.73$ µm, $l_z = 200$ nm is the thickness of the flake, and $d = 2.21$ µm the length of the diagonal of the hourglass (used to calculate the angle), $l(y_{max}) = 2.06$ µm.

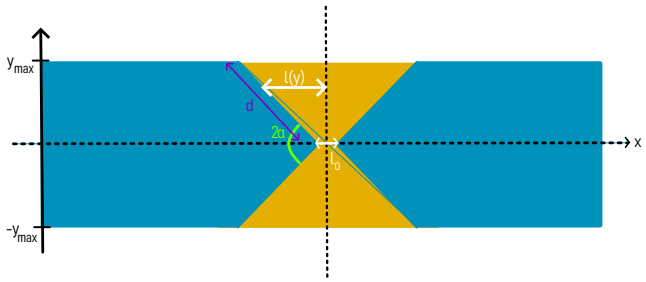

FIGURE 3.25 – Sketch of the hourglass-shaped junction with relevant parameters. The colored part represents the superconducting leads and we wish to determine the conductance of the white part. $y_{max} = 0.73$ µm, $d = 2.21$ µm. $l_z = 200$ nm the thickness of the flake, and $l(y_{max}) = 2.06$ µm are not written in the sketch for clarity.

We assume the junction to be symmetric and for the calculations we can only consider the top triangular shape (half of the hourglass) starting at $y = 0$ up to $y = y_{max}$. We define an elementary conductance $g(y)$ as :

$$g(y) = \sigma \frac{S}{2l(y) + l_0} \tag{3.14}$$

with $S = t \times dy$ and $\sigma = 2$ MS/m the conductivity. The angle α is defined as :

$$\tan(\alpha) = \frac{y}{l(y)} \tag{3.15}$$

which can be computed and we have $\tan(\alpha) = 0.35$. This allows to write the elementary conductance :

$$g(y) = \frac{\sigma t dy}{2\frac{y}{\tan(\alpha)} + l_0} \tag{3.16}$$

so that the total conductance of the junction is :

$$\begin{aligned} G &= 2 \times \int_0^{y_{max}} \frac{\sigma t}{2y/\tan(\alpha) + l_0} dy \\ &= \sigma t \tan(\alpha) \ln(\frac{2y_{max}}{\tan(\alpha) l_0} + 1) \end{aligned} \tag{3.17}$$

Quantitatively, we obtain :

$$R = \frac{1}{G} = 1 - 1.5\Omega \text{ similar to the experiment} \tag{3.18}$$

With the expression of G obtained in equation 3.17, we can compute an effective length for the hourglass junction using

$$G = \frac{\sigma S}{L_{eff}} \tag{3.19}$$

with

$$\begin{aligned} L_{eff} &= \frac{2y_{max}}{\ln(\frac{2y_{max}}{l_0 \tan(\alpha)+1})} \times \frac{1}{\tan(\alpha)} \\ &= 0.94 \text{ µm} \end{aligned} \tag{3.20}$$

and the hourglass junction is equivalent, as a first approximation, to a rectangular junction of width $w = 2y_{max}$ and length L_{eff}, as illustrated in Fig. 3.26

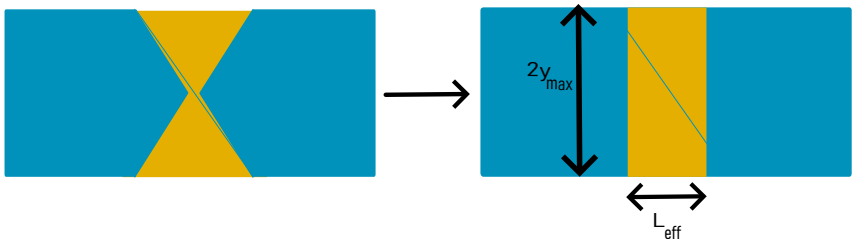

FIGURE 3.26 – The hourglass junction, in the following of the characterization, will be seen as its equivalent rectangular junction of width $w = 2y_{max}$ and length L_{eff}, much simpler to study.

This L_{eff} will be used in the next parts to compute the Thouless energy and the aspect ratio of the equivalent rectangular junction.

(b) Temperature dependence of the reference junction

Let us take a look now at the temperature dependence. The differential resistance curve presented in Fig. 3.24 is recorded at different temperatures and we observe a decrease in the critical current, and the variation with temperature is presented in Fig. 3.27. The decrease is fitted with the exponential decrease of a diffusive junction (similar to the fit presented in Fig. 2.16 of chapter 2, from [19]), yielding a Thouless energy $E_{Th} = 68$ mK

This result is further corroborated by the rectangular junction approximation for which we can compute the Thouless energy as :

$$\begin{aligned} E_{Th} &= \frac{\hbar D}{L_{eff}^2} \\ &= \frac{\hbar v_F l_e}{3L_{eff}^2} \\ &\approx 40 \text{ mK} \end{aligned} \tag{3.21}$$

giving a similar order of magnitude. It confirms the diffusive nature of transport in the hourglass-shaped junction.

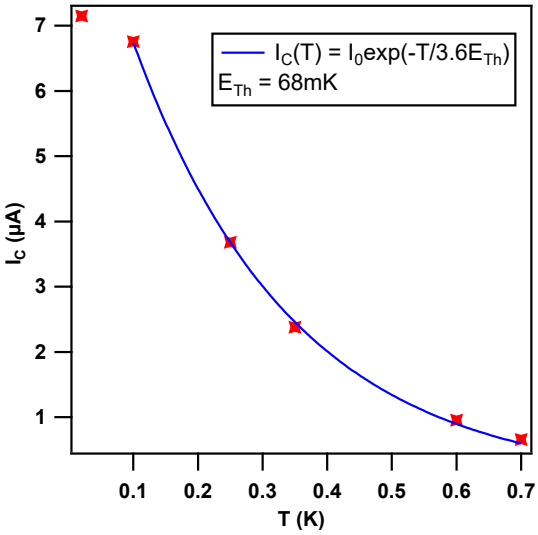

FIGURE 3.27 – Temperature dependence of the critical current at B = 0 measured using the differential resistance method. The fit using the exponential law for a diffusive junction yields $E_{Th} = 68$ mK.

(c) Diffraction pattern of the reference junction

We have seen in section 3.3.2 that a long diffusive SNS junction under a magnetic field could yield a diffraction pattern whose shape depends strongly on the aspect ratio W/L. We perform the differential resistance measurement at various fields, and the result is shown in Fig. 3.28

The frontier between the black and red regions in this figure represents the SQUID's critical current evolution with the magnetic field. It can be separated into two components : one huge background, decreasing quickly with the magnetic field, and a modulation which should be the CPR of the edge junction and is the subject of section 3.6.2. The background seems to rebound at 10 mT, 15 mT and 20 mT. This is reminescent of a Fraunhofer-like interference pattern, that we characterize by calculating the effective aspect ratio of the hourglass-junction using :

$$\frac{w}{L_{eff}} = \frac{2y_{max}}{L_{eff}} \approx 1.5 \tag{3.22}$$

Due to this aspect ratio and the hourglass geometry, the diffraction pattern we observe can not be fitted to the usual Fraunhofer function of eq. 3.10, as it seems closer to the case $L = 10\xi$ in Fig. 3.15(a), and yet it is still a rough approximation. It is important to notice that we don't have any analytical expression for this field dependence in our geometry, and we can only describe it with the previous qualitative arguments.

In conclusion we approximate the reference junction as a diffusive long junction of rectangular shape with an effective aspect ratio of 1.5, explaining the slow variations of 3.28. In the following, we focus on the edge junction, which is expected to carry the signatures of the topological hinge states.

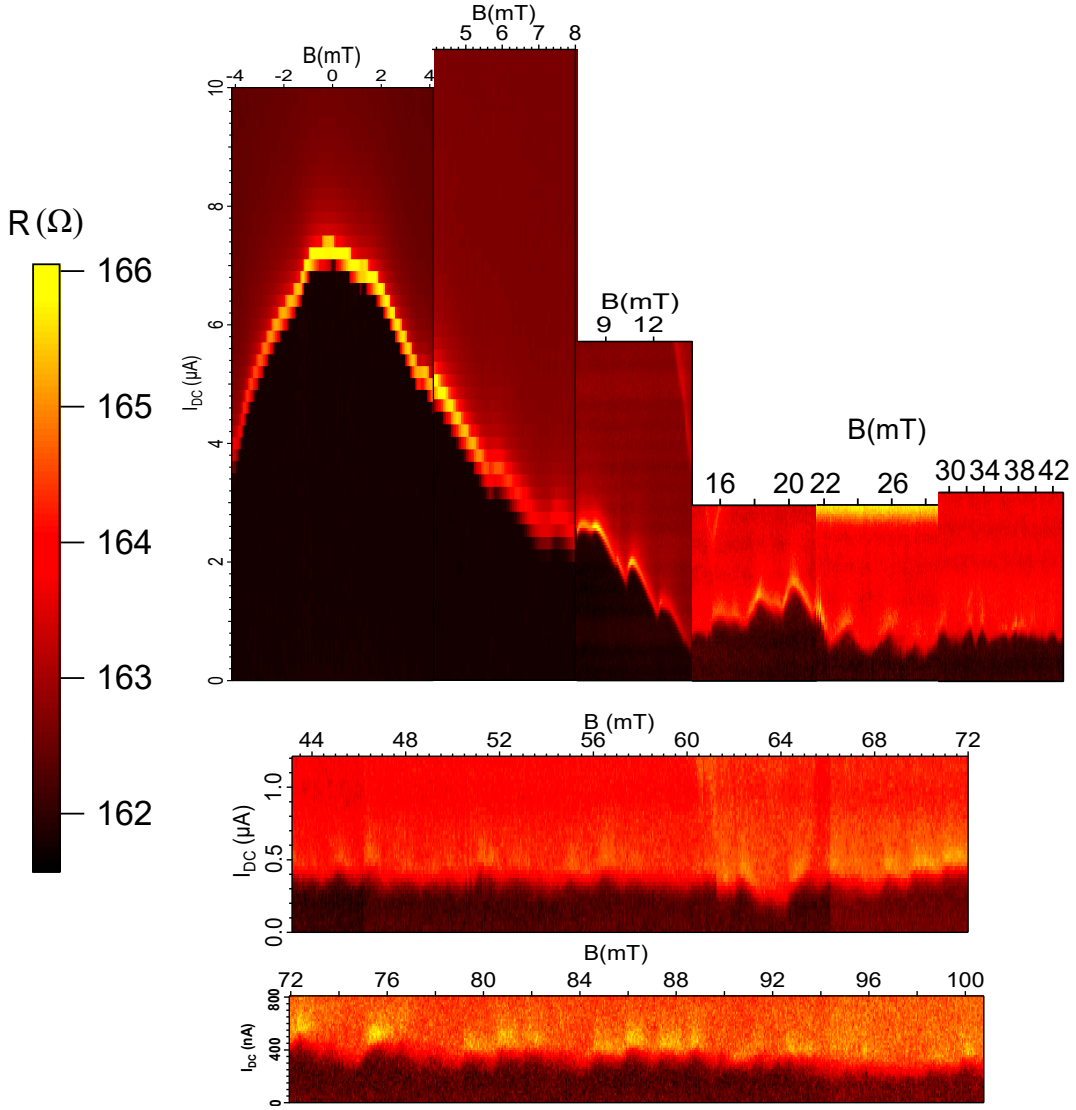

FIGURE 3.28 – Differential resistance vs external applied field, between -4 mT and 100 mT. The y-axis represents the dc current flowing through the sample, the x-axis the field. The color represents the resistance of the junction : it switches from a superconducting state (black) to a resistive state (red) when the dc current reached the critical current of the SQUID. The envelop represented by the yellow interface between the black and red curve (when it is well defined, mostly at low field) represents the behaviour of the critical current with the magnetic field. This pattern is obtained at T = 20 mK.

3.6.2 . Current-phase relation of the edge junction

(a) Parallel and effective field

Let us first describe the orientation of the magnetic field with respect to the SQUID. The magnetic field is mainly oriented parallel to the plane of the SQUID, but because the sample is slightly tilted there is a small component perpendicular

to the SQUID that allows us to measure the interferences in the device.

To observe the modulation of the critical current of the SQUID over a period of the CPR, one should thread a quantum of flux $\Phi_0 = \frac{h}{2e}$ through the surface of the SQUID.

The experimentally period is 2.3 mT, and it corresponds to an expected period of 0.13 mT (from $\Delta B = \Phi_0/S$, with $S = 14.4\ \mu\text{m}^2$). This means that the perpendicular component of the field is 6% of the applied field only, and most of the applied field is parallel to the plane defined by the SQUID.

The orientation of the field with respect to the sample is sketched in Fig. 3.29

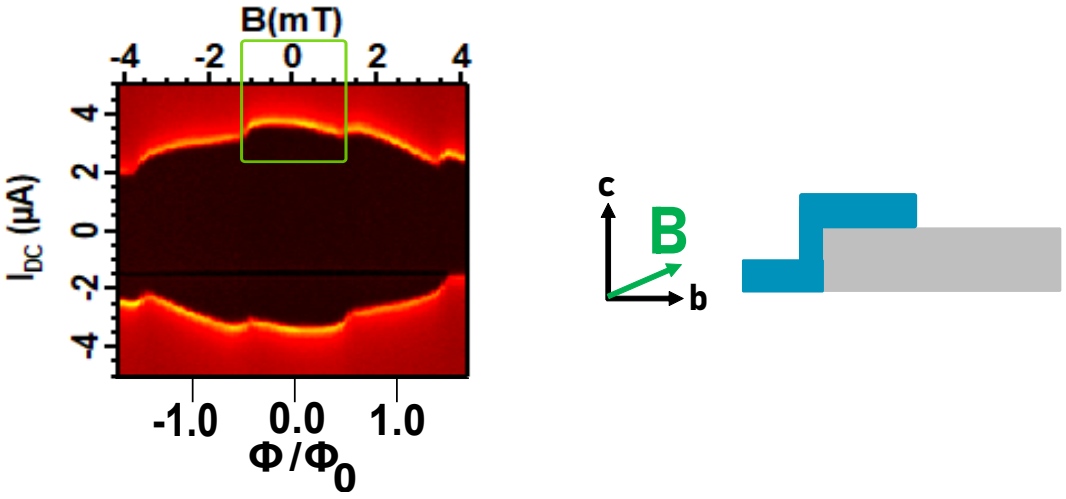

FIGURE 3.29 – (Left) From the background, a modulation of period 2.3 mT can be seen. Since we attributed the background behaviour to the reference junction, this period in magnetic field is associated with the SQUID area of 14.4 μm^2, i.e. 0.13 mT, meaning that only 6% of the applied field is perpendicular to the SQUID. The bottom axis represents the flux going through the SQUID. (Right) Exaggerated orientation of the magnetic field on the (b,c) plane. The real field is even closer to the b-axis.

(b) Extraction of the CPR and low field behaviour

We now discuss the modulation seen on top of the huge diffraction pattern. The modulation is clearly seen in a range of -4 mT and 4 mT and therefore we focus first on this range of field. The results at T = 250, 350, 600 and 700 mK are plotted in Fig. 3.30.

The first step is to extract the critical current of the SQUID. To do so, we need a proper definition of the supercurrent. We choose to take the current associated with the mean value of the jump of resistance : if the system has a finite resistance R_s in the superconducting region and R_r in the resistive state, the current associated to $(R_r + R_s)/2$ is taken as the critical current [4]. The extraction of the critical current

4. The non-zero resistance of the superconducting state is not observed due to the filtered

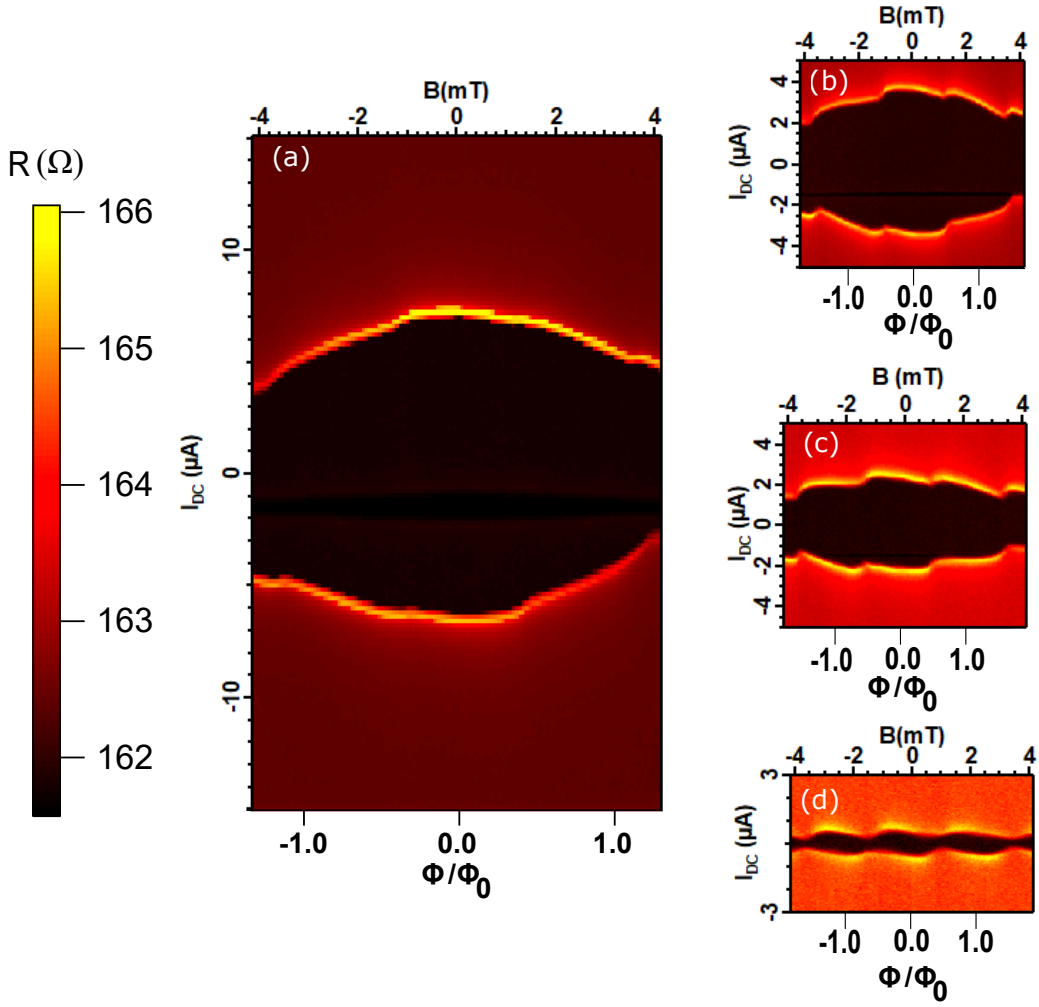

FIGURE 3.30 – Interference pattern at **(a)** T = 20 mK**(b)** T = 250 mK **(c)** T = 350 mK**(d)** T = 700 mK, with a field between -4 and 4mT only. The black region is the superconducting state and the red region is the resistive state. The critical current lies between the black and red regions. The decrease in the critical current is clearly visible and is attributed to the reference junction as argued in section 3.6.1. A first step in the analysis is to extract the critical current of the SQUID.

is illustrated in the differential measurement curve of Fig. 3.31(a). By doing so at every point in field, we can extract the $I_c(B)$ dependence of the SQUID, and rebuild the envelop of the interference pattern, see 3.31(b).

The critical current versus field low for T = 250 to 700 mK is shown in Fig. 3.32. The extracted signal already shows a ressemblance with a sawtooth, especially at higher temperature when the effect of the diffraction is reduced.

The extraction of the critical current is however not sufficient to analyze quantitatively the CPR and we need to remove the diffraction pattern. Since there is no

DC lines from the room temperature stage of the refrigerator and the sample which are observed in a two wires measurement

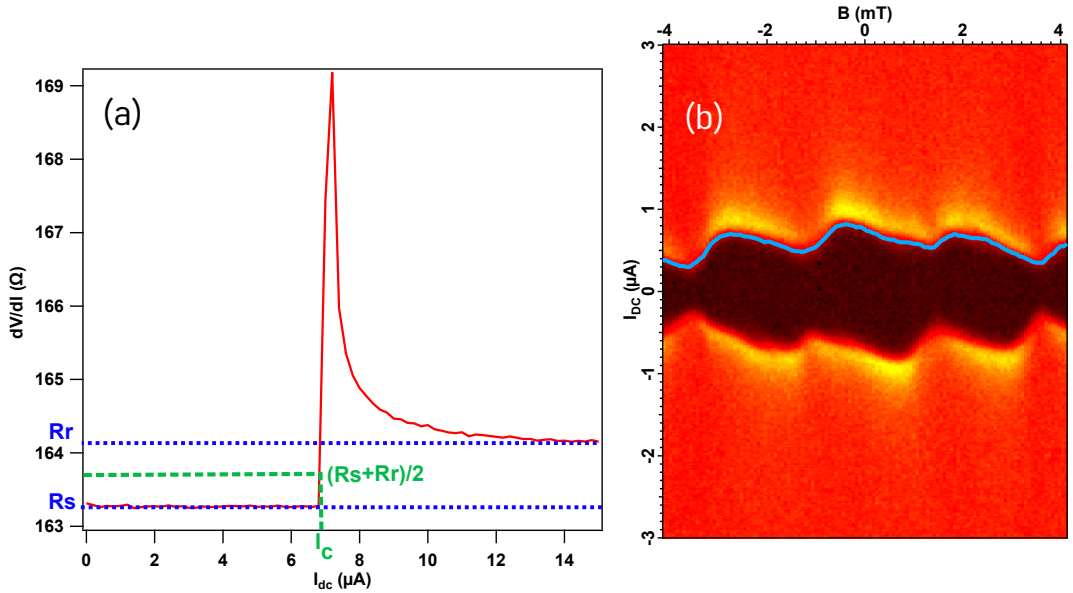

FIGURE 3.31 – (a) The critical current is defined here as the value associated with the jump in resistance : if R_s is the resistance in the superconducting state (low current bias region) and R_r in the resistive state (high bias region), we necessarily have a current value associated to $(R_r + R_s)/2$. This point is taken at every field, and we obtain the result of (b) the $I_c(B)$ law is extracted, represented by the blue solid lines.

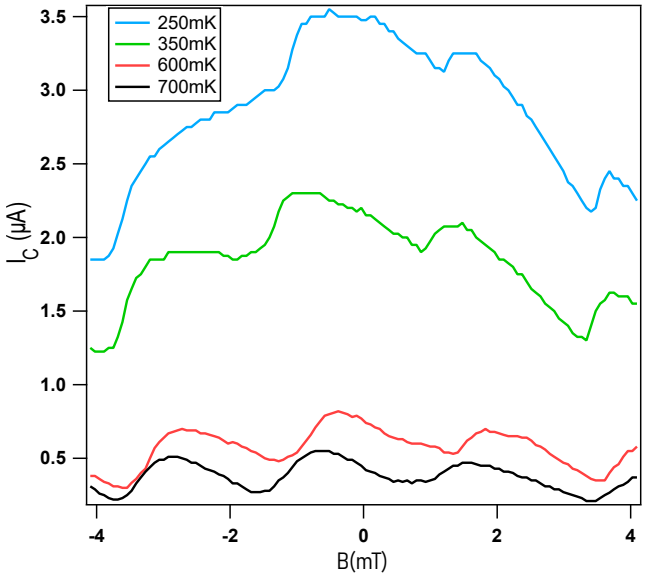

FIGURE 3.32 – $I_c(B)$ extracted for T = 250, 350, 600 and 700 mK. We see that, as the temperature increases, the diffraction effect on the reference junction is reduced and at 600 and 700 mK a sawtooth-like shape is already visible.

analytical expression, we filter the signal numerically. The Fourier transform of each interference pattern is calculated. The diffraction effect can be associated with the

low frequencies of the Fourier decomposition, and removing the first three harmonics we can extract the modulation only. An exemple of this low-frequency cut is shown Fig. 3.33 together with all the extracted current-phase relations. The amplitude of these CPRs doesn't seem to change with temperature and stays at around 150 nA for the range of temperature we investigated, but it seems more rounded as the temperature increases than the long ballistic CPR expected for a topological edge channel.

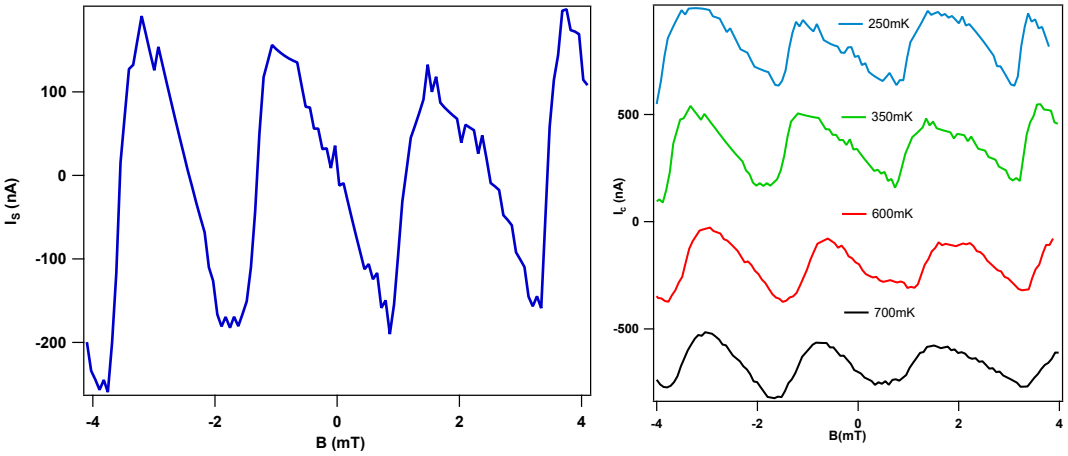

FIGURE 3.33 – (Left) The low-frequency cut applied at T = 350 mK as an example. Using this method, we obtain the CPR centered around 0 and the critical current can be read directly from the curve, yielding $I_c \approx 150$ nA. (Right) Results for T = 250, 350, 600 and 700 mK. The curves are offset for clarity. The sawtooth shape seems more rounded at higher temperature.

We distinguish two possibilities to explain the roundness of the CPR :

— A non-perfect interface yields change in the energy spectrum of the Andreev states, even in the case of a TI/S interface. The critical current of a S/TI/S junction decreases even if the jump remains abrupt at phase π. [88, 89].

— Temperature might reduce the importance of the highest harmonics first. When reaching high enough temperature (for instance, E_{Th}), the CPR might gets closer to a sine.

To take into account these effects, we introduce a term e^{-an}/n in the Fourier decomposition of the sawtooth, such that it reads :

$$I_{saw}(\varphi) = I_c \sum_n \frac{e^{-an}}{n} \sin(n\varphi) \tag{3.23}$$

such that it places the decomposition in between the two extreme cases of a perfect ballistic transport (where the amplitude of the harmonics is proportional to $1/n$) and diffusive transport (for which they decrease as $1/n^2$). The Fourier decomposition (see Fig. 3.34(a)) can thus be fitted to $\exp(-an)/n$ with respect to n, as shown in Fig. 3.34(b).

This damping term a is a general term describing the non-perfect ballistic nature of the transport. To take into account this effect, we expand the definition of a by

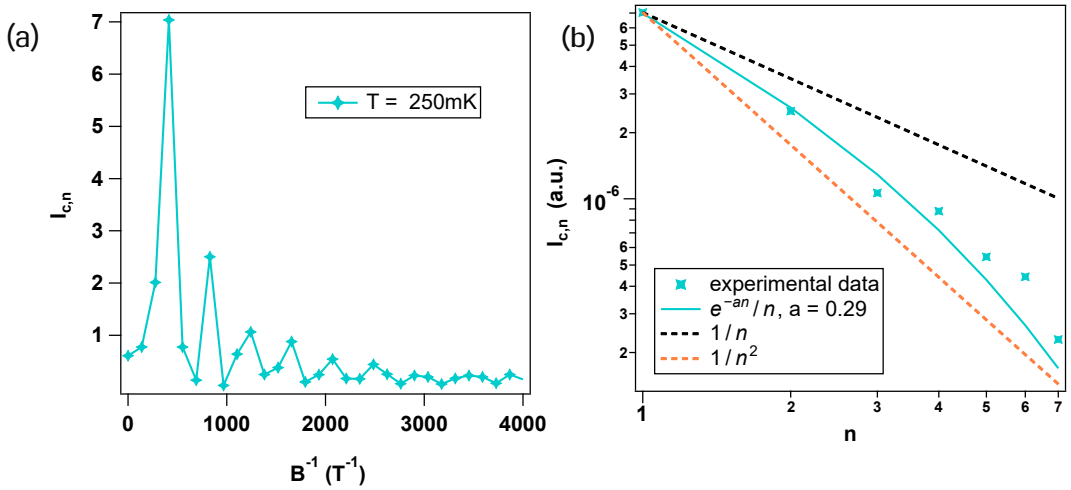

FIGURE 3.34 – (a) FFT performed on the sawtooth obtained for T = 250 mK. The seven first harmonics are used for the fit using equation 3.23. (b) Fit of the amplitude of the harmonics. We obtain $a = 0.29$. The $1/n$ (black dashed lines) and $1/n^2$ (orange dashed lines) behaviours are plotted to show that the actual dependence on n lies in between, indicating the non perfect ballistic nature of the hinge states.

the relation :

$$e^{-an} = t^n e^{-nT/E_{Th}} \tag{3.24}$$

$$\rightarrow a = -\ln(t) + \frac{T}{E_{Th}} \tag{3.25}$$

from [25], where t is the transmission in the normal part of the junction, representing a finite coherence length for instance, assumed to be temperature independent. A linear fit using equation 3.25 is thus performed in order to obtain the Fourier decomposition of the CPR, see Fig. 3.35

Nevertheless, these results are to be taken carefully as it can be seen from the error bars especially at T = 700 mK. However the order of magnitudes tend to favor an interpretation in terms of topological hinge states :

— The sawtooth-like CPR points to ballistic transport, over more than 500 nm.

— $E_{Th} = 1.39$ K $< \Delta \approx 5$ K indicates the long junction regime.

We can compare with the expected values for the Thouless energy and the critical current. In the ballistic regime, the Thouless energy is defined in equation 1.61. With v_F between 1×10^5 m/s and 3×10^5 m/s [59, 90], we get :

$$1.4 \text{ K} < E_{Th}^{edge} < 4.2 \text{ K} \tag{3.26}$$

and the experimental value is within this range. Following [58], we can compute the current carried by one conducting channel i_{ch} :

$$\begin{aligned} i_{ch} &= \frac{eE_{Th}}{\hbar} \\ &\approx 30 \text{ nA} \end{aligned} \tag{3.27}$$

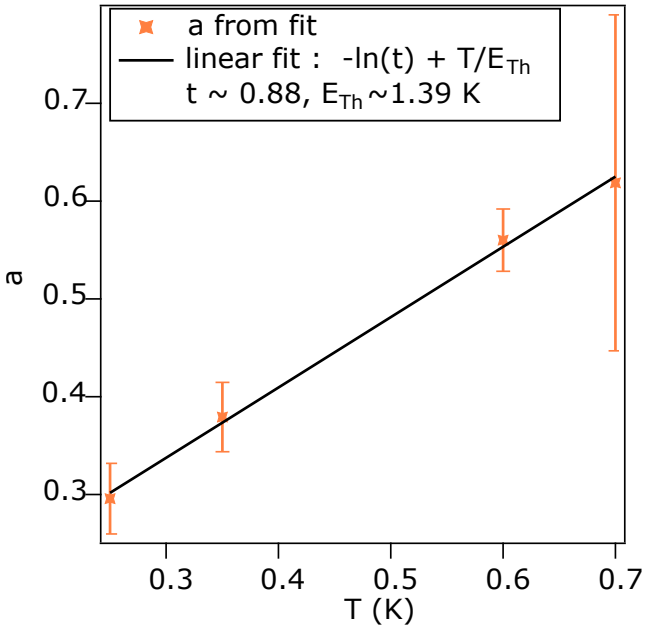

FIGURE 3.35 – damping term versus T. The linear fit performed yields $t \approx 0.88 \pm 0.01$ and $E_{Th} = 1.39 \pm 0.05$ K

In a very simple approximation, the number of conducting channels is given by the measured critical current divided by this value. Experimentally it yields $160/30 \approx 5$ conducting channels.

If we replace $i_{ch} = eE_{Th}/\hbar$ by ev_F/L and take the values found in literature, one gets N = 2-6 depending on the values of v_F taken. This is consistent with the SEM image of the sample shown in Fig. 3.21 in which we see 4 terrasses (equivalently 4 topological hinges) but also with the localization of the edge states calculated in [78] and the theoretical aspects depicted [91], illustrated in Fig. 3.36

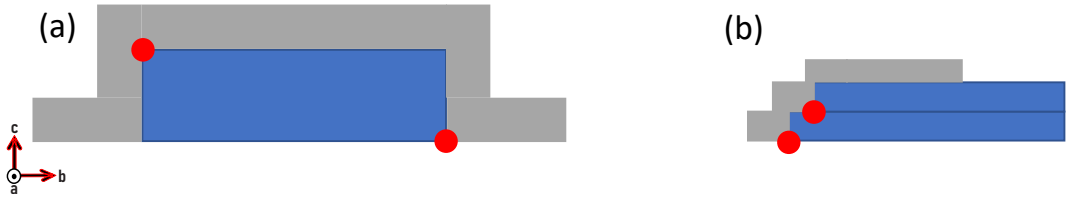

FIGURE 3.36 – **(a)** One out of two hinges is topological in a perfectly rectangular sample. **(b)** In our sample, several terraces can be seen in the SEM pictures. A possible interpretation is depicted in this sketch. The topological hinge states are marked by red dots, the flake is in blue and the superconducting leads in grey.

Knowing E_{Th} and t and fixing them, we can rebuild the CPR calculation using the following equation :

$$i(\varphi) = I_c \sum_n \frac{(-1)^n}{n} t^n \times \mathrm{e}^{-\frac{nT}{E_{Th}}} \sin(n\varphi) \tag{3.28}$$

where the case $t = 1$ and $E_{Th} \gg T$ represents the perfect sawtooth-shaped CPR of the long ballistic channel. The results in comparison with the four experimental points presented is shown in Fig. 3.37

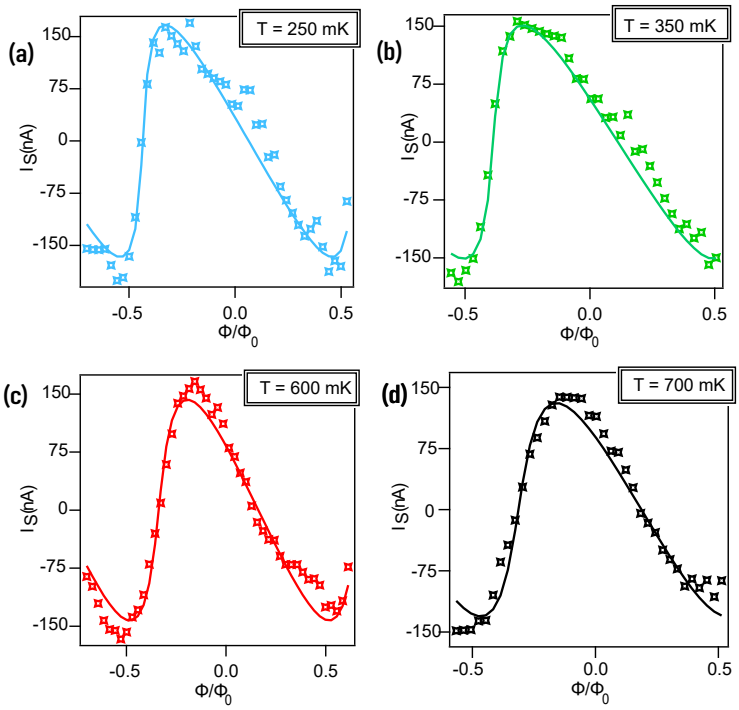

FIGURE 3.37 – Calculated CPR with equation 3.28 (solid lines). The experimental data are the unfilled diamonds. **(a)** T = 250 mK, **(b)** T = 350 mK, **(c)** T = 600 mK, **(d)** T = 700 mK.

3.6.3 . High field behaviour.

The high field behaviour of the supercurrent can give as well some insights about the topological protection. For topologically protected states in multilayer WTe_2 a superconducting behaviour was still observed up to 1 T [78, 79, 80]. On Fig. 3.38 is shown the magnetic field dependence of the supercurrent over a large range of magnetic field, at T = 19 mK and T = 490 mK.

From this measurement we distinguish three zones :

— The first one where the modulation by the sawtooth is clearly visible. (green rectangle)

— The sawtooth disappears and the shape of modulation is less clear. (blue rectangle)

— There is no modulation anymore but quasi constant supercurrent with critical value $\sim$ 150 nA. (yellow rectangle)

The first zone is the one where the asymmetric SQUID regime takes places and we detailed the results in the previous sections. In the intermediate regime and because of the exponentiel decrease of the critical current in the diffusive regime, both junctions have similar critical current values, hence the SQUID becomes sym-

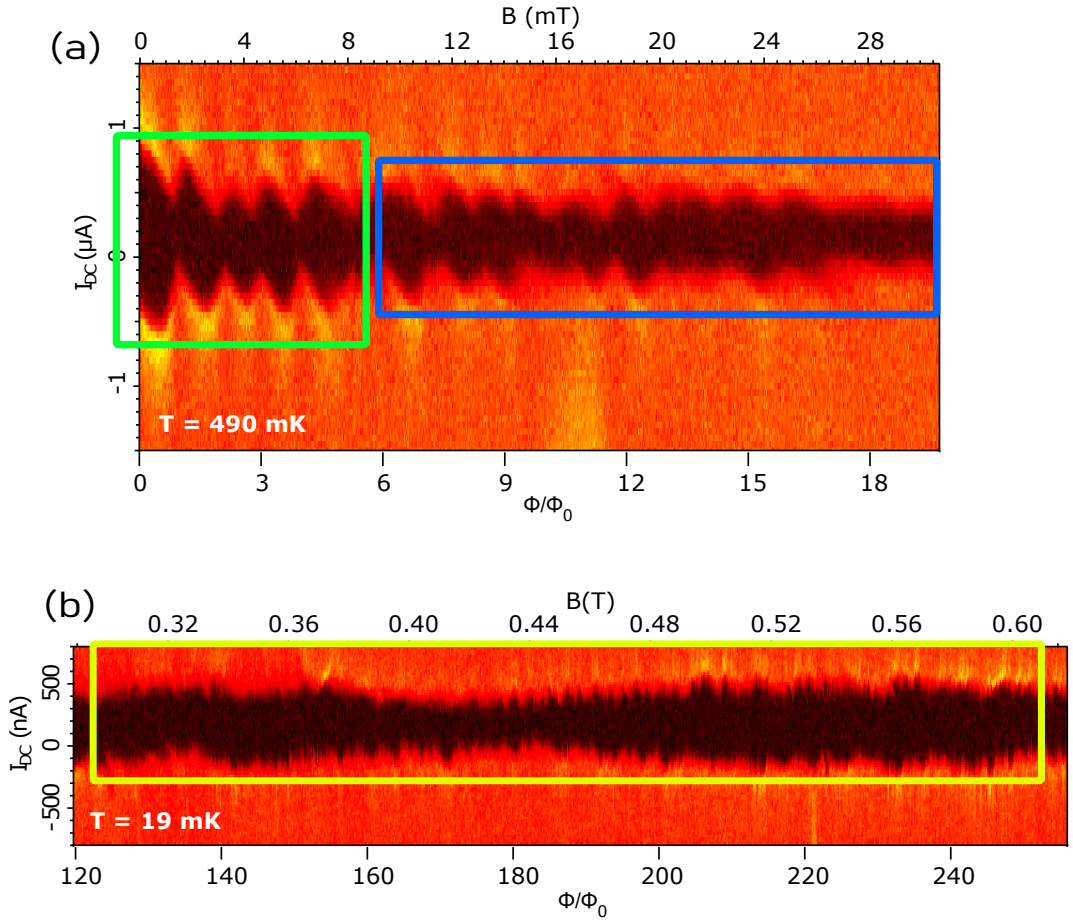

FIGURE 3.38 – Interference pattern at **(a)** T = 490 mK, up to $\approx 20 \times \Phi_0$. **(b)** T = 19 mK, up to $\approx 250 \times \Phi_0$. The green rectangle highlights the zone where the modulation is a sawtooth, the blue rectangle the zone where the modulation is less clear and the last zone where the critical current is almost constant, being modulated in a higher range of field.

metric but with one sine-like CPR and the other one with a sawtooth-like CPR. At high field, the critical current of the diffusive junction is negligible and only the supercurrent carried by the topological hinge states survives with the amplitude of the CPR extracted previously.

We corroborate the behaviour of the interference pattern with numerical calculations on Fig. 3.39. We can tune the calculations by chosing for each junction the critical current, their respective CPR and their dependence in magnetic field. To reproduce the experimental data of Fig. 3.38, we chose :

— For the reference junction : $I(\varphi) = I_{c,ref} \times \sin(\varphi)$, $I_c = 1$ μA and the field dependence is approximated by the Fraunhofer function $I_c(B) = I_c|\,\mathrm{sinc}(B \times S/\phi_0)|$, with S four times smaller than the SQUID area.

— for the edge junction : the CPR is a sawtooth, with $I_c = 150$ nA and no dependence in magnetic field.

An other possibility is that the helical channels interfere with each other. In

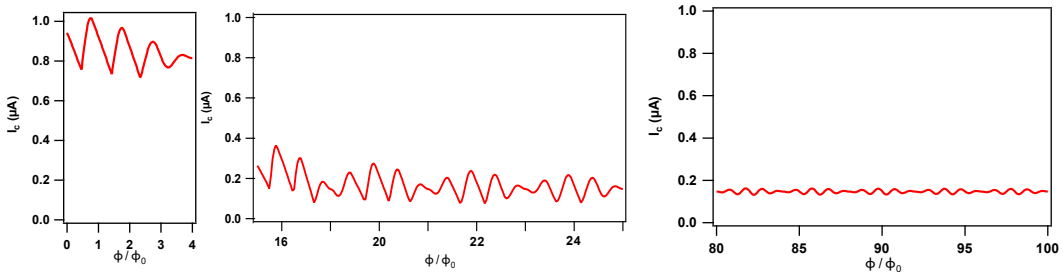

FIGURE 3.39 – Numerical modelisation of the interference pattern. (Left) Region where the sawtooth is clearly visible. (Middle) Modulation of the critical current when the two junctions have a similar critical current. (c) The roughly B-independent critical current. The three graphs are represented at the same scale for ease of the comparison with the experiment.

the case of two channels, we would recover the situation illustrated in Fig. 3.40 as the channels would be symmetric, and their orientation is quasi-perpendicular to the field (see Fig. 3.29 and Fig. 3.36). Additionnally, the Zeeman dephasing could be at the origin of the amplitude and phase modulation we observed for very high Φ/Φ_0, but more experiments are necessary to evidence this effect and is still subject to investigation.

If we assume now that we have two (long) ballistic channels localized at different hinges of the normal part of the junction. In this case, the current distribution can be written :

$$j(y) \propto \frac{1}{2}[\delta(y - y_1/2) + \delta(y + y_2/2)] \tag{3.29}$$

with y_1 and y_2 the positions on the y-axis of the two conducting channels. In the symmetric case, that is to say if $I_{c,1} = I_{c,2}$, this would correspond to a triangular shape interference pattern as in Fig. 3.40. Two main properties emerge from this pattern :

— The critical current never goes to zero.

— In the symmetric case, the triangle oscillates from i_c to $2i_c$.

This interference pattern can also be modified by the addition of an other dephasing term, call the Zeeman term, defined for a junction with two helical pairs of opposite helicities. This Zeeman dephasing reads :

$$\varphi_Z = \varphi_1 - \varphi_2 \approx (\frac{L_1}{\hbar v_{F,1}} g_1 \cos(\theta_1) - \frac{L_2}{\hbar v_{F,2}} g_2 \cos(\theta_2))\mu_B B \tag{3.30}$$

with L_i, $v_{F,i}$ and g_i the lengths, Fermi velocities and g factors of the respectives channels. An interference pattern between two long ballistic channels is shown in Fig. 3.41.

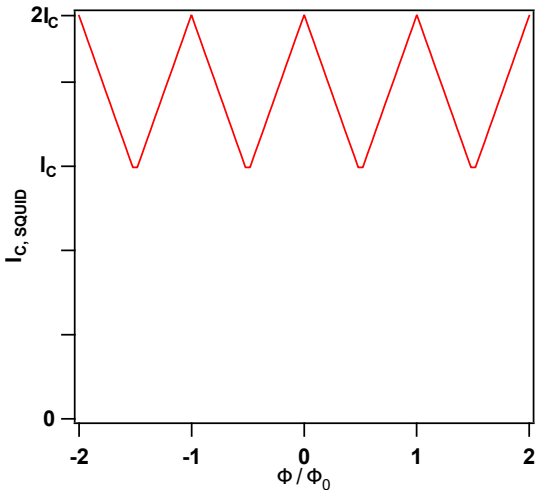

FIGURE 3.40 – Interference pattern obtained for two long ballistic states at the edges of a junction with the same critical current i_c. One notices that the critical current never goes to zero in this case and oscillates between i_c and $2i_c$.

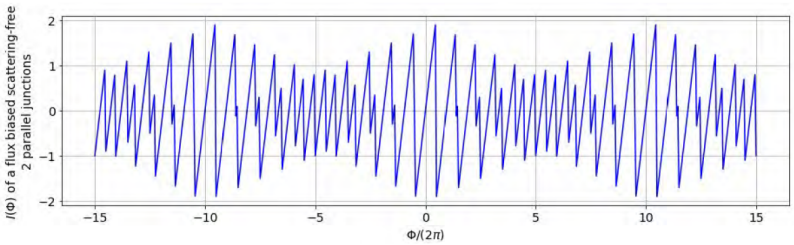

FIGURE 3.41 – DC symmetric SQUID interference pattern with a Zeeman dephasing term taken into account, for two long ballistic channels. From [92].

3.7 . Conclusion and perspectives.

We have measured the current-phase relation of a WTe_2-based Josephson junction (a Weyl semimetal in bulk) by using an asymmetric SQUID. For a junction made from the edge of a multilayer flake along the a-axis, we have detected a clear sawtooth behavior up to high magnetic field. This can be interpreted as the presence of ballistic helical hinge states over 500 nanometers. This is in agreement with the prediction that bulk WTe_2 could present such 1d hinge states as vestiges of a HOTI phase very close in the parameter space. [75]

This work opens the way to further investigations on topological physics using WTe_2. A first measurement that could be performed using the DC SQUID measurement on two opposites hinges could lead to measure the phase shift due to the coupling between the spins and a Zeeman field, yielding the spin-dependence on transport. For other signatures, experiments similar to the ones presented in [93] should reveal the existence of the loop currents along the hinges of WTe_2, in both the normal and the superconducting states. Obviously, as it is proposed in the first chapter, WTe_2 could be used as a material for measurement of the thermal noise

of a topological SNS junction [40, 94], or to observe the effect of a high-frequency irradiation on topological systems [95].

Conclusion

We have demonstrated that a current flowing through an SNS junction is actually noisy, i.e presents thermal fluctuations at equilibrium. This has been done by designing a high frequency set-up based on a ultrasensitive cryogenic amplifier, which allowed us to detect independently the conductance and the noise of the junction. The careful comparison between these two quantities yields a first experimental demonstration of the FDT in an SNS junction. This result shows that supercurrent noise is a fundamental tool to probe mesoscopic systems. Indeed, although FDT tells us that conductance and noise yields the same information, they are not equivalent experimentally. Equilibrium noise measurements, although more challenging, provide a unique advantage over other measurements that involve sample biasing. Indeed, in some cases the linear regime can not be maintained over the full current versus phase relation. This is especially true in the context of topological materials, whose Andreev spectra display true crossings at π, and for which Zener transitions can occur. A true equilibrium measurement, with no excitation, has a clear advantage in this case. In addition, we gave a first theoretical insight to the temperature dependence of the conductance of an SNS junction, highlighting the role of the electron-hole symmetry imposed by the superconductor. [96]

In a second part, we have measured the current-phase relation of a WTe_2-based Josephson junction (a Weyl semimetal in bulk) by using an asymmetric SQUID. For a junction made from the edge of a multilayer flake along the a-axis, we have detected a clear sawtooth behavior up to high magnetic field. This can be interpreted as the presence of ballistic helical hinge states over 500 nanometers. This is in agreement with the prediction that bulk WTe_2 could present such 1d hinge states as vestiges of a HOTI phase very close in the parameter space. [75]

A perspective of this work is to measure the current fluctuations in a topological insulator. A clear signature of the topological protection, which yields a true crossing of ABS at phase π is expected in dissipation and more directly in the equilibrium noise [40, 94]. This crossing should manifest through strong current fluctuations that we plan to measure at finite frequency and ultimately in the time domain. This could be done with monolayer WTe_2 or $BiBr_4$ another HOTI candidate studied in the group.

Bibliography

[1] R. Landauer. « Spatial variation of currents and fields due to localized scatterers in metallic conduction ». In: *IBM J. Res. Develop.* 1.3 (1957), pp. 223–231. DOI: 10.1147/rd.130223.

[2] Christophe Texier. URL: http://lptms.u-psud.fr/christophe_texier/.

[3] Tero T. Heikkilä. *The Physics of Nanoelectronics: Transport and Fluctuation Phenomena at Low Temperatures*. en. Oxford University Press, Jan. 2013. ISBN: 978-0-19-959244-9. DOI: 10.1093/acprof:oso/9780199592449.001.0001. URL: https://academic.oup.com/book/11132.

[4] Eric Akkermans and Gilles Montambaux. *Mesoscopic Physics of Electrons and Photons*. Cambridge University Press, 2007. DOI: 10.1017/CBO9780511618833.

[5] Nandini Trivedi and Dana A. Browne. « Mesoscopic ring in a magnetic field: Reactive and dissipative response ». en. In: *Phys. Rev. B* 38.14 (Nov. 1988), pp. 9581–9593. ISSN: 0163-1829. DOI: 10.1103/PhysRevB.38.9581. URL: https://link.aps.org/doi/10.1103/PhysRevB.38.9581.

[6] B. Reulet and H. Bouchiat. « ac conductivity of mesoscopic rings: The discrete-spectrum limit ». In: *Phys. Rev. B* 50 (4 July 1994), pp. 2259–2272. DOI: 10.1103/PhysRevB.50.2259. URL: https://link.aps.org/doi/10.1103/PhysRevB.50.2259.

[7] J. B. Johnson. « Thermal Agitation of Electricity in Conductors ». en. In: *Phys. Rev.* 32.1 (July 1928), pp. 97–109. ISSN: 0031-899X. DOI: 10.1103/PhysRev.32.97. URL: https://link.aps.org/doi/10.1103/PhysRev.32.97.

[8] Herbert B. Callen and Theodore A. Welton. « Irreversibility and Generalized Noise ». en. In: *Phys. Rev.* 83.1 (July 1951), pp. 34–40. ISSN: 0031-899X. DOI: 10.1103/PhysRev.83.34. URL: https://link.aps.org/doi/10.1103/PhysRev.83.34 (visited on 05/25/2023).

[9] R Kubo. « The fluctuation-dissipation theorem ». en. In: ().

[10] B. D. Josephson. « Possible new effects in superconductive tunnelling ». In: *Physics Letters* 1.7 (1962), pp. 251–253. ISSN: 0031-9163. DOI: https://doi.org/10.1016/0031-9163(62)91369-0. URL: https://www.sciencedirect.com/science/article/pii/0031916362913690.

[11] P. W. Anderson and J. M. Rowell. « Probable Observation of the Josephson Superconducting Tunneling Effect ». en. In: *Phys. Rev. Lett.* 10.6 (Mar. 1963), pp. 230–232. ISSN: 0031-9007. DOI: 10.1103/PhysRevLett.10.230. URL: https://link.aps.org/doi/10.1103/PhysRevLett.10.230.

[12] A. F. Andreev. « Thermal conductivity of the intermediate state of superconductors ». In: *JETP* 19:1228 (1964).

[13] Philip F. Bagwell. « Suppression of the Josephson current through a narrow, mesoscopic, semiconductor channel by a single impurity ». en. In: *Phys. Rev. B* 46.19 (Nov. 1992), pp. 12573–12586. ISSN: 0163-1829, 1095-3795. DOI: 10.1103/PhysRevB.46.12573. URL: https://link.aps.org/doi/10.1103/PhysRevB.46.12573.

[14] O.N. Dorokhov. « On the coexistence of localized and extended electronic states in the metallic phase ». In: *Solid State Communications* 51.6 (1984), pp. 381–384. ISSN: 0038-1098. DOI: https://doi.org/10.1016/0038-1098(84)90117-0.

[15] M. Ferrier et al. « Phase-dependent Andreev spectrum in a diffusive SNS junction: Static and dynamic current response ». en. In: *Phys. Rev. B* 88.17 (Nov. 2013), p. 174505. ISSN: 1098-0121, 1550-235X. DOI: 10.1103/PhysRevB.88.174505. URL: https://link.aps.org/doi/10.1103/PhysRevB.88.174505.

[16] K. K. Likharev. « Superconducting weak links ». In: *Rev. Mod. Phys.* 51 (1 Jan. 1979), pp. 101–159. DOI: 10.1103/RevModPhys.51.101. URL: https://link.aps.org/doi/10.1103/RevModPhys.51.101.

[17] I. O. Kulik and A. N. Omel'Yanchuk. « Contribution to the microscopic theory of the Josephson effect in superconducting bridges ». In: *Soviet Journal of Experimental and Theoretical Physics Letters* 21 (Feb. 1975), p. 96.

[18] I O Kulik and A N Omel'yanchuk. « Properties of superconducting microbridges in the pure limit ». In: *Sov. J. Low Temp. Phys. (Engl. Transl.); (United States)* 3:7 (July 1977).

[19] P. Dubos et al. « Josephson critical current in a long mesoscopic S-N-S junction ». en. In: *Phys. Rev. B* 63.6 (Jan. 2001), p. 064502. ISSN: 0163-1829, 1095-3795. DOI: 10.1103/PhysRevB.63.064502. URL: https://link.aps.org/doi/10.1103/PhysRevB.63.064502.

[20] Igor O. Kulik. « Macroscopic Quantization and the Proximity Effect in S-N-S Junctions ». In: *Soviet Journal of Experimental and Theoretical Physics* (1970).

[21] D. Averin and H. T. Imam. « Supercurrent Noise in Quantum Point Contacts ». en. In: *Phys. Rev. Lett.* 76.20 (May 1996), pp. 3814–3817. ISSN: 0031-9007, 1079-7114. DOI: 10.1103/PhysRevLett.76.3814. URL: https://link.aps.org/doi/10.1103/PhysRevLett.76.3814.

[22] R. Landauer and M. Büttiker. « Resistance of Small Metallic Loops ». In: *Phys. Rev. Lett.* 54 (18 May 1985), pp. 2049–2052. DOI: 10.1103/PhysRevLett.54.2049. URL: https://link.aps.org/doi/10.1103/PhysRevLett.54.2049.

[23] A. Martín-Rodero, A. Levy Yeyati, and F. J. García-Vidal. « Thermal noise in superconducting quantum point contacts ». en. In: *Phys. Rev. B* 53.14 (Apr. 1996), R8891–R8894. ISSN: 0163-1829, 1095-3795. DOI: 10.1103/PhysRevB.53.R8891. URL: https://link.aps.org/doi/10.1103/PhysRevB.53.R8891.

[24] Bastien Dassonneville. « Dynamics of Andreev states in a normal metal-superconductor ring : supercurrent fluctuations and spectroscopy of the minigap ». Thesis. Université Paris Sud - Paris XI, Jan. 2014. URL: https://theses.hal.science/tel-01011558.

[25] Anil Murani et al. « Ballistic edge states in Bismuth nanowires revealed by SQUID interferometry ». en. In: *Nat Commun* 8.1 (Aug. 2017), p. 15941. ISSN: 2041-1723. DOI: 10.1038/ncomms15941. URL: http://www.nature.com/articles/ncomms15941.

[26] A. Bernard et al. « Long-lived Andreev states as evidence for protected hinge modes in a bismuth nanoring Josephson junction ». In: *Nature Physics* 19.3 (Mar. 2023), pp. 358–364. ISSN: 1745-2481. DOI: 10.1038/s41567-022-01858-8. URL: https://doi.org/10.1038/s41567-022-01858-8.

[27] A. Murani et al. « Microwave Signature of Topological Andreev level Crossings in a Bismuth-based Josephson Junction ». en. In: *Phys. Rev. Lett.* 122.7 (Feb. 2019), p. 076802. ISSN: 0031-9007, 1079-7114. DOI: 10.1103/PhysRevLett.122.076802. URL: https://link.aps.org/doi/10.1103/PhysRevLett.122.076802.

[28] B. Dassonneville et al. « Dissipation and Supercurrent Fluctuations in a Diffusive Normal-Metal–Superconductor Ring ». In: *Phys. Rev. Lett.* 110 (21 May 2013), p. 217001. DOI: 10.1103/PhysRevLett.110.217001. URL: https://link.aps.org/doi/10.1103/PhysRevLett.110.217001.

[29] B. Dassonneville et al. « Coherence-enhanced phase-dependent dissipation in long SNS Josephson junctions: Revealing Andreev bound state dynamics ». en. In: *Phys. Rev. B* 97.18 (May 2018), p. 184505. ISSN: 2469-9950, 2469-9969. DOI: 10.1103/PhysRevB.97.184505. URL: https://link.aps.org/doi/10.1103/PhysRevB.97.184505.

[30] Francesca Chiodi. « Dynamical effects in Superconductor/Normal metal/Superconductor long Josephson Junctions ». PhD thesis.

[31] Anil Murani. « Superconducting proximity effect in monocrystalline bismuth nanowires ». fr. PhD thesis.

[32] Y. Jin et al. « Ultra-low noise CryoHEMTs for cryogenic high-impedance readout electronics: Results and applications ». en. In: *2016 13th IEEE International Conference on Solid-State and Integrated Circuit Technology (ICSICT)*. Hangzhou, China: IEEE, Oct. 2016, pp. 342–345. ISBN: 978-1-4673-9717-9 978-1-4673-9719-3. DOI: 10.1109/ICSICT.2016.7998915. URL: http://ieeexplore.ieee.org/document/7998915/.

[33] D.M. Pozar. *Microwave Engineering, 4th Edition*. Wiley, 2011. ISBN: 9781118213636.

[34] F. Teyssandier and D. Prêle. « Commercially Available Capacitors at Cryogenic Temperatures ». In: *Ninth International Workshop on Low Temperature Electronics - WOLTE9*. Guaruja, Brazil, June 2010. URL: https://hal.science/hal-00623399.

[35] S Thoms and D S Macintyre. « 2014: An Investigation of CSAR 62, a New Resist for Electron Beam Lithography ». en. In: ().

[36] Michele Bonaldi et al. « Thermal noise in a high Q cryogenic resonator ». en. In: *Review of Scientific Instruments* 70.3 (Mar. 1999), pp. 1851–1856. ISSN: 0034-6748, 1089-7623. DOI: 10.1063/1.1149679. URL: http://aip.scitation.org/doi/10.1063/1.1149679.

[37] N. W. Ashcroft and N. D. Mermin. *Solid State Physics*. Holt-Saunders, 1976.

[38] F. Zhou and B. Spivak. « Resistance of superconductor-normal-metal-superconductor (SNS) junctions ». en. In: *Jetp Lett.* 65.4 (Feb. 1997), pp. 369–374. ISSN: 0021-3640, 1090-6487. DOI: 10.1134/1.567374. URL: http://link.springer.com/10.1134/1.567374.

[39] K. S. Tikhonov and M. V. Feigel'man. « Admittance of a long diffusive SNS junction ». en. In: *Phys. Rev. B* 91.5 (Feb. 2015), p. 054519. ISSN: 1098-0121, 1550-235X. DOI: 10.1103/PhysRevB.91.054519. URL: https://link.aps.org/doi/10.1103/PhysRevB.91.054519.

[40] Liang Fu and C. L. Kane. « Josephson current and noise at a superconductor/quantum-spin-Hall-insulator/superconductor junction ». en. In: *Phys. Rev. B* 79.16 (Apr. 2009), p. 161408. ISSN: 1098-0121, 1550-235X. DOI: 10.1103/PhysRevB.79.161408. URL: https://link.aps.org/doi/10.1103/PhysRevB.79.161408.

[41] Christoph W Groth et al. « Kwant: a software package for quantum transport ». en. In: *New J. Phys.* 16.6 (June 2014), p. 063065. ISSN: 1367-2630. DOI: 10.1088/1367-2630/16/6/063065. URL: https://iopscience.iop.org/article/10.1088/1367-2630/16/6/063065.

[42] Dmitri A. Ivanov, Raphael von Roten, and Gianni Blatter. « Minigap in a long disordered SNS junction: Analytical results ». en. In: *Phys. Rev. B* 66.5 (Aug. 2002), p. 052507. ISSN: 0163-1829, 1095-3795. DOI: 10.1103/PhysRevB.66.052507. URL: https://link.aps.org/doi/10.1103/PhysRevB.66.052507.

[43] D. G. Olivares et al. « Dynamics of quasiparticle trapping in Andreev levels ». en. In: *Phys. Rev. B* 89.10 (Mar. 2014), p. 104504. ISSN: 1098-0121, 1550-235X. DOI: 10.1103/PhysRevB.89.104504. URL: https://link.aps.org/doi/10.1103/PhysRevB.89.104504.

[44] M. O. Goerbig. *Introduction to Quantum Mesoscopic Transport and Topological Matter. Lectures notes*. Ecole Polytechnique, 2023.

[45] TU Delft. *Topology in Condensed Matter*. 2017. URL: https://ocw.tudelft.nl/courses/topology-condensed-matter-concept/.

[46] B. Andrei Bernevig and Shou-Cheng Zhang. « Quantum Spin Hall Effect ». en. In: *Phys. Rev. Lett.* 96.10 (Mar. 2006), p. 106802. ISSN: 0031-9007, 1079-7114. DOI: 10.1103/PhysRevLett.96.106802. URL: https://link.aps.org/doi/10.1103/PhysRevLett.96.106802.

[47] C. L. Kane and E. J. Mele. « Quantum Spin Hall Effect in Graphene ». en. In: *Phys. Rev. Lett.* 95.22 (Nov. 2005), p. 226801. ISSN: 0031-9007, 1079-7114. DOI: 10.1103/PhysRevLett.95.226801. URL: https://link.aps.org/doi/10.1103/PhysRevLett.95.226801.

[48] M. Z. Hasan and C. L. Kane. « Colloquium: Topological insulators ». In: *Rev. Mod. Phys.* 82 (4 Nov. 2010), pp. 3045–3067. DOI: 10.1103/RevModPhys.82.3045. URL: https://link.aps.org/doi/10.1103/RevModPhys.82.3045.

[49] Jiewen Xiao and Binghai Yan. « First-principles calculations for topological quantum materials ». In: *Nature Reviews Physics* 3.4 (Apr. 2021), pp. 283–297. ISSN: 2522-5820. DOI: 10.1038/s42254-021-00292-8. URL: https://doi.org/10.1038/s42254-021-00292-8.

[50] D. Hsieh et al. « A topological Dirac insulator in a quantum spin Hall phase ». en. In: *Nature* 452.7190 (Apr. 2008), pp. 970–974. ISSN: 0028-0836, 1476-4687. DOI: 10.1038/nature06843. URL: https://www.nature.com/articles/nature06843.

[51] D. Hsieh et al. « Observation of Unconventional Quantum Spin Textures in Topological Insulators ». en. In: *Science* 323.5916 (Feb. 2009), pp. 919–922. ISSN: 0036-8075, 1095-9203. DOI: 10.1126/science.1167733. URL: https://www.science.org/doi/10.1126/science.1167733.

[52] B. Andrei Bernevig, Taylor L. Hughes, and Shou-Cheng Zhang. « Quantum Spin Hall Effect and Topological Phase Transition in HgTe Quantum Wells ». en. In: *Science* 314.5806 (Dec. 2006), pp. 1757–1761. ISSN: 0036-8075, 1095-9203. DOI: 10.1126/science.1133734. URL: https://www.science.org/doi/10.1126/science.1133734.

[53] Markus König et al. « Quantum Spin Hall Insulator State in HgTe Quantum Wells ». en. In: *Science* 318.5851 (Nov. 2007), pp. 766–770. ISSN: 0036-8075, 1095-9203. DOI: 10.1126/science.1148047. URL: https://www.science.org/doi/10.1126/science.1148047.

[54] Frank Schindler et al. « Higher-order topological insulators ». en. In: *SCIENCE ADVANCES* (2018).

[55] Josias Langbehn et al. « Reflection-Symmetric Second-Order Topological Insulators and Superconductors ». In: *Phys. Rev. Lett.* 119 (24 Dec. 2017), p. 246401. DOI: 10.1103/PhysRevLett.119.246401. URL: https://link.aps.org/doi/10.1103/PhysRevLett.119.246401.

[56] Eslam Khalaf. « Higher-order topological insulators and superconductors protected by inversion symmetry ». In: *Phys. Rev. B* 97 (20 May 2018), p. 205136. DOI: 10.1103/PhysRevB.97.205136. URL: https://link.aps.org/doi/10.1103/PhysRevB.97.205136.

[57] Max Geier et al. « Second-order topological insulators and superconductors with an order-two crystalline symmetry ». In: *Phys. Rev. B* 97 (20 May 2018), p. 205135. DOI: 10.1103/PhysRevB.97.205135. URL: https://link.aps.org/doi/10.1103/PhysRevB.97.205135.

[58] C. W. J. Beenakker et al. « Fermion-Parity Anomaly of the Critical Supercurrent in the Quantum Spin-Hall Effect ». In: *Phys. Rev. Lett.* 110 (1 Jan. 2013), p. 017003. DOI: 10.1103/PhysRevLett.110.017003. URL: https://link.aps.org/doi/10.1103/PhysRevLett.110.017003.

[59] Xiaofeng Qian et al. « Quantum spin Hall effect in two-dimensional transition metal dichalcogenides ». en. In: ().

[60] Su-Yang Xu et al. « Electrically switchable Berry curvature dipole in the monolayer topological insulator WTe2 ». In: *Nature Physics* 14.9 (Sept. 2018), pp. 900–906. ISSN: 1745-2481. DOI: 10.1038/s41567-018-0189-6. URL: https://doi.org/10.1038/s41567-018-0189-6.

[61] Zaiyao Fei et al. « Edge conduction in monolayer WTe2 ». en. In: *Nature Phys* 13.7 (July 2017), pp. 677–682. ISSN: 1745-2473, 1745-2481. DOI: 10.1038/nphys4091. URL: https://www.nature.com/articles/nphys4091.

[62] Feipeng Zheng et al. « On the Quantum Spin Hall Gap of Monolayer 1T-WTe_2 ». en. In: *Adv. Mater.* 28.24 (June 2016), pp. 4845–4851. ISSN: 09359648. DOI: 10.1002/adma.201600100. URL: https://onlinelibrary.wiley.com/doi/10.1002/adma.201600100 (visited on 08/07/2023).

[63] Lang Peng et al. « Observation of topological states residing at step edges of WTe2 ». en. In: *Nat Commun* 8.1 (Sept. 2017), p. 659. ISSN: 2041-1723. DOI: 10.1038/s41467-017-00745-8. URL: https://www.nature.com/articles/s41467-017-00745-8.

[64] Sanfeng Wu et al. « Observation of the quantum spin Hall effect up to 100 kelvin in a monolayer crystal ». en. In: *Science* 359.6371 (Jan. 2018), pp. 76–79. ISSN: 0036-8075, 1095-9203. DOI: 10.1126/science.aan6003. URL: https://www.science.org/doi/10.1126/science.aan6003.

[65] Mazhar N. Ali et al. « Large, non-saturating magnetoresistance in WTe2 ». en. In: *Nature* 514.7521 (Oct. 2014), pp. 205–208. ISSN: 0028-0836, 1476-4687. DOI: 10.1038/nature13763. URL: https://www.nature.com/articles/nature13763.

[66] I. Pletikosi ć et al. « Electronic Structure Basis for the Extraordinary Magnetoresistance in WTe_2 ». In: *Phys. Rev. Lett.* 113 (21 Nov. 2014), p. 216601. DOI: 10.1103/PhysRevLett.113.216601. URL: https://link.aps.org/doi/10.1103/PhysRevLett.113.216601.

[67] H. Y. Lv et al. « Perfect charge compensation in WTe $_2$ for the extraordinary magnetoresistance: From bulk to monolayer ». en. In: *EPL* 110.3 (May 2015), p. 37004. ISSN: 0295-5075, 1286-4854. DOI: 10.1209/0295-5075/110/37004. URL: https://iopscience.iop.org/article/10.1209/0295-5075/110/37004.

[68] Ya Yi et al. « Thickness dependent magneto transport properties of WTe2 thin films ». In: *Solid State Communications* 260 (2017), pp. 45–49. ISSN: 0038-1098. DOI: https://doi.org/10.1016/j.ssc.2017.05.017. URL: https://www.sciencedirect.com/science/article/pii/S0038109817301667.

[69] Alexey A. Soluyanov et al. « Type-II Weyl Semimetals ». en. In: *Nature* 527.7579 (Nov. 2015). arXiv:1507.01603 [cond-mat], pp. 495–498. ISSN: 0028-0836, 1476-4687. DOI: 10.1038/nature15768. URL: http://arxiv.org/abs/1507.01603.

[70] Peng Li et al. « Evidence for topological type-II Weyl semimetal WTe2 ». en. In: *Nat Commun* 8.1 (Dec. 2017), p. 2150. ISSN: 2041-1723. DOI: 10.1038/s41467-017-02237-1. URL: https://www.nature.com/articles/s41467-017-02237-1.

[71] Chui-Zhen Chen et al. « Asymmetric Josephson Effect in Inversion Symmetry Breaking Topological Materials ». en. In: *Phys. Rev. B* 98.7 (Aug. 2018). arXiv:1802.10389 [cond-mat], p. 075430. ISSN: 2469-9950, 2469-9969. DOI: 10.1103/PhysRevB.98.075430. URL: http://arxiv.org/abs/1802.10389.

[72] O. O. Shvetsov et al. « Realization of a Double-Slit SQUID Geometry by Fermi Arc Surface States in a WTe2 Weyl Semimetal ». en. In: *Jetp Lett.* 107.12 (June 2018), pp. 774–779. ISSN: 0021-3640, 1090-6487. DOI: 10.1134/S0021364018120020. URL: http://link.springer.com/10.1134/S0021364018120020.

[73] P K Das et al. « Electronic properties of candidate type-II Weyl semimetal WTe $_2$. A review perspective ». en. In: *Electron. Struct.* 1.1 (Mar. 2019), p. 014003. ISSN: 2516-1075. DOI: 10.1088/2516-1075/ab0835. URL: https://iopscience.iop.org/article/10.1088/2516-1075/ab0835.

[74] F. Y. Bruno et al. « Observation of large topologically trivial Fermi arcs in the candidate type-II Weyl semimetal WT e 2 ». en. In: *Phys. Rev. B* 94.12 (Sept. 2016), p. 121112. ISSN: 2469-9950, 2469-9969. DOI: 10.1103/PhysRevB.94.121112. URL: https://link.aps.org/doi/10.1103/PhysRevB.94.121112.

[75] Zhijun Wang et al. « Higher-Order Topology, Monopole Nodal Lines, and the Origin of Large Fermi Arcs in Transition Metal Dichalcogenides X Te 2 (X = Mo , W) ». en. In: *Phys. Rev. Lett.* 123.18 (Oct. 2019), p. 186401. ISSN: 0031-9007, 1079-7114. DOI: 10.1103/PhysRevLett.123.186401. URL: https://link.aps.org/doi/10.1103/PhysRevLett.123.186401.

[76] Chen Fang et al. « Topological nodal line semimetals* ». In: *Chinese Physics B* 25.11 (Nov. 2016), p. 117106. DOI: 10.1088/1674-1056/25/11/117106. URL: https://dx.doi.org/10.1088/1674-1056/25/11/117106.

[77] Frank Schindler et al. « Higher-order topology in bismuth ». en. In: *Nature Phys* 14.9 (Sept. 2018), pp. 918–924. ISSN: 1745-2473, 1745-2481. DOI: 10.1038/s41567-018-0224-7. URL: https://www.nature.com/articles/s41567-018-0224-7.

[78] Yong-Bin Choi et al. « Evidence of higher-order topology in multilayer WTe2 from Josephson coupling through anisotropic hinge states ». en. In: *Nat. Mater.* 19.9 (Sept. 2020), pp. 974–979. ISSN: 1476-1122, 1476-4660. DOI: 10.1038/s41563-020-0721-9. URL: https://www.nature.com/articles/s41563-020-0721-9.

[79] Artem Kononov et al. « One-Dimensional Edge Transport in Few-Layer WTe $_2$ ». en. In: *Nano Lett.* 20.6 (June 2020), pp. 4228–4233. ISSN: 1530-6984, 1530-6992. DOI: 10.1021/acs.nanolett.0c00658. URL: https://pubs.acs.org/doi/10.1021/acs.nanolett.0c00658.

[80] Ce Huang et al. « Edge superconductivity in multilayer WTe2 Josephson junction ». In: *National Science Review* 7.9 (May 2020), pp. 1468–1475. ISSN: 2095-5138. DOI: 10.1093/nsr/nwaa114. eprint: https://academic.oup.com/nsr/article-pdf/7/9/1468/38881940/nwaa114.pdf. URL: https://doi.org/10.1093/nsr/nwaa114.

[81] Lucia Vigliotti et al. « Effects of the Spatial Extension of the Edge Channels on the Interference Pattern of a Helical Josephson Junction ». en. In: *Nanomaterials* 13.3 (Jan. 2023). arXiv:2302.00024 [cond-mat], p. 569. ISSN: 2079-4991. DOI: 10.3390/nano13030569. URL: http://arxiv.org/abs/2302.00024.

[82] R. C. Dynes and T. A. Fulton. « Supercurrent Density Distribution in Josephson Junctions ». en. In: *Phys. Rev. B* 3.9 (May 1971), pp. 3015–3023. ISSN: 0556-2805. DOI: 10.1103/PhysRevB.3.3015. URL: https://link.aps.org/doi/10.1103/PhysRevB.3.3015.

[83] A. Barone and G. Paterno. *Physics and applications of the Josephson effect*. Wiley, 1982. ISBN: 9780471014690.

[84] J. C. Cuevas and F. S. Bergeret. « Magnetic Interference Patterns and Vortices in Diffusive SNS Junctions ». en. In: *Phys. Rev. Lett.* 99.21 (Nov. 2007), p. 217002. ISSN: 0031-9007, 1079-7114. DOI: 10.1103/PhysRevLett.99.217002. URL: https://link.aps.org/doi/10.1103/PhysRevLett.99.217002.

[85] F. Chiodi et al. « Geometry-related magnetic interference patterns in long S N S Josephson junctions ». en. In: *Phys. Rev. B* 86.6 (Aug. 2012), p. 064510. ISSN: 1098-0121, 1550-235X. DOI: 10.1103/PhysRevB.86.064510. URL: https://link.aps.org/doi/10.1103/PhysRevB.86.064510.

[86] Jorge Vallejo Bustamante. « Singular orbital diamagnetism and paramagnetism in graphene ». Theses. Université Paris-Saclay, Feb. 2023. URL: https://theses.hal.science/tel-04032004.

[87] Martin Endres et al. « Transparent Josephson Junctions in Higher-Order Topological Insulator WTe2 via Pd Diffusion ». en. In: *Phys. Rev. Materials* 6.8 (Aug. 2022). arXiv:2205.06542 [cond-mat], p. L081201. ISSN: 2475-9953. DOI: 10.1103/PhysRevMaterials.6.L081201. URL: http://arxiv.org/abs/2205.06542.

[88] P. Adroguer et al. « Probing the helical edge states of a topological insulator by Cooper-pair injection ». In: *Phys. Rev. B* 82 (8 Aug. 2010), p. 081303. DOI: 10.1103/PhysRevB.82.081303. URL: https://link.aps.org/doi/10.1103/PhysRevB.82.081303.

[89] A. Murani et al. « Andreev spectrum with high spin-orbit interactions: Revealing spin splitting and topologically protected crossings ». In: *Phys. Rev. B* 96 (16 Oct. 2017), p. 165415. DOI: 10.1103/PhysRevB.96.165415. URL: https://link.aps.org/doi/10.1103/PhysRevB.96.165415.

[90] Ce Huang et al. « Inducing Strong Superconductivity in WTe2 by a Proximity Effect ». In: *ACS Nano* 12.7 (July 2018), pp. 7185–7196. ISSN: 1936-0851. DOI: 10.1021/acsnano.8b03102. URL: https://doi.org/10.1021/acsnano.8b03102.

[91] Akihiko Sekine et al. *Emergent One-Dimensional Helical Channel in Higher-Order Topological Insulators with Step Edges*. en. arXiv:2206.15206 [cond-mat]. Dec. 2022. URL: http://arxiv.org/abs/2206.15206.

[92] Alexandre Bernard. « Thèse soutenue à Paris-Saclay, le 08 décembre 2022, par ». fr. In: ().

[93] J. Vallejo Bustamante et al. « Detection of graphene's divergent orbital diamagnetism at the Dirac point ». In: *Science* 374.6573 (2021), pp. 1399–1402. DOI: 10.1126/science.abf9396. eprint: https://www.science.org/doi/pdf/10.1126/science.abf9396. URL: https://www.science.org/doi/abs/10.1126/science.abf9396.

[94] Dmitriy S. Shapiro, Alexander D. Mirlin, and Alexander Shnirman. « Excess equilibrium noise in a topological SNS junction between chiral Majorana liquids ». In: *Phys. Rev. B* 98 (24 Dec. 2018), p. 245405. DOI: 10.1103/PhysRevB.98.245405. URL: https://link.aps.org/doi/10.1103/PhysRevB.98.245405.

[95] Ziwei Dou et al. « Microwave photoassisted dissipation and supercurrent of a phase-biased graphene-superconductor ring ». en. In: *Phys. Rev. Research* 3.3 (July 2021), p. L032009. ISSN: 2643-1564. DOI: 10.1103/PhysRevResearch.3.L032009. URL: https://link.aps.org/doi/10.1103/PhysRevResearch.3.L032009.

[96] Ziwei Dou et al. *Supercurrent Noise in a Phase-Biased Superconductor-Normal Ring in Thermal Equilibrium*. 2022. arXiv: 2208.03482 [cond-mat.mes-hall].